Development of an algorithm for the distinction between muon and electron neutrino events for the P2O plausibility study

Masterarbeit aus der Physik

vorgelegt von:
Thomas Kittler
9. Februar 2015

Erlangen Centre For Astroparticle Physics
Friedrich-Alexander-Universität Erlangen-Nürnberg

Betreuer: Prof. Dr. Ulrich Katz

Ich versichere, dass ich die Arbeit ohne fremde Hilfe und ohne Benutzung anderer als der angegebenen Quellen angefertigt habe und dass die Arbeit in gleicher oder ähnlicher Form noch keiner anderen Prüfungsbehörde vorgelegen hat und von dieser als Teil einer Prüfungsleistung angenommen wurde. Alle Ausführungen, die wörtlich oder sinngemäß übernommen wurden, sind als solche gekennzeichnet.

Erlangen, den 09.02.2015

Abstract

Within the following thesis the principle and the development of a working algorithm for the distinction of ν_e and ν_μ events for the Protvino To ORCA plausibility study is described and the efficiency is presented. Furthermore the simulation of beam neutrino events, which were used for the analysis, within a densely detected layout is described. Four different event samples, and for each sample events in nine small energy bands from 2 to 10 GeV, were produced in order to get results as detailed as possible. The analysis part contains the efficiency analysis of a simple event selection, the analysis of errors of vertex, track and interaction time reconstruction algorithms and the classification results for the distinction between ν_e and ν_μ events.

Contents

Chapter 1

Introduction

Since the postulation by Wolfgang Pauli in 1930 neutrinos remain one of the most mysterious particles in physics. Nearly massless, no electric charge and a very small cross section make it very difficult to investigate the neutrino properties, thus pushing the limits of large scale experiments for the last decades. Over 80 years after Paulis postulation a lot of the neutrino properties are still unknown. The absolute mass of neutrinos could not be determined so far, only upper limits could be measured. Furthermore it is still in question whether neutrinos are their own anti-particles, so called Majorana particles.
One of the most outstanding features of neutrinos, however, is neutrino oscillation, the ability of neutrinos to switch between flavor eigenstate while propagating through space and time. Neutrino oscillation, however, is only possible if not all neutrinos have zero mass. With oscillation experiments, only statements about the differences of neutrino masses can be made. So far, two mass hierarchies are compatible with the experimental results, called normal mass hierarchy and inverted mass hierarchy. For the next generation experiments the exclusion of one mass hierarchy comes within reach since the latest measurement of the last mixing angle θ_{13} [26].
The feasibility study called ORCA (Oscillation Research with Cosmics in the Abyss) aims at the exclusion of one mass hierarchy. One possible option which is investigated, is to use a GeV neutrino beam instead of atmospheric neutrinos as a particle source. A suiting particle accelerator is located in Protvino, Russia, which has been used to produce a neutrino beam in the past and would be at a perfect distance to possible sites for the ORCA detector. This option is called P2O (Protvino To ORCA).
The following thesis describes the development of an algorithm for the distinction between muon and electron beam neutrino events for the P2O plausibility study. After a short introduction of the theoretical background in chapter 2 the proposed experimental set up is introduced in chapter 3. In chapter 4 the production chain for neutrino beam events is described, and the signatures of ν_e and ν_μ events within a densely instrumented detector are shown. Afterwards the basic idea for the distinction is described and the algorithm, which was developed in order to calculate features for a classifier, is explained in detail. The last part of this chapter describes briefly the used classifier and what features have been chosen for a ν_e ν_μ event distinction. Chapter 5 contains the obtained results, first a efficiency analysis of the used event selection then a detailed anal-

ysis of the reconstruction errors of used vertex, lepton direction and interaction time reconstruction algorithms. The chapter ends with the presentation of the efficiency analysis of the distinction between ν_e and ν_μ events for four different samples and additionally the analysis of a distinction between track and shower like events. In chapter 6 these results are then discussed, interpreted and connected to each other and chapter 7 completes the thesis with a summary and a brief listing of possible future topics.

Chapter 2

Theoretical Background

2.1 The standard model of particle physics

In this section the standard model of particle physics shall be briefly introduced on a phenomenological level. The standard model of particle physics is the established approach to describe quantitatively the behavior of quarks and leptons and their non-gravitational interaction. Within the standard model two groups of particles are defined, namely fermions and gauge bosons.

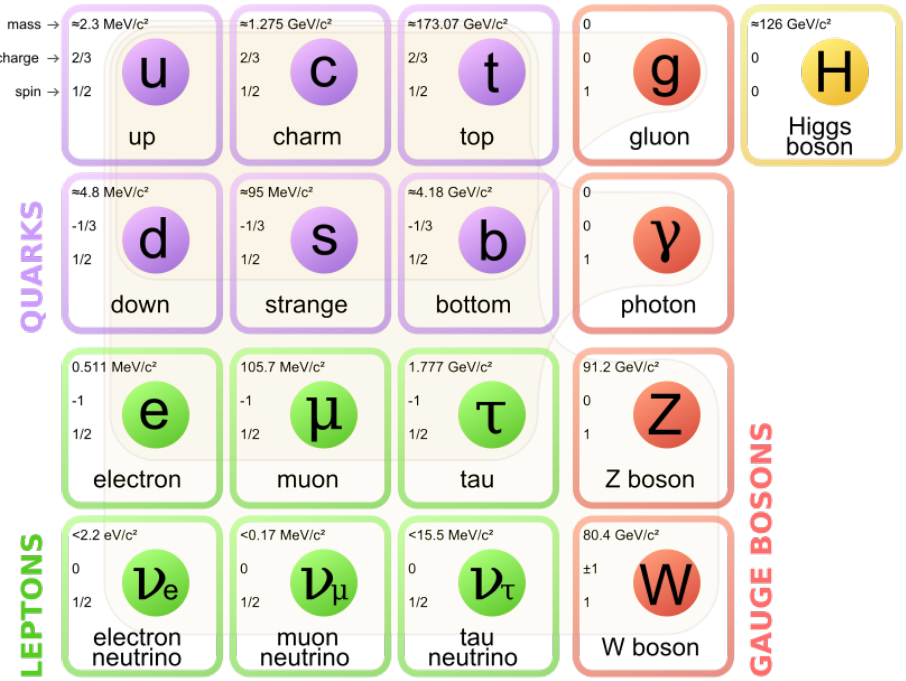

Figure 2.1: Particles of the Standard Model [1]

Fermions are structureless, massive, subatomic particles with half-number spin. Ordinary macroscopic matter for example is made of fermions. Within the fermions two other groups are defined, leptons and quarks, each group containing three doublets of two particles each.
In the quark section the three doublets are (u, d), (c, s) and (t, b). All quarks carry an electromagnetic charge of either $+1/3$ (u, c and t quark) or $-2/3$ (d, s and b quark) (inverse sign for anti quarks). Quarks can interact via the electromagnetic, the weak and the strong force (gravitation is omitted in this context).
In the leptonic section these doublets are (ν_e, e^-), (ν_μ, μ^-) and (ν_τ, τ^-). All leptons can interact via the weak interaction, but only electron, muon and tauon carry an electromagnetic charge (-1 for particles, $+1$ for anti-particles), so only these particles can interact electromagnetically. Leptonic particles can not interact via the strong interaction since they do not carry any "color", which can be seen as an analogon to the electric charge for the strong interaction.
The other group of particles within the standard model are gauge bosons. Gauge bosons are structureless particles with whole-number spin. Gluons (g) are the mediators of the strong force, $W^\pm$ and Z^0 are the mediators of the weak force and photons (γ) of the electromagnetic force. The recently discovered Higgs Boson (H) can interact with all massive particles. [20]

2.2 Neutrinos

In this section a closer look is taken at neutrinos in order to get a better understanding of what neutrinos are, what properties are known and what is still unknown and about topics of recent experiments.

2.2.1 Properties of Neutrinos

As mentioned in chapter 2.1 neutrinos are massive particles with half-number spin, carry no electric charge and can only interact via the weak force, besides gravitation.
So far three types of neutrinos have been found, namely the electron neutrino ν_e, the muon neutrino ν_μ and the tau neutrino ν_τ. Up to this point experiments indicate that the chirality of all neutrinos is left-handed and the chirality of antineutrinos is right-handed. This is not surprising, since the weak interaction of the SM does not couple to right-handed particles or left-handed antiparticles. Therefore it is justified to suggest the existence of right-handed neutrinos which only interact gravitational. Such particles are referred to as "sterile neutrinos" and the proof of their existence might have a huge impact on particles physics and cosmology [4].
The absolute masses of neutrinos are still unknown, only upper boundaries could be determined from the collected data of various measurements.
One of these upper limits comes from the field of cosmology. The analysis of data from the Wilkinson Microwave Anisotropy Probe (WMAP), the Sloan Digital Sky Survey (SDSS), the SuperNova Legacy Survey (SNLS) and the Lyman-α forest results in an upper limit of $\sum_\nu = 0.2 - 0.4\,\mathrm{eV}$ (95% CL) [5].
One of the experiments that is currently trying to determine the mass of electron

neutrinos is the KARlsruhe TRItium Neutrino experiment (KATRIN) which is located at the Karlsruhe Institute of Technology (KIT). KATRIN will be sensitive to a mass as small as 0.2 eV and it is planned to start taking data in 2015[29].
Another experiment which might be able to determine the neutrino mass is the attempt to confirm the existence of the neutrinoless double beta decay ($0\nu\beta\beta$) (e.g. EXO200). If such a process could be confirmed one could not only calculate the neutrino mass, but also determine that neutrino are Majorana particles instead of Dirac particles, meaning that neutrinos and antineutrinos are the same particles [10].
The search of a possible CP-violating phase δ is also still ongoing, but with resent measurements of the last mixing angle θ_{13} ([26]) and the analysis of data from different experiments possible hints towards $\delta \approx \pi$ have been calculated [6]. While the simplest version of the Standard Model assumes that neutrinos are massless particles, the confirmation of neutrino oscillation in various experiments (e.q. T2K [8] and most recently OPERA [11]) contradicts the zero mass theory for neutrinos (neutrino oscillation will be discussed in section 2.2.2). Since neutrino oscillation depends only on the differences of the squared masses of the neutrinos, oscillation experiments can not determine the absolute value of neutrino masses, but the differences of the squared masses. The most recent values for squared mass differences are:

$$\Delta m^2_{12} = m^2_1 - m^2_2 = 7.58 \cdot 10^{-5}\,\mathrm{eV}^2 \tag{2.1}$$

$$|\Delta m^2_{23}| = |m^2_2 - m^2_3| = 2.32 \cdot 10^{-3}\,\mathrm{eV}^2 \tag{2.2}$$

Values taken from [7]. From these values one can calculate that there must be one or more neutrinos with a mass of at least 0.04 eV.
The sign of Δm_{23} is another aspect which is still unknown. The two possibilities are called normal mass hierarchy (NH) for $\Delta m_{23} > 0$ and therefore an ordering of $m_1 < m_2 < m_3$ and inverted mass hierarchy for $\Delta m_{23} < 0$ and an ordering of $m_3 < m_1 < m_2$ (see fig 2.2).
The exploration of these unknown properties of neutrinos does not only expand our knowledge about fundamental particles, but has a huge impact on a lot of theories in various fields, from particle physics to cosmology.

2.2.2 Neutrino oscillation

The phenomenon called neutrino oscillation is that a neutrino of a certain flavour ν_α ($\alpha = e, \mu, \tau$) can change its flavour while moving through space and time. Therefore the probability of detecting a ν_β ($\beta = e, \mu, \tau$) at a certain distance of a neutrino source which produced a ν_α, with $\alpha \neq \beta$, is not zero.
This behavior requires two conditions:

- not all neutrinos have the same mass $\rightarrow$ not all neutrinos have a mass of zero
- lepton flavour is not preserved.

The following section describes briefly the theoretical background of neutrino oscillation in vacuum and in matter [30].

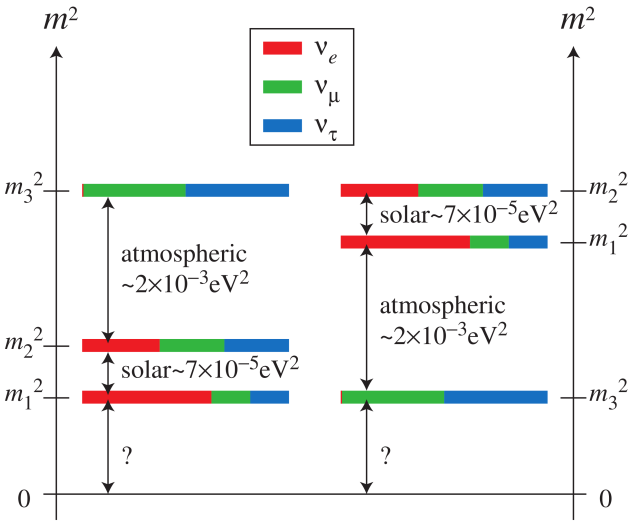

Figure 2.2: Schematic view of the Neutrino mass hierarchy (left: normal hierarchy, right: inverted hierarchy)[14]

Neutrino oscillation in vacuum

First the general case of n orthogonal eigenstates is considered. The flavour and mass eigenstates can be written as:

$$|\nu_\alpha\rangle = \sum_i U_{\alpha i}|\nu_i\rangle \tag{2.3}$$

$$|\nu_i\rangle = \sum_\alpha (U^+)_{i\alpha}|\nu_\alpha\rangle \tag{2.4}$$

where U is a unitary transformation so that $U^+U = 1$. $|\nu_\alpha\rangle$ represents a flavour eigenstate and $|\nu_i\rangle$ a mass eigenstate.
The time development of mass eigenstates can be expressed via

$$|\nu_i(\vec{x},t)\rangle = e^{-i(E_i t - \vec{p}\cdot\vec{x})}|\nu_i(t=0)\rangle. \tag{2.5}$$

Flavour eigenstates are not eigenstates of the mass operator, therefore the time development has a different form. As written in equation 2.4 flavour eigenstates are a linear combination of mass eigenstates for which the time development is shown in equation 2.5. In combining those equations one obtains

$$|\nu(t)\rangle = \sum_i U_{\alpha i} e^{-i(E_i t - \vec{p}\cdot\vec{x})}|\nu_i\rangle = \sum_{i,\beta} U_{\alpha i} U^*_{\beta i} e^{-i(E_i t - \vec{p}\cdot\vec{x})}|\nu_\beta\rangle. \tag{2.6}$$

The transition probability amplitude for $\nu_\alpha \to \nu_\beta$ can then be written as

$$A(\alpha \to \beta, t) = \langle \nu_\beta | \nu(t) \rangle \tag{2.7}$$
$$= \langle \nu_\beta | \sum_{i,\gamma} U_{\alpha i} U^*_{\gamma i} e^{-i(E_i t - \vec{p}\cdot\vec{x})} | \nu_\gamma \rangle \tag{2.8}$$
$$= \sum_i U_{\alpha i} U^*_{\beta i} e^{-i(E_i t - \vec{p}\cdot\vec{x})} \tag{2.9}$$

since $\langle \nu_\alpha | \nu_\beta \rangle = \delta_{\alpha\beta}$. With

$$p = \sqrt{E^2 - m^2} \approx E + \frac{m^2}{2E} \tag{2.10}$$

and with no loss of generality

$$\vec{p} \to (p, 0, 0) \tag{2.11}$$
$$\vec{x} \to (L, 0, 0) \tag{2.12}$$
$$\Rightarrow \vec{p} \cdot \vec{x} = p \cdot L \tag{2.13}$$
$$= (E + \frac{m^2}{2E}) \cdot L. \tag{2.14}$$

Now the phase of the transition amplitude (eq. 2.9) can be written as:

$$-i(E_i t - \vec{p} \cdot \vec{x}) = -i \left(\frac{m_i^2 L}{2E_i} \right). \tag{2.15}$$

The probability of a transition from ν_α to ν_β is the absolute square value of the transition amplitude:

$$P(\alpha \to \beta, t) = |A(\alpha \to \beta, t)|^2 \tag{2.16}$$
$$= \sum_{ij} U_{\alpha i} U^*_{\alpha j} U^*_{\beta i} U_{\beta j} e^{-i(\frac{m_i^2 L}{2E_i} - \frac{m_j^2 L}{2E_j})} \tag{2.17}$$
$$= \sum_i |U_{\alpha i} U^*_{\beta i}|^2 + 2\mathrm{Re} \sum_{i<j} U_{\alpha i} U^*_{\alpha j} U^*_{\beta i} U_{\beta j} e^{-i\Delta_{ij}} \tag{2.18}$$

where

$$\Delta_{ij} = \frac{m_i^2 L}{2E_i} - \frac{m_j^2 L}{2E_j} = \frac{L \delta m_{ij}^2}{2E} \tag{2.19}$$
$$\text{with} \quad E_i = E_j = E \tag{2.20}$$
$$\text{and} \quad \delta m_{ij}^2 = m_i^2 - m_j^2. \tag{2.21}$$

Now the case with $n = 3$, so that there are three mass eigenstates ν_1, ν_2 and ν_3 and three flavour eigenstates ν_e, ν_μ and ν_τ is considered. So far only three flavour eigenstates have been found. In this picture there are three mixing angles $\theta_1, \theta_2, \theta_3$ with $0 \leq \theta_i \leq \frac{\pi}{2}$ and one CP-phase δ with $-\pi \leq \delta \leq \pi$. The

transition matrix U within the three flavour case can be parametrized in the following form:

$$U = \begin{pmatrix} 1 & 0 & 0 \\ 0 & c_2 & s_2 \\ 0 & -s_2 & c_2 \end{pmatrix} \cdot \begin{pmatrix} c_1 & s_1 & 0 \\ -s_1 & c_1 & 0 \\ 0 & 0 & 1 \end{pmatrix} \cdot \begin{pmatrix} 1 & 0 & 0 \\ 0 & 1 & 0 \\ 0 & 0 & e^{i\delta} \end{pmatrix} \cdot \begin{pmatrix} 1 & 0 & 0 \\ 0 & c_3 & s_3 \\ 0 & -s_3 & c_3 \end{pmatrix} \quad (2.22)$$

$$= \begin{pmatrix} c_1 & s_1 c_3 & s_1 s_3 \\ -s_1 c_2 & c_1 c_2 c_3 - s_2 s_3 e^{i\delta} & c_1 c_2 s_3 + s_2 c_3 e^{i\delta} \\ s_1 s_2 & -c_1 s_2 c_3 - c_2 s_3 e^{i\delta} & -c_1 s_2 s_3 + c_2 c_3 e^{i\delta} \end{pmatrix} \quad (2.23)$$

where $s_i = \sin\theta_i$ and $c_i = \cos\theta_i$. Since the mass eigenstates m_i are also eigenstates of the Hamiltonian the Schrödinger equation takes the following form [30]:

$$-i\frac{d\nu_i}{dt} = H^i \nu_i, \quad (2.24)$$

where

$$H^i_{ij} = \frac{m_i^2}{2p}\delta_{ij}. \quad (2.25)$$

In order to calculate the Hamiltonian for flavour eigenstates the transformation matrix from eq. 2.23 can be used:

$$H^\alpha = U H^i U^\dagger \quad (2.26)$$

and the Schrödigner equation takes a similar form to 2.27:

$$-i\frac{d\nu_\alpha}{dt} = H^\alpha \nu_\alpha \quad (2.27)$$

Neutrino oscillation in matter

As soon as neutrinos propagate through matter the probabilities for neutrino oscillation change. Reason for that is the possible interaction of neutrinos with particles of the material. Since neutrinos do not carry any electrically charge, don't have a color charge and have only a very small mass only interaction via the weak force is relevant in this context. While propagating through matter neutrinos can interact with particles of the nucleus, protons and neutrons, or electrons from the atomic shell. All three neutrino flavors, ν_e, ν_μ and ν_τ, can interact via the exchange of a neutral Z-boson, called neutral current interaction (NC), with all particles of the nucleus and the electrons. But only electron neutrinos can interact via the exchange of a W-boson, called charged current interaction (CC), with shell electrons, see figure 2.3.
This causes an additional potential for electron neutrinos while propagating through matter, thus changing the probabilities for neutrino oscillation depending on the electron density of the material.

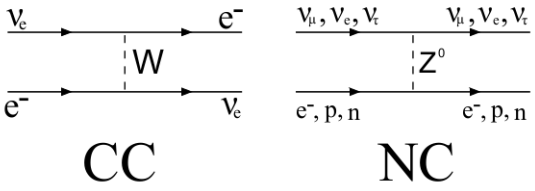

Figure 2.3: Feynman graphs of a charged current (CC, left) and a neutral current (NC, right) interaction[27].

One way to describe this phenomenon quantitatively is to introduce an additional term for the Hamiltonian [15]:

$$H = \frac{1}{2E}\left[U\begin{pmatrix} m_1^2 & 0 & 0 \\ 0 & m_2^2 & 0 \\ 0 & 0 & m_3^2 \end{pmatrix}U^\dagger + \begin{pmatrix} A & 0 & 0 \\ 0 & 0 & 0 \\ 0 & 0 & 0 \end{pmatrix}\right] \tag{2.28}$$

Here U is the neutrino mixing matrix from equation 2.23, $U^\dagger$ the adjoint matrix of U, E the energy and m_i $(i = 1, 2, 3)$ are the mass eigenvalues for the mass eigenstates. The second term is caused by the matter effects where $A = 2\sqrt{2}G_F n_e E_\nu$, G_F is the Fermi coupling constant and n_e is the electron density of the material.

2.2.3 Measured Neutrino Parameters

From a global analysis of various neutrino experiments figure 2.4 summarizes the up to date best fits for different neutrino parameters and their current precision:

Parameter	Best fit	1σ range	2σ range	3σ range
$\delta m^2/10^{-5}$ eV^2 (NH or IH)	7.54	7.32 – 7.80	7.15 – 8.00	6.99 – 8.18
$\sin^2\theta_{12}/10^{-1}$ (NH or IH)	3.07	2.91 – 3.25	2.75 – 3.42	2.59 – 3.59
$\Delta m^2/10^{-3}$ eV^2 (NH)	2.43	2.33 – 2.49	2.27 – 2.55	2.19 – 2.62
$\Delta m^2/10^{-3}$ eV^2 (IH)	2.42	2.31 – 2.49	2.26 – 2.53	2.17 – 2.61
$\sin^2\theta_{13}/10^{-2}$ (NH)	2.41	2.16 – 2.66	1.93 – 2.90	1.69 – 3.13
$\sin^2\theta_{13}/10^{-2}$ (IH)	2.44	2.19 – 2.67	1.94 – 2.91	1.71 – 3.15
$\sin^2\theta_{23}/10^{-1}$ (NH)	3.86	3.65 – 4.10	3.48 – 4.48	3.31 – 6.37
$\sin^2\theta_{23}/10^{-1}$ (IH)	3.92	3.70 – 4.31	3.53 – 4.84 $\oplus$ 5.43 – 6.41	3.35 – 6.63
δ/π (NH)	1.08	0.77 – 1.36	—	—
δ/π (IH)	1.09	0.83 – 1.47	—	—

Figure 2.4: Neutrino parameters and uncertainty intervals from [6]

Chapter 3

Protvino to ORCA (P2O)

After the measurement of the mixing angle θ_{13} all mixing angles and both mass square differences are known. With these values new experiments which might be able to measure still unknown properties of neutrinos can be designed. In the following chapter the basic concepts of a large scale experiment will be introduced, whose primary goal is to determine whether or not the neutrino mass hierarchy is normal or inverted.

3.1 Basic idea for the exclusion of one mass hierarchy

The basic concept of "Protvino to ORCA" (P2O) is to target an underwater megaton Cerenkov neutrino telescope with a conventional GeV ν_μ beam at a certain distance. Due to the artificial source of the neutrinos the composition of the neutrino beam can be measured and is hence to be known with fair precision, and so is the distance to the detector. By using well established models of the Earths density it is possible to calculate the oscillation probabilities for each neutrino flavour.
For a distance of 2600 km and a constant density of $3.3\,g/cm^3$ for the Earth's mantle oscillation probabilities as shown in figure 3.1 were calculated by using the General Long Baseline Experiment Simulator (GLoBES [12]). The GLoBES software package provides tools to calculate oscillation probabilities and event rates for long baseline neutrino experiments using a full three flavour scheme and matter density profiles [12].
For the calculation of the probabilities in figure 3.1 the best fit parameters from figure 2.4 (from [6]) were used and the still unknown CP-Phase δ_{CP} was varied in steps of 30°.
It can easily be seen, that within the neutrino energy range from 3 GeV to 8 GeV significant differences arise between normal mass hierarchy (red lines) and inverted mass hierarchy (blue lines) and there is no overlapping of the two CP-bands. Considering these oscillation probabilities it seems logical to calculate the best energy range in order to separate the two possible hierarchies. In order to accomplish this one can write down the sum of the oscillation probabilities $P(\mu \to \alpha)$ weighted by the energy dependent cross section for each flavour and interaction type (from [22])

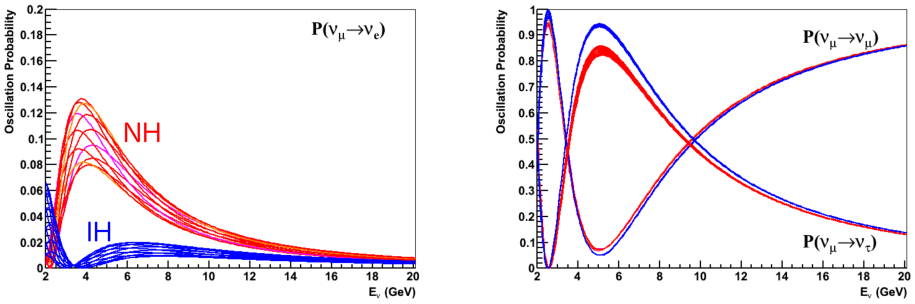

Figure 3.1: Oscillation probabilities for normal hierarchy (red lines) and inverted hierarchy (blue lines) for a baseline of 2600 km. δ_{CP} is varied in steps of 30° [22].

$$P_\mu^\sigma(E_\nu) = \frac{1}{\left[\sigma_{\nu_\mu}^{CC} + \sigma_\nu^{NC}\right](E_0)} \sum_\alpha \left[P(\mu \to \alpha)\sigma_{\nu_\mu}^{CC} + \sigma_\nu^{NC}\right](E\nu), \tag{3.1}$$

with total cross sections

$$\sigma_{\nu_\mu}^{CC}(E_\nu) = \sigma_{\nu_e}^{CC}(E_\nu) = 0.68(E_\nu/GeV)10^{-38}\, cm^2, \tag{3.2}$$

$$\sigma_{\nu_\tau}^{CC}(E_\nu) = 0.29\log\left(\frac{E\nu}{E_0}\right)\sigma_{\nu_\mu}^{CC}(E_\nu) \tag{3.3}$$

and

$$\sigma_\nu^{NC}(E_\nu) = \frac{1}{3}\sigma_{\nu_\mu}^{CC}(E_\nu). \tag{3.4}$$

$P_\mu^\sigma(E_\nu)$ is shown in the left plot of figure 3.2 for $E_0 = 1\,\text{GeV}$.

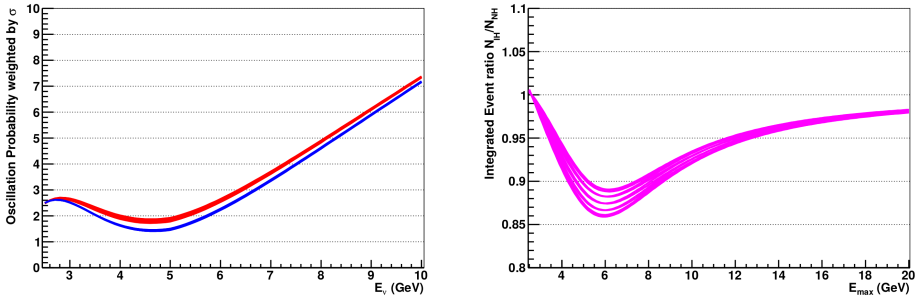

Figure 3.2: **left:** Cross section weighted sum of oscillation probabilities **right:** Ratio of Integrals for IH/NH from left plot from $E_{min} = 2.5\,\text{GeV}$ to E_{max} [22]

The ratio IH/NH of the integrals from the weighted sum is shown in the right plot of figure 3.2 from $E_{min} = 2.5\,\text{GeV}$ to E_{max} (different values for δ_{CP} were

used). It can be seen, that an energy of $E_{max} = 6\,\mathrm{GeV}$ causes the largest difference between the two mass hierarchies, thus giving the best potential for the exclusion of one hierarchy.
This potential can be further enhanced by using flavour identifying methods which will be discussed in section 3.4.

3.2 Production of a GeV neutrino beam in Protvino

The most common approach to produce a neutrino beam is to fire relativistic protons on a massive target. Amongst other particles a lot of pions and kaons will be produced in collisions of protons and target nucleons. Both, pions and kaons are unstable particles with a short lifetime ($\tau_{\pi^\pm} \approx 2.6 \cdot 10^{-8}\,\mathrm{s}$ and $\tau_{K^\pm} \approx 1.2 \cdot 10^{-8}\,\mathrm{s}$). The decay channels with the highest branching ratios are

$$\pi^+ \rightarrow \mu^+ + \nu_\mu \tag{3.5}$$

for the π^+ with a branching ration of 99.99% and

$$K^+ \rightarrow \mu^+ + \nu_\mu \tag{3.6}$$

for the K^+ with a branching ration of 63.55% [7]. These ratios are similar for the anti particles.
The U70 proton accelerator which is hosted at the Institute of High Energy Physics (IHEP) in Protvino near Moscow is operational since 1967 and is capable of producing protons with an energy up to 70 GeV [25]. In former experiments, namely the SKAT experiment, high energetic protons produced by the U70 accelerator have been used to create a neutrino beam. The setup used for the neutrino production is shown in figure 3.3.

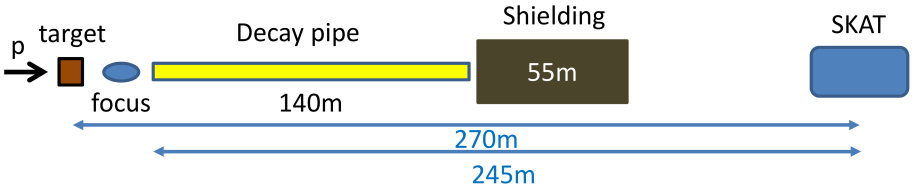

Figure 3.3: Schematic setup for the production of a neutrino beam at IHEP for the SKAT bubble chamber [21].

After the proton beam hit the target a electromagnetic lens is used to focus secondary particles with a positive electric charge and at the same time filter negatively charged particles. The down stream installed decay pipe is used to provide the remaining particles with enough time to decay. After that a shield is attached, which should filter remaining non neutrino particles.
The neutrino beam which was used for the SKAT experiment was a very clean ν_μ beam with contamination of other flavors of less than 1% as can been seen in figure 3.4.
At the moment the U70 accelerator operates with a repetition rate of 0.11 Hz, a maximum energy of 76 GeV and a beam intensity of $1.7 \cdot 10^{13}$ protons per

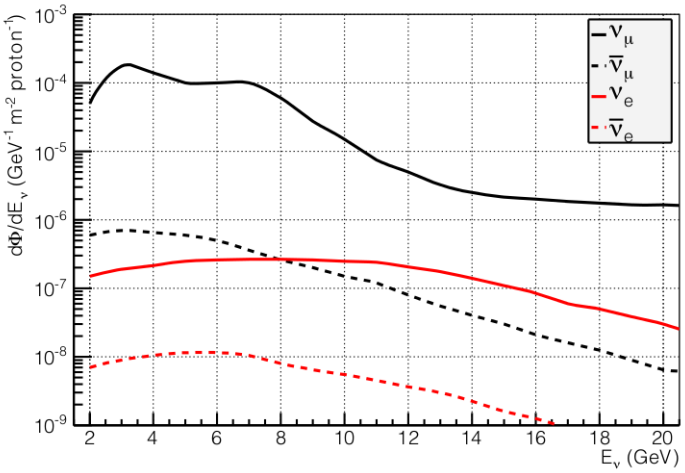

Figure 3.4: Profile of the Neutrino Beam used for the SKAT experiment [22].

pulse. A proposed upgrade indicates a repetition rate of 0.2 Hz and $2.2 \cdot 10^{14}$ protons per pulse. Assuming three years of operation, with six month running time per year and a beam efficiency of about 50 % the accelerator is able to produce 10^{21} protons on target. An also planned extension for the decay pipe to about 300 − 400 m would furthermore increase the amount of neutrinos within the beam up to 150 % of the initial value [22].

3.3 The Neutrino Detector

In this section a closer look at the neutrino detector is taken. After the detection principles of a megaton underwater Cerenkov neutrino detector have been introduced a successfully operating example, the ANTARES detector will be discussed briefly. Afterwards the KM3NeT project and ORCA, which is the proposed target for a neutrino beam from Protvino, are presented.

3.3.1 Principle of a megaton Cerenkov detector

Since neutrinos do only interact via the weak force and have a very small cross section it is extremely difficult to detect such particles and even more challenging to determine direction, energy or even the neutrino flavour.
The principle of all neutrino detectors so far is to measure secondary particles created in a neutrino reaction and then try to reconstruct information about the initial neutrino. The very small cross section of neutrinos demands very large detector masses and instrumented volume in order to get as many neutrino reactions within a detector as possible. For artificial neutrino sources an intensity as high as possible is crucial.
The principle of a megaton underwater Cerenkov detector therefore is to instrument a large volume of sea water with photomultipliers (PMTs) and to measure Cerenkov light which is produced by high energetic secondary particles created

in neutrino reactions.
Cerenkov light is produced when electrical charged particles travel through a dielectric medium with a greater speed than light would have traveling through the same material. The minimal energy for a particle being able to emit Cerenkov light dependent on the particle mass is

$$E_{min} = \gamma m c_0 \tag{3.7}$$

$$\gamma = \frac{1}{\sqrt{1 - \frac{v^2}{c_0^2}}} \rightarrow \frac{1}{\sqrt{1 - \frac{1}{n^2}}} \tag{3.8}$$

$$\text{with} \quad v = c_{H_2O} = \frac{c_0}{n}, \tag{3.9}$$

where n is the refraction index of the material ($n_{H_2O} = 1.33$). Another property of Cerenkov light is that it is emitted under a certain angle Θ with respect to the direction of flight of the causing emitting particle (see figure 3.5).

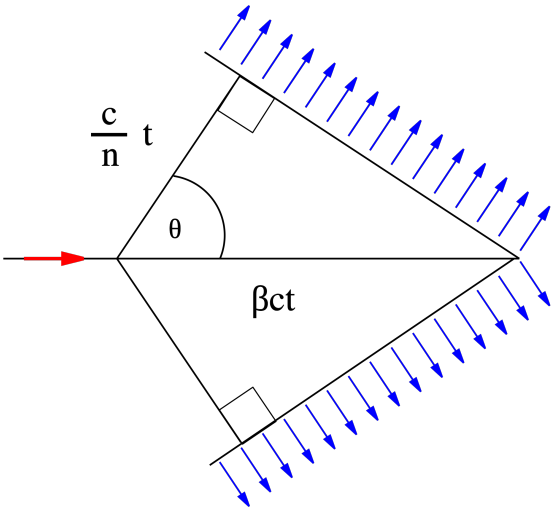

Figure 3.5: Schematic view of a charged particle emitting Cerenkov light with an angle of Θ (ideal case with no dispersion) [2].

The value of Θ depends on the energy of the particle:

$$cos(\Theta) = \frac{c}{nv} \tag{3.10}$$

For very high energetic particles Θ takes a constant value:

$$E >> E_0 = mc^2 \Rightarrow \frac{v}{c_0} \approx 1 \Rightarrow cos(\Theta) \rightarrow \frac{1}{n} \tag{3.11}$$

So, for water with a refractive index of $n_{H_2O} = 1.33$ $\Theta \approx 41.25°$.
To gain information about neutrinos by measuring secondary particles it is crucial to know what reactions might occur within the detector and how signatures

of secondary particles look like. Neutrinos can interact via the exchange of a charged $W^{\pm}$ boson (CC reaction) or a neutral Z^0 boson (NC reaction), but since only in CC reactions leptons are amongst the secondary particles NC reactions are not further discussed at this point.
The most common reaction of a neutrino is a charged current reaction with a nucleus of the detector material :

$$\nu_\alpha + X \xrightarrow{W^{\pm}} \alpha + A \tag{3.12}$$

Here α is the corresponding lepton depending on the neutrino flavour, so α is either an electron, a muon or a tauon. X is the hadronic reaction partner and A is representative for all hadronic secondary particles.
Independent of the neutrino flavour all CC reactions with a nucleus cause a hadronic shower within the detector. The size of the hadronic shower depends strongly on the value of Bjorken Y (B_y) which is the ratio of the energy within the hadronic shower E_{shower} divided by the available energy E: $B_y = E_{shower}/E$. In order to resolve the individual particles within the hadronic shower the PMTs need to be very close to each other. The detector layouts used for this thesis, and for experiments like ANTARES, have distances of some meters between various PMTs, hence the resolution of individual particles of the hadronic shower seems not possible at the moment. Therefore a hadronic shower is seen as a bright point like light source within the detector, which is used in order to reconstruct the vertex and time of an event.
The situation for leptonic secondary particles, however, is quite different. The reactions leptonic particles cause in water depend strongly on the lepton flavour, thus it makes sense to take a look at each lepton individually.
For an electron with a mass of 0.511 MeV ([7]) a minimum energy of 0.775 MeV is required to produce Cerenkov light while traveling through water (see equation 3.8). Nevertheless, Cerenkov light is not the only phenomenon which is caused by high energetic electrons with energies on the order of some GeV traveling through water. Most energy is lost due to the formation of an electromagnetic cascade. Via bremsstrahlung high energetic photons are created which can then decay into an electron positron pair, which also experiences energy loss due to bremsstrahlung. As long as the photon energy E_γ is above $E_{thr} = 2m_e \approx 1.022\,\text{MeV}$ pair production can occur and as long as the so produced electrons and positrons have an energy above the Cerenkov threshold they produce Cerenkov light.
In order to describe the formation of an electromagnetic shower the simple model from W.Heitler is used [17]. The radiation length of an electron in water is approximately 36 cm, so after the electron traversed one radiation length one electron positron pair is produced until the energy drops to a value below $E_{min} = 70\,\text{MeV}$. After that other processes like ionization and excitation become dominant. In this context it is interesting to know how many radiation lengths an electron can cover until it no longer emits Cerenkov radiation. With the assumption that the amount of particles is $N(n) = 2^n$, where n is the number of radiation lengths the electron has covered, and that the energy is distributed equally under all particles one obtains

E_0/GeV	n	L/m
2.0	11.33	4.08
5.0	12.66	4.56
10.0	13.66	4.92

Table 3.1: Maximal track lengths L for electrons causing a electromagnetic cascade in water

$$E_0 = 2^n E_c \Rightarrow n = \frac{\ln(E_0/E_c)}{\ln(2)}, \tag{3.13}$$

where E_0 is the initial Energy of the electron, E_c is the minimal energy for Cerenkov radiation and n is the number of radiation lengths [27]. In table 3.1 the maximal track lengths for electrons in water are calculated by using this simple model. So, in order to identify electrons with an energy of some GeV it is useful to look for track lengths in a range of $4 - 5\,\mathrm{m}$.

The situation for muons however is quite different. Muons have a mass of $m_\mu = 105.7\,\mathrm{MeV}$ ([7]) therefore an energy of 160 MeV is need so that the muon is able to emit Cerenkov radiation. Although the same processes (ionization, bremsstrahlung, excitation) occur when a muon propagates through matter the cross sections for each process are quite different. Therefore bremsstrahlung and pair production are not the dominant effect for energy loss. While the possible track length for electrons grows only logarithmically the relation between track length and energy for muons can be approximated as $-dE/dx = a + bE$ [13]. At a muon energy of some GeV a rough approximation is $\approx 5\,\mathrm{m/GeV}$. An electron with an initial energy of 5.0 GeV for example can cover approximately 5 m in water before the energy is below the Cerenkov limit, but a muon can propagate as far as 25 m before it stops emitting Cerenkov photons. This property of muons can be used to identify muons in water.
In contrast to electrons muons are not stable particles, but can decay into electrons via $\mu^- \to e^- \overline{\nu_e} \nu_\mu$ (analogue for antiparticles) with a branching ration of almost 100 % and a lifetime of approximately $\tau \approx 2.2 \cdot 10^{-6}\,\mathrm{s}$ [7].
The heaviest leptons discovered so far are tauons with a mass of $m_\tau \approx 1.78\,\mathrm{GeV}$ ([7]) and a lifetime of $\tau \approx 3.0 \cdot 10^{-17}\,\mathrm{s}$. A tauon needs an energy of 2.70 GeV to be able to radiate Cerenkov light in water. The extremely short mean life time makes it very hard to detect tauons before they decay. The branching ration for a decay into an electron is $\approx 17.4\,\%$ and into a muon $\approx 17.9\,\%$, so almost equal, but the biggest branching ration however is the decay into two pions ($\tau \to \pi^- \pi^0 \nu_\tau$) with a value of $\approx 25.5\,\%$. Pions are the lightest mesons and since they are hadronic particles it is very likely that they will cause a hadronic cascade in water for a initial tauon energy of some GeV. The interaction length for hadrons is approximately 85 cm [7]. Thus the most promising idea for the identification of tauons is to look for so called "two-bang-events", so events with two bright point like light sources which are not too far apart in space and time. In order to shut out any disturbing other light sources (e.g. the sun) the detector has to be placed within a dark surrounding. In the following examples the detectors are placed on the ground of the sea, which is technically extremely

challenging, but brings the advantage that a huge detector mass can be instrumented without the necessity and the limitation of building some sort of tank within a building.
Since 2007 the ANTARES (Astronomy with a Neutrino Telescope and Abyss environmental RESearch) detector operates successfully on the ground of the Mediterranean Sea, 40 km off the French coast at 42°50′ N, 6°10′E, whose main goal is to measure cosmic neutrinos with an energy greater than 50 GeV [18]. The detector is an array of about 885 photomultipliers (PMTs) arranged in 12 vertical lines with an approximate instrumented volume of 0.01 km^3 at an depth of 2.5 km. For ANTARES the PMTs were put into a pressure resistant glass sphere which is called an optical module (OM). Three OMs assembled on a mechanical structure facing downwards at an angle of 45° makes a storey. One normal line contains 25 storeys with a distance of 14.5 m and 100 m distance between seabed and first storey. At the bottom each line is anchored to the seabed and at the top a buoy holds the line at a vertical position. The signals from each line is first collected at a junction box at the bottom of the sea and then send to the shore station. In order to get information about the current status of the lines and the surroundings an additional line has been installed (IL07). In figure 3.6 a schematic illustration of the ANTARES detector can be seen.

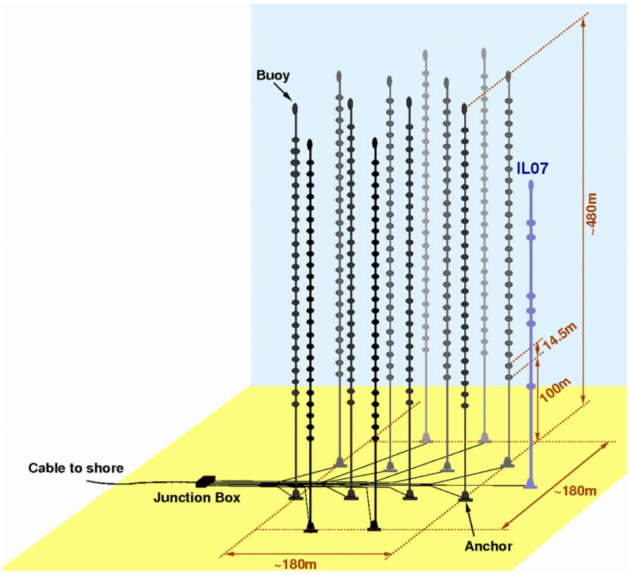

Figure 3.6: Schematic illustration of the ANTARES neutrino detector [9]

With this detector design it is possible to detect neutrinos with an energy as low as 20 GeV [9].

3.3.2 The ORCA Project

As a successor to the ANTARES detector the construction of a multi-cubic-kilometer detector KM3NeT has been started [28]. The main goal is the detection of cosmic high energetic neutrino sources. KM3NeT consists of three neutrino telescopes at three different sites within the Mediterranean Sea. Each detector contains 115 strings with 18 storeys and one optical module per storey. The optical modules for KM3NeT, however, are different from the ones used for ANTARES. Each optical module contains 31 3" PMTs which are quasi isotropically distributed within the glass sphere (see figure 3.7).

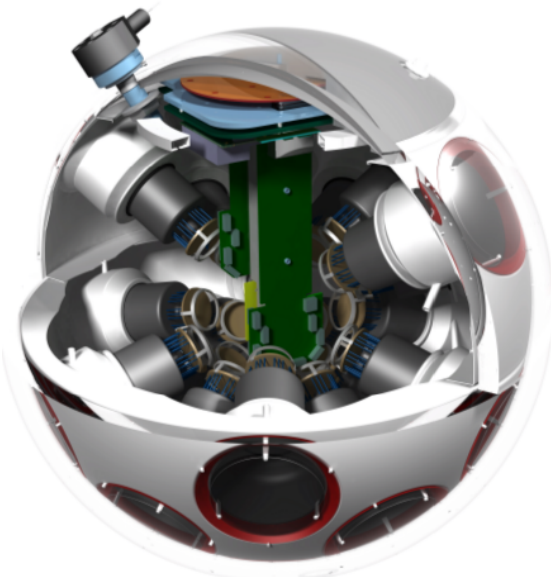

Figure 3.7: Schematic picture of the Digital Optical Module (DOM) used for KM3NeT with a total of 31 PMTs [28]

Within this project one detector is planed to be instrumented with a higher photomultiplier density. A higher density of photomultipliers allows a Cerenkov detector to be more sensitive to neutrinos with lower energies and allows for a higher energy and direction resolution thus leading to better flavour identification. The main goal of ORCA (Oscillation Research with Cosmics in the Abyss) is to use this densely instrumented volume and atmospheric neutrinos to probe the neutrino mass hierarchy. A temporary detector design consists of 50 strings with a mean distance of about 20 m. Each string counts 20 optical modules with a distance of 6 m. In total the instrumented volume is $1.75 \cdot 10^6\,\mathrm{m}^3$ which corresponds to a mass of approximately 1.8 MTon of sea water. A footprint of the detector and an artist's view of a string can be seen in figure 3.8.
A preliminary result from the current feasibility study for the effective mass for ν_μ charged current reactions within the detector is shown in figure 3.9.
Since the atmosphere is used as neutrino source it is not only important to know the neutrino flavour and energy, but also from which direction the neutrinos came from in order to determine the distance between neutrino source and

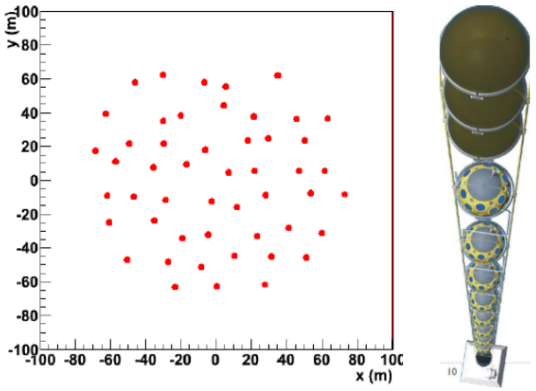

Figure 3.8: Footprint of the ORCA detector used in the feasibility study (left) and an artist's view of a string containing digital optical modules(DOM) [31]

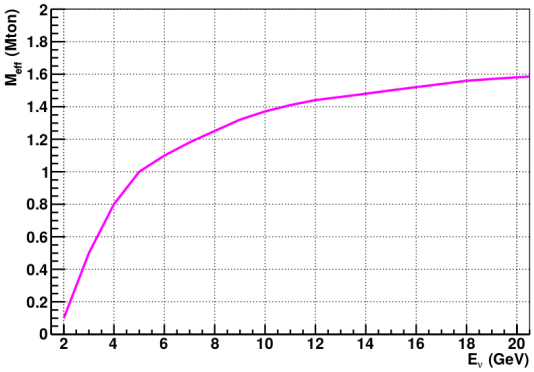

Figure 3.9: Preliminary result for the effective mass for the detection of ν_μ charged current reaction within the instrumented volume [22]

interaction vertex. The latest results indicate a significance of $3-5\sigma$ for the exclusion of one mass hierarchy after an exposure of 20Mton·year [31].
A possible site for the ORCA detector is near the ANTARES detector which would yield a baseline of 2588 km to the particle accelerator in Protvino. Another possible location would be within the Ionian Sea off the Sicilian coast and results in an almost identical baseline (with a difference of about 1 %) [22]. The dense detector layout, which enables accurate measurements of secondary particles from neutrino interactions with an energy of some GeV and the ideal distance to the source of a neutrino beam highly qualifies the ORCA detector as a target for a long baseline neutrino experiment.

3.4 Expected event rates

At this point it is interesting to calculate the expected event rates for both mass hierarchies. For CC reactions the number of events for a flavour α is (from [22]):

$$\begin{aligned}\frac{dN_\alpha}{dE_\nu} =& N_{pot}\left(\frac{l_{SKAT}}{l_{LBL}}\right)^2 \frac{M_{eff}(E_\nu)}{m_p} \\ & \left[\sigma^{CC}_{\nu_\alpha}\left(\frac{d\Phi_{\nu_\mu}}{dE_\nu}P_{\mu\alpha}+\frac{d\Phi_{\nu_e}}{dE_\nu}P_{e\alpha}\right)\right]+\left[\sigma^{CC}_{\bar{\nu}_\alpha}\left(\frac{d\Phi_{\bar{\nu}_\mu}}{dE_\nu}P_{\overline{\mu\alpha}}+\frac{d\Phi_{\bar{\nu}_e}}{dE_\nu}P_{\overline{e\alpha}}\right)\right]\end{aligned} \tag{3.14}$$

Here $l_{SKAT} = 245\,\text{m}$ is the distance between proton target and the SKAT bubble chamber and $l_{LBL} = 2600\,\text{m}$ the distance between target and detector site, M_{eff} the effective mass of the detector, m_p the proton mass, Φ_{ν_α} the respective flux and $P_{\alpha\beta}$ is the oscillation probability for a transition from ν_α to ν_β. For NC reaction a similar event rate can be calculated, but the effective mass is evaluated for $E_\nu/2$ since on average half of the energy from a NC reaction is transferred to the outgoing neutrino:

$$\begin{aligned}\frac{dN}{dE_\nu} =& N_{pot}\left(\frac{l_{SKAT}}{l_{LBL}}\right)^2 \frac{M_{eff}(E_\nu/2)}{m_p} \\ & \left[\sigma^{NC}_{\nu}\left(\frac{d\Phi_{\nu_\mu}}{dE_\nu}+\frac{d\Phi_{\nu_e}}{dE_\nu}\right)\right]+\left[\sigma^{NC}_{\bar{\nu}}\left(\frac{d\Phi_{\bar{\nu}_\mu}}{dE_\nu}+\frac{d\Phi_{\bar{\nu}_e}}{dE_\nu}\right)\right]\end{aligned} \tag{3.15}$$

Since the cross section for NC reaction are approximated to be independent of the neutrino flavour in this context (see eq. 3.4) the event rate for NC reaction is independent of the oscillation probabilities.
In table 3.2 the event rates for both mass hierarchies for an energy range of $2-20\,\text{GeV}$, the effective mass approximation from figure 3.9 and fluxes according to the expected beam profile (figure 3.4) are summarized. A distinction between two event topologies is made, namely track like events and cascade like events. Track like events in this scenario are all ν_μ CC interactions, whereas cascade like events are ν_e CC interactions. All ν_τ and NC events are considered as background (BG).
The biggest difference between the two hierarchies lies within the number of cascade like events. By comparing these two numbers one obtains that the statistical separation of both hierarchies is better than $20\,\sigma$. A more advanced

Event	Track NH	Track IH	Cascade NH	Cascade IH
N	10317	10015	1366-1876	397-597
BG	227-231	245-248	5807-5830	5895-5908
Total	10543-10548	10260-10263	7196-7683	6304-6492

Table 3.2: Event numbers for normal and inverted hierarchy for varying Θ_{CP} and $N_{pot} = 10^{21}$ [22]

event rate calculation under consideration of misidentification of events and detector systematics can be found in [22].

Chapter 4

Algorithm for the distinction of muon and electron neutrino events

In this chapter the algorithm, which was developed during this master thesis, will be described in detail. Furthermore two detector layouts, which were used for the event simulation, will be introduced and the process chain for the event simulation will be explained. The last section illustrates the integration of a machine-learning tool which was used in combination with features calculated by the track length reconstruction and four additional features in order to classify neutrino events in two categories, ν_e events and ν_μ events.

4.1 Detector layouts

Detector layout refers to the three dimensional arrangement of optical modules. The optical modules for the here used layouts are according to KM3NeT technology, so 31 3" PMTs quasi isotropically distributed within a glass sphere (see fig. 3.7).
For this thesis two layouts are important, namely the dense detector layout and the cuboid layout. Both layouts are impractical for a real detector since the strings are too close to each other, 3 m distance for the dense detector layout and 6 m for the cuboid layout.
The dense detector contains 2181 Strings, arranged in a octagonal form (see fig. 4.1), with 51 optical modules each with a distance of 3 m from one another. Each optical module contains 31 PMTs which yields a total of 3448161 PMTs. Within the dense detector the distance between two optical modules is always 3 m in x- ,y- and z-direction.
Although the dense detector is unrealistically big and densely instrumented to be realized it served two important purposes. On the one hand, it was used as the primary detector layout for the event simulation in this thesis. If a photon, created within the simulation tool, flies into a PMT and is detected it does not disappear, meaning that it can propagate further through the detector and might be detected by another PMT, producing another hit (detected photon).

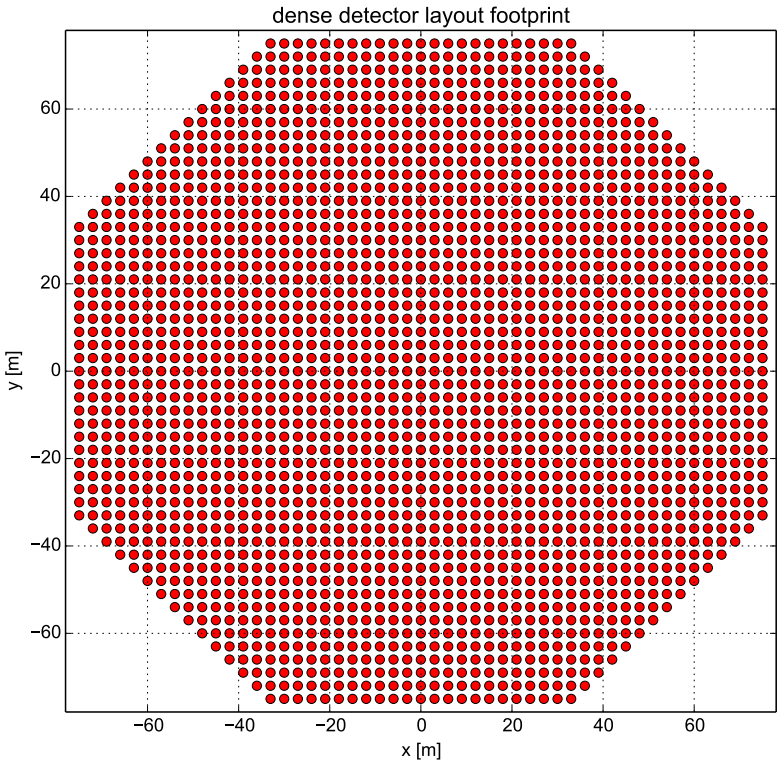

Figure 4.1: Footprint of the dense detector layout containing 2181 strings

This effect leads to about 30 % more hits for the dense detector layout than would be obtained if a photon disappears after it has been detected, but brings the advantage that any other detector layout, which is completely contained in the dense detector layout, can use the same simulated events. For the conversion between dense detector layout to another it is just necessary to cut out all hits which are on optical modules not contained within the new layout. Depending on the amount of PMTs within the new layout the excess of hits drops rapidly. On the other hand the dense detector layout was used for the first analysis of simulated muon and electron neutrino events in order to get a first idea of how events within an energy range of $2 - 10\,\mathrm{GeV}$ from a neutrino beam would look like and how a distinction might work.

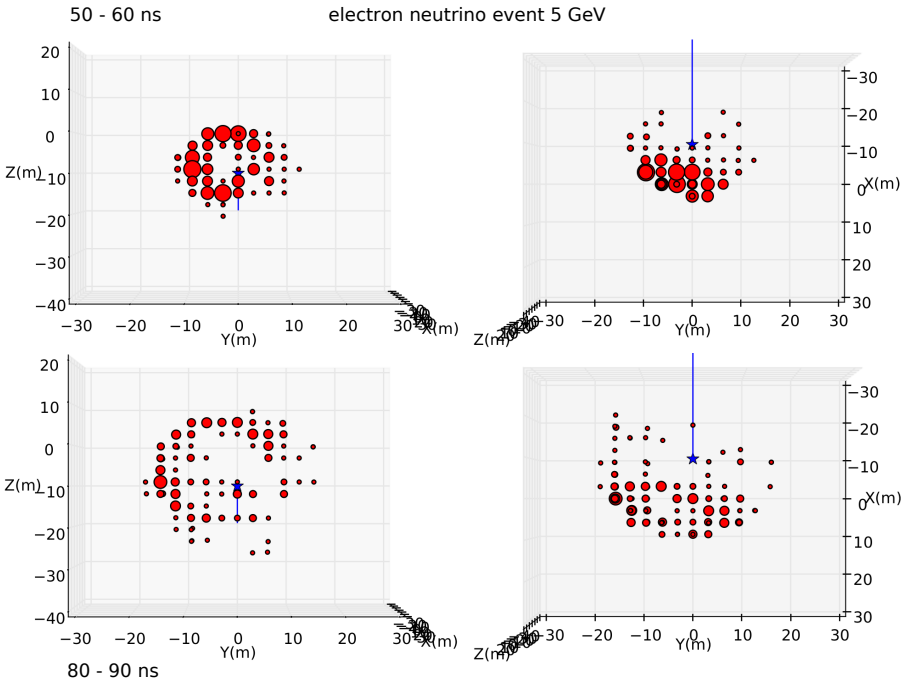

Figure 4.2: Hits (red dots) of an electron neutrino event with E=5 GeV for front view (left column) and top view (right column) for time windows of 50 to 60 ns (top row) and 80 to 90 ns (bottom row) within the dense detector. The blue line represents the neutrino beam and the position of the vertex is marked with the blue star.

In figure 4.2 and 4.3 the hits of an electron neutrino event and in figure 4.4 and 4.5 the hits of a muon neutrino event with an initial neutrino energy of 5 GeV are shown. Each figure contains four plots. The top row plots of figure 4.2 and 4.4 represent all hits within a time window of 40 to 50 ns, while the bottom row shows all hits within 80 to 90 ns after the interaction. Furthermore two different viewing angles are chosen, a front view for the left column and a top view for the right column. Figure 4.3 and 4.5 contain the same events with the same

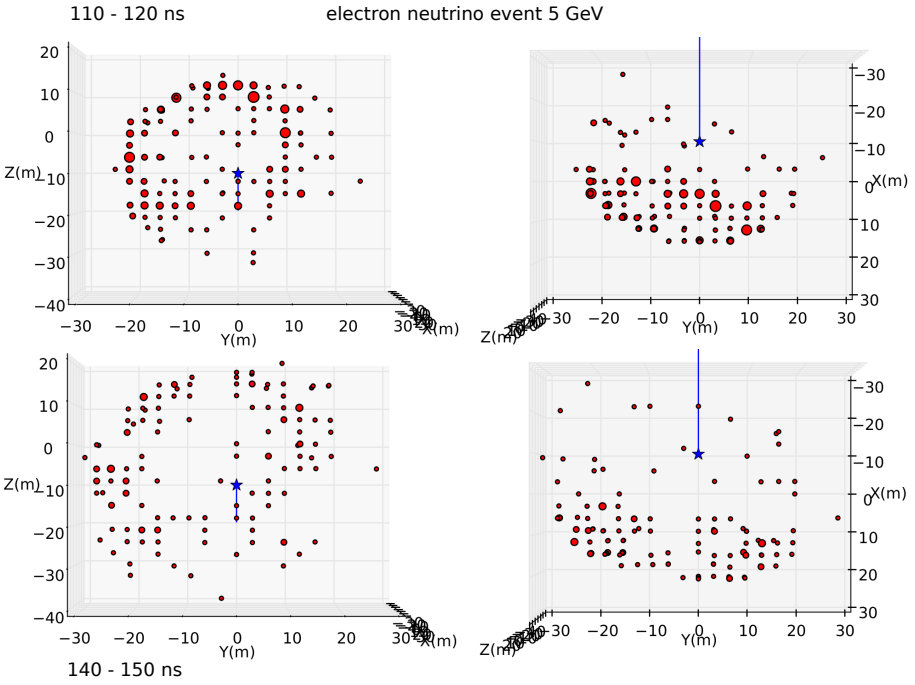

Figure 4.3: Hits (red dots) of an electron neutrino event with E=5 GeV for front view (left column) and top view (right column) for time windows of 110 to 120 ns (top row) and 140 to 150 ns (bottom row) within the dense detector. The blue line represents the neutrino beam and the position of the vertex is marked with the blue star.

point of view but for later time intervals, 110 to 120 ns for the top row and 140 to 150 ns for the bottom row. Each red dot represents an optical module with a hit within the respective time window. The size of each dot is connected to the amount of hits which were detected within the time window. In addition the neutrino beam, represented by the blue line, and the interaction vertex, marked with a blue star, are drawn into the plots.

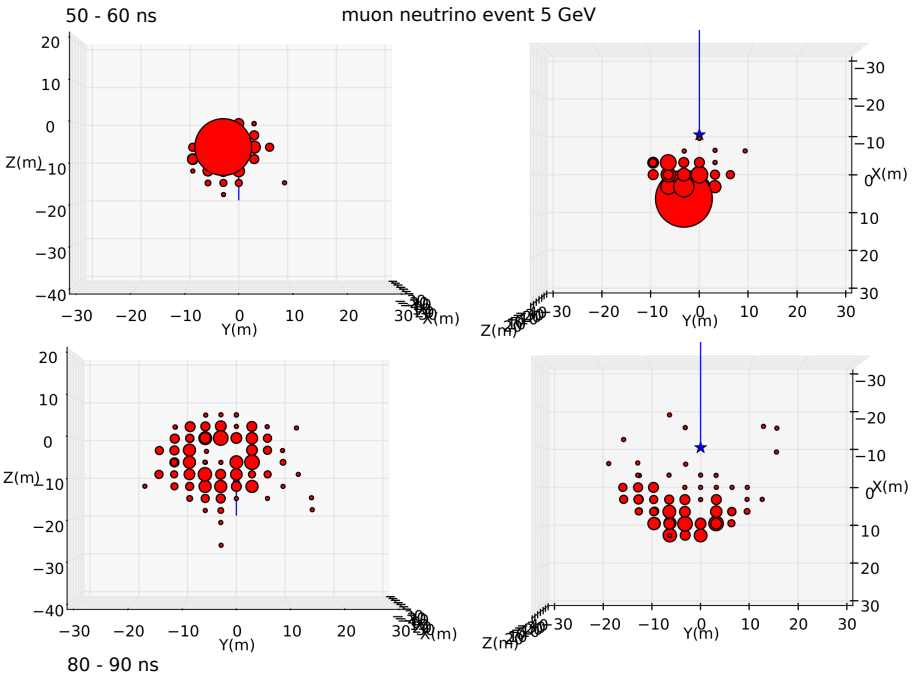

Figure 4.4: Hits (red dots) of a muon neutrino event with E=5 GeV for front view (left column) and top view (right column) for time windows of 50 to 60 ns (top row) and 80 to 90 ns (bottom row) within the dense detector. The blue line represents the neutrino beam and the position of the vertex is marked with the blue star.

For both event types circle like structures, Cerenkov rings, can be recognized. The most interesting fact however yields the comparison of the plots for the 40 to 50 ns time window. In figure 4.2 the top left plot clearly shows a hollow circle. This suggests that the emitting particle for Cerenkov light already disappeared, with the consequence that the top of the Cerenkov cone is missing. This also can be seen in the right plot of the top row. If the emitting particle would not have vanished already, the top of the Cerenkov cone would be visible, causing the hits from the top view to resemble a triangle. This is not surprising, since an electron would have covered a distance of approximately 12 m at this time, which is extremely unlikely within this energy range. If a closer look is taken on the top plots of figure 4.4 it can be seen, that the Cerenkov ring (left plot) is still filled, and the Cerenkov cone (right plot) is still in possession of its top

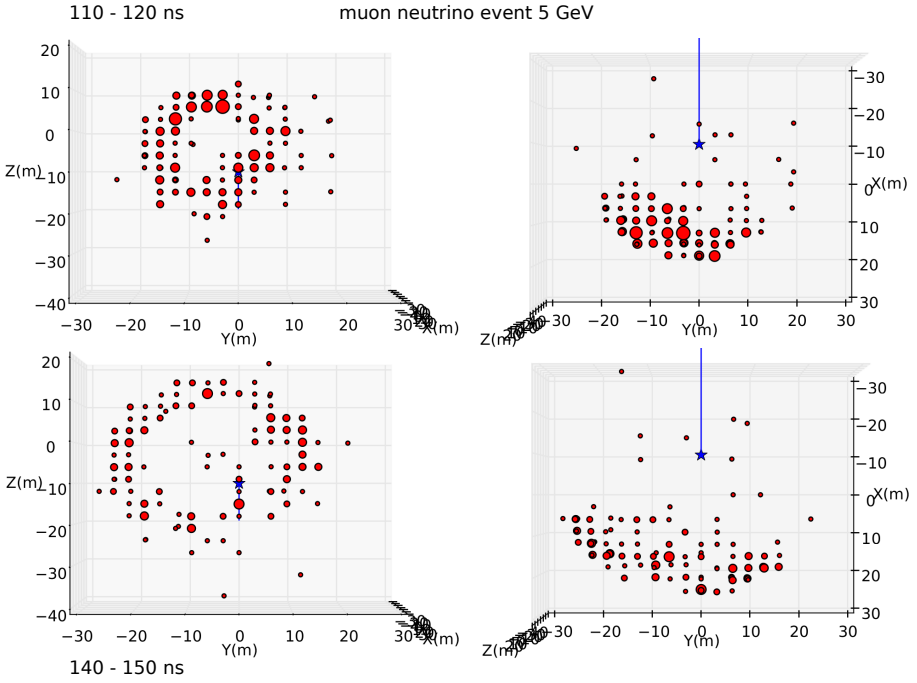

Figure 4.5: Hits (red dots) of a muon neutrino event with E=5 GeV for front view (left column) and top view (right column) for time windows of 110 to 120 ns (top row) and 140 to 150 ns (bottom row) within the dense detector. The blue line represents the neutrino beam and the position of the vertex is marked with the blue star.

part. This leads to the assumption that the emitting particle, a muon, has not disappeared 40 ns after the interaction. A lifetime of 40 ns corresponds to a track length of 12 m, which is quiet possible for muons with an energy of 5 GeV. Another difference can be seen for the 80 to 90 ns front view plots. The hole within the Cerenkov ring is much bigger for the electron neutrino event than for the muon neutrino event, which is also a consequence of the early disappearance of the electron. Thus, the muon is much longer capable of emitting Cerenkov photons. The information gained from the analysis of such events led to the idea of a lepton track length reconstruction by analyzing Cerenkov rings which will be discussed in detail in section 4.3.
The second important detector layout is the cuboid layout containing 357 strings with 26 OMs per String, which leads to 9282 OMs and 287742 PMTs in total. Within the cuboid layout the distance between two optical modules in x-, y- and z-direction is 6 m. The footprint of the cuboid layout is shown in figure 4.6. By comparison of figure 4.1 and 4.6 it can be seen, that the cuboid layout is completely contained within the dense layout, but less densely instrumented. The amount of PMTs within the cuboid layout is only about 8.3 % of the number of PMTs within the dense layout. The reason for the introduction of the cuboid layout is obviously the smaller amount of PMTs, which is directly linked to the needed computational resources (memory, cpu time, hard drive storage). Furthermore the vertex- and track reconstruction, which were used, were not designed for such large detector layouts. Therefore the cuboid layout was used for the whole analysis within this thesis, so every result presented is based on this layout, if not explicitly stated otherwise.

4.2 Event simulation

The simulation of events, which were used for the efficiency analysis, is a sequence of six different steps. These steps shall be discussed within the following section.
The first stage of a simulated event is a file containing the following information:

- vertex position and time,
- energy and direction of the initial neutrino,
- energy, direction and particle type for every secondary particle produced within the interaction,
- interaction type (CC or NC),
- production channel (elastic, inelastic, etc.),
- target particle,
- Bjorken X and Y.

These files, to which from now on is referred to as event input files, were produced with the GENIE tool ([3]) and were already available when the work on this thesis started.
The first processing step was to get events within the desired energy range and to rotate the direction from the initial neutrino direction in a way that

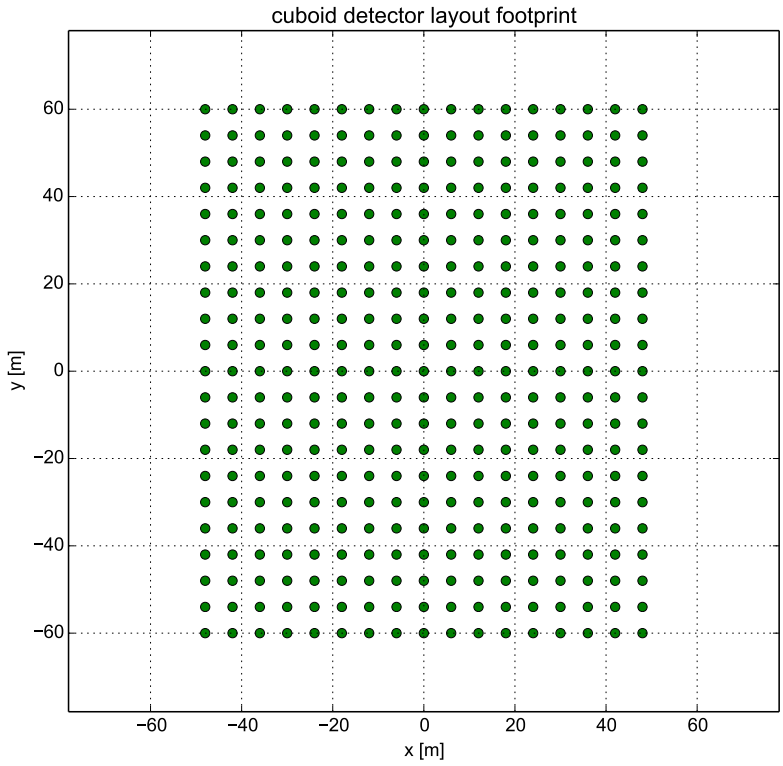

Figure 4.6: Footprint of the cuboid detector layout containing 357 strings

it represents a neutrino coming from a neutrino beam. Since the distance between detector and neutrino beam source is approximately 2600 km the earth curvature causes a beam inclination of 11.7° at the detector site. Detector layout and neutrino beam are arranged so that the neutrino beam direction is $[0.979, 0.000, 0.202]$ (x-, y-, z-value within the coordinate system used in 4.6). The angular difference for beam neutrinos arriving at the detector can be calculated with $\alpha/2 = \arcsin(220\,\text{m}/2600\,\text{km}) \approx 0.005°$, where 220 m is the maximal range on the y-axis for vertices (detector surface facing in beam direction plus 50 m in each direction). Therefor the angular variation of beam neutrinos can be neglected.
In order to contain the integrity of the event all secondary particles have to be rotated by the same operation. The rotation matrix is defined as

$$R_{\vec{n}}(\alpha)\vec{x} = \vec{n}(\vec{n}\cdot\vec{x}) + \cos(\alpha)(\vec{n}\times\vec{x})\times\vec{n} + \sin(\alpha)(\vec{n}\times\vec{x}), \tag{4.1}$$

$$\text{with } \vec{n} = \frac{(\vec{d_\nu}\times\vec{d}_{beam})}{|(\vec{d_\nu}\times\vec{d}_{beam})|} \tag{4.2}$$

$$\text{and } \alpha = \arccos\left(\frac{\vec{d_\nu}\cdot\vec{d}_{beam}}{|\vec{d_\nu}||\vec{d}_{beam}|}\right), \tag{4.3}$$

where $\vec{d_\nu}$ is the initial neutrino direction and $\vec{d}_{beam}$ is the beam direction, so that $R_{\vec{n}}(\alpha)\vec{d_\nu} = \vec{d}_{beam}$.
Nine small energy ranges where chosen for which events were simulated, namely 2, 3, 4, 5, 6, 7, 8, 9 and 10 GeV with a range of ±2.5 % for each mean value. These values were chosen in order to be able to get energy dependent results for beam neutrino events, which have an energy between 2 and 10 GeV (see fig. 3.4).
The so preprocessed event input files, correct energy range, neutrino direction rotated to beam direction and secondary particles rotated accordingly were then further processed by the KM3Sim tool, which simulates hits for each event within the dense detector layout. The so produced hits are added to the files. For each hit the identification number of the PMT, the hit time, the number of photons which caused the hit and the particle which created the photon is amongst other information added. After this point the event simulation for the dense detector layout without noise simulation would be done.
In order to get simulated events for the cuboid layout further steps have to be carried out. As mentioned before, the cuboid layout is completely contained within the dense detector layout. This means that for a conversion of a simulated event all hits which occurred on PMTs not available in the cuboid layout have to be removed form the files. This is achieved with two geometry files, one for each layout, which assigns each PMT id to a geometrical position, so each hit which occurred on a PMT also contained in the cuboid layout is kept, all other hits are removed. Since the amount of PMTs changes it is useful to change the PMT id as well after the needless hits have been removed.
The next step is to remove all hits which were registered later than 2000 ns after the initial neutrino interaction happened. This is done because of two important reasons (at this point no noise has been added to the simulations).
One is that a photon which is detected 2000 ns after the event, is either scattered light, so most information about the initial event is lost, or has propagated about 600 m without any interaction, which is extremely unlikely. Furthermore,

the detector layouts are not big enough to be able to use such photons, even if the vertex would be 100 m outside of the detector a photon could only cover a distance of about 400 m before leaving the detector (removing late hits for an event is also done within the ANTARES project, but with a time window of ± 2500 ns around the approximated interaction time). The other reason is connected to the following processing step.
In order to make the simulated events more realistic, hits are added which are not caused by particles created within the neutrino interaction. The biggest source for background hits, or noise, is the radioactive decay of ^{40}K which is present in sea water. The potassium 40 isotope is unstable and can decay via the β^+ or the β^- channel. In both cases however relativistic electrons or positrons are created, which radiate Cerenkov light while propagating through water. When such a potassium decay occurs within the detected volume the Cerenkov light is detected. For the PMTs used for the KM3NeT detectors the noise rate equals approximately 9500 Hz. For the simulation of noise hits the "k40" tool was used, which was written by Salvatore Galatà. Noise hits within a time window of 1000 ns before the first hit of the event and 1000 ns after the last hit of the event with a noise rate of 9500 Hz and a coincidence time of 500 ns were added to the events. So, if extremely late hits would still be present within the event files, a huge amount of noise hits would be simulated, causing the files and needed cpu time for further processing and reconstruction steps to be extremely large.
After this step the event simulation is finished and the so produced files are used for the efficiency analysis and other calculations within this thesis. To get results as detailed as possible two event samples have been simulated, namely premium events(PE) and normal events(NE). For each sample simulations with and without noise were used. Events are referred to as premium events when the interaction vertex is within a small area within the left half of the detector. The minimal and maximal values for each dimension for premium events are: $(x_{min}, x_{max}) = (-36\,\text{m}, -12\,\text{m})$, $(y_{min}, y_{max}) = (-12\,\text{m}, 12\,\text{m})$ and $(z_{min}, z_{max}) = (-12\,\text{m}, 12\,\text{m})$. The reason for the production of this event sample is to get events, which are completely contained within the instrumented volume in order to extract as much information about the event as possible.
Normal events are then events with a vertex anywhere within the detector and a distance up to 50 m in x- and y-direction and 40 m in positive z-direction. The possible vertex positions for normal events are within the following ranges: $(x_{min}, x_{max}) = (-98\,\text{m}, -98\,\text{m})$, $(y_{min}, y_{max}) = (-110\,\text{m}, 110\,\text{m})$ and $(z_{min}, z_{max}) = (-75\,\text{m}, 115\,\text{m})$. Normal events are produced to test the classification algorithm for a more realistic sample of events, so contained and semi contained events. The amount of events for each sample and energy class is listed in table 4.1.

4.3 Separation principle

The following section describes in detail the basic idea used for the algorithm designed for the distinction of muon and electron neutrino events.
The main idea used for a separation of ν_e and ν_μ events within a energy range of $2 - 10\,\text{GeV}$ is the track length of the secondary leptons produced in a charge current reaction. As described in section 3.3.1 the track length of a electron within a energy between $2 - 10\,\text{GeV}$ covers a distance of about $4 - 5\,\text{m}$ while a

mean energy [GeV]	2	3	4	5	6	7	8	9	10
ν_e PEnN	1133	1186	1162	1039	1180	1116	1092	1189	1198
ν_μ PEnN	1117	1142	1105	1150	1136	1079	1107	1173	1027
ν_e PEwN	1079	1142	1128	1023	1161	1100	1078	1176	1188
ν_μ PEwN	1058	1106	1079	1122	1123	1057	1093	1163	1013
ν_e NEnN	7236	7234	7267	7231	7227	7263	7218	7271	7228
ν_μ NEnN	7260	7318	7312	7311	7212	7311	7262	7256	7136
ν_e NEwN	6113	6412	6598	6675	6758	6860	6875	6976	6966
ν_μ NEwN	5918	6382	6614	6744	6758	6913	6901	6912	6856

Table 4.1: Amount of simulated events for each energy range and event sample type. The shortcut PE stands for premium event, NE for normal events, nN for no noise and wN for with noise.

muon with the same energy can propagate as far as $10 - 40\,\mathrm{m}$ before it decays or interacts. In order to reconstruct the distance a lepton covered within the detector Cerenkov light can be used. While propagating through water the high energetic leptons emit continuously Cerenkov photons with an angle of 41° with respect to the direction of flight.
Before the description continues it is useful to introduce some terms which will be used in the following section. A Cerenkov cone defines the geometrical position of the photons emitted due to Cerenkov radiation of a high energetic particle. Since the Cerenkov angle is approximately constant the Cerenkov cone looks very much the same for every particle, with the particle track as the directrix (the symmetry axis of a cone) and the particle at the very tip, also called the apex. For a cone to be unique seven parameters are necessary, e.g. directrix, apex and apex angle.
A Cerenkov ring is called the intersection of the Cerenkov cone with a plane, so geometrically a cone section. Cone sections can be circles, ellipses, parabolas and hyperbolas. Within this context only ellipses, and circles, as a special case of ellipses are considered. The reason for this is that the angle between secondary lepton and initial neutrino direction would need to be at least 37° ($90° - (12° + 41°)$) so that the conic section would no longer be an ellipse (41° equals the Cerenkov angle in water, 12° is the inclination of the neutrino beam). An angular difference between lepton and initial neutrino this big indicates a large B_y, which makes the reconstruction of lepton properties difficult.
If a photon is detected time and PMT identification number are stored. This unit is called a hit. The PMT id can then be connected to the PMT position and the direction of the PMT within the optical module. Within this thesis however the direction of the PMT is neglected and the position of a PMT is reduced to the center of the optical module.
A detector plane refers to all optical modules within a theoretical plane inside the detector, so all optical modules with a x-value of $-6\,\mathrm{m}$ for example. In figure 4.7 the Cerenkov cone of a lepton and a string with OMs is illustrated.
The basic idea of the distinction between muon and electron neutrino events is now to reconstruct Cerenkov rings within detector planes and with the help of a reconstructed vertex and track to calculate how far the emitting particle had to fly at least in order to produce the reconstructed Cerenkov ring. The amount of hits, which would fit such a ring and the time of each hit on a ring are stored

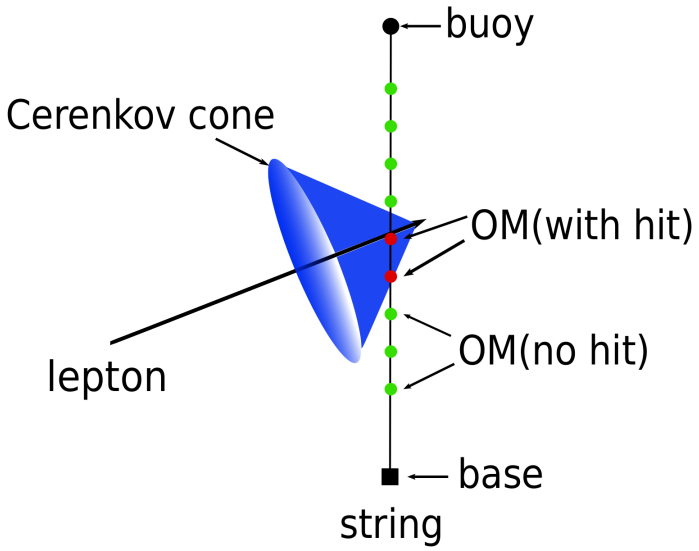

Figure 4.7: A lepton with its surrounding Cerenkov cone hitting optical modules (red dots) on a string

and will be used later for the classification process.
In figure 4.8 the connection between hits, which are part of a Cerenkov ring, and the lepton track is illustrated. In this figure the theoretical path for Cerenkov photons which were emitted at three different points on the lepton track can be seen.
Each point has a different distance to the plane, namely d_1, d_2 and d_3, which is directly connected to the size of the Cerenkov ring, or at figure 4.8 the distance between the hits on the string. If the very same situation would be rotated around the z-Axis and not just one string, but a lot of strings would be shown it would look like illustrated in figure 4.9.
Here also three different Cerenkov rings are shown, each refers to a different emitting position for the photons and the lepton track so ring 1 would match a emitting position for d_1, ring 2 for d_2 and ring 3 for d_3. The optical modules which are crossed by the ring are able to detect a hit and are therefore marked red. The green optical modules do not detect a hit since no scattered light and other light sources but Cerenkov light from one lepton is considered at the moment.
The idea for the track length reconstruction is now to get all hits within a detector plane, then with the knowledge of the track direction, from a track reconstruction, calculate the form of the Cerenkov ring on the plane for various distances d and then to count all hits, which match a certain ring and save the amount of hits for a certain distance. Finally it is possible to calculate a minimal track length with the help of a reconstructed vertex position. Then each track length and the amount of hits which were found to match this length are stored and used to classify each event.
With the knowledge of the lepton direction and the position of the plane it is

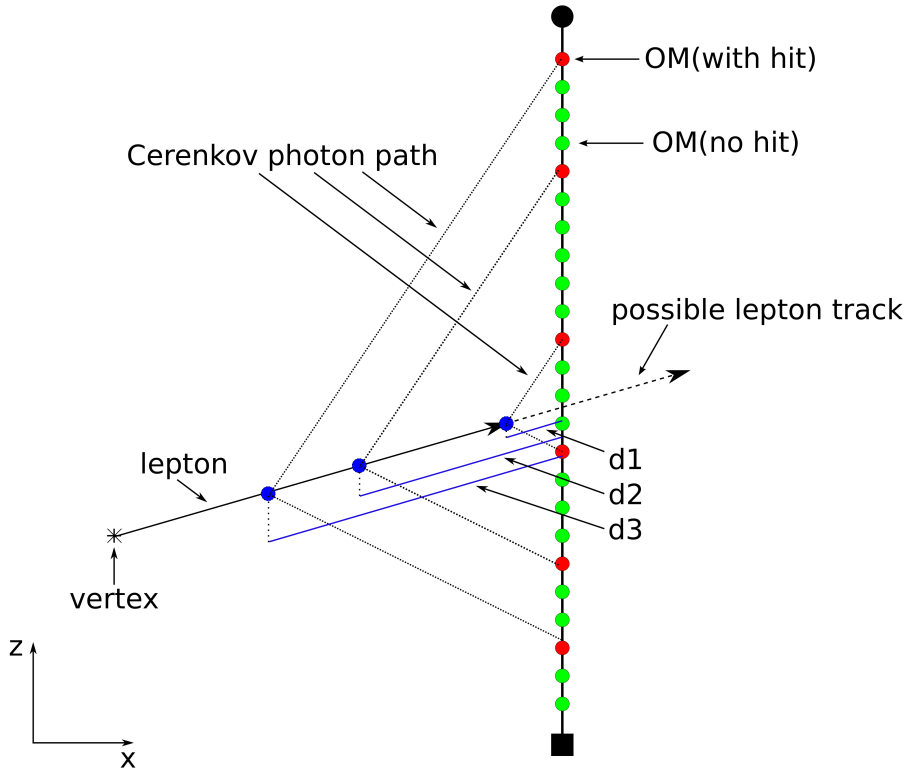

Figure 4.8: Schematic illustration of the connection between hits on a Cerenkov ring and the lepton track

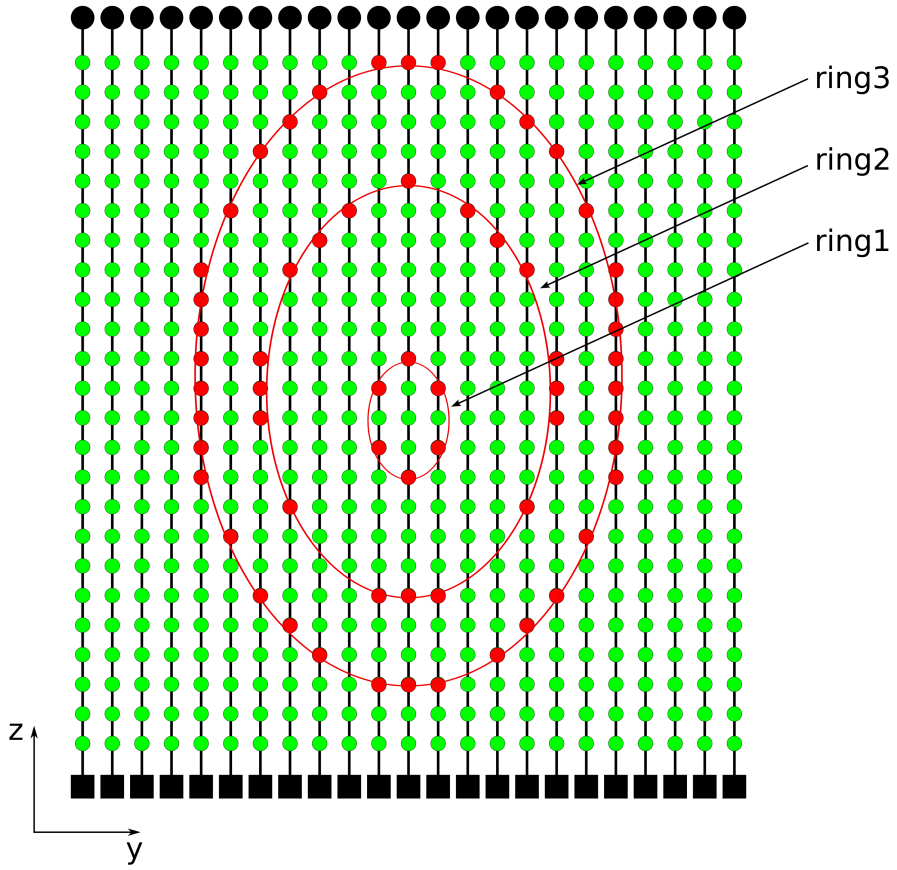

Figure 4.9: possible hits (red dots) from three different emitting distances within a detector plane

possible to calculate the parameters for the conic section within the plane. All points on the intersection have to solve the equation for the cone and for the plane. A cone can be defined as :

$$\cos(\theta) = \frac{(\vec{S} - \vec{X}) \cdot \vec{w}}{|\vec{S} - \vec{X}| \cdot |\vec{w}|}, \tag{4.4}$$

where θ is the apex angle, $\vec{S}$ the position of the apex and $\vec{w}$ the directrix. In oder to make the calculations easier, the apex is shifted to the point of origin and the directrix is parallel to the z-axis, so $\vec{S} = (0, 0, 0)$ and $\vec{w} = (0, 0, 1)$. So equation 4.4 becomes

$$\cos(\theta) = \frac{(\vec{S} - \vec{X}) \cdot \vec{w}}{|\vec{S} - \vec{X}| \cdot |\vec{w}|} \rightarrow \cos(\theta) = \frac{-x_3}{|\vec{X}|} \tag{4.5}$$

$$\Rightarrow x_3^2 = \cot^2(\theta)(x_1^2 + x_2^2). \tag{4.6}$$

The equation for a plane is:

$$n_1 x_1 + n_2 x_2 + n_3 x_3 + n_0 = 0 \tag{4.7}$$

$$\vec{n} = (n_1, n_2, n_3) \tag{4.8}$$

For the sake of convenience and with no loss of generality the plane is rotated so that it is parallel to the y-axis and the start point is $\vec{A} = (0, 0, d)$ and $\vec{n} = (n_1, 0, n_3)$, so that 4.8 becomes

$$n_1 x_1 + n_3 x_3 = n_3 d \tag{4.9}$$

In order to get the intersection equation one can insert 4.6 in 4.9:

$$n_1 x_1 + n_3 \sqrt{\cot(\theta)} \sqrt{(x_1^2 + x_2^2)} - n_3 d = 0 \tag{4.10}$$

$$\Rightarrow x_1^2 \cdot \underbrace{(n_1^2 - n_3^2 \cot(\theta))}_{A} \underbrace{-2 n_1 n_3 d}_{B} \cdot x_1 \underbrace{-n_3^2 \cot(\theta)}_{C} \cdot x_2^2 \underbrace{+n_3^2 d}_{D} = 0 \tag{4.11}$$

$$A x_1^2 + B x_1 + C x_2^2 + D = 0 \tag{4.12}$$

With equation 4.12 it is now possible to calculate the intersection parameter. An ellipse needs five parameters to be unique, so one set of parameters would be the semi-major axis the semi-minor-axis the position of the center and the angle between vertical axis of the coordinate system and the major-axis. Since the plane has been rotated to be parallel to the y-axis, the major-axis lies within the x-z-plane and the minor-axis is parallel to the y-axis. The major-axis can now be calculated by inserting $x_2 = 0$ into equation 4.12:

$$Ax_1^2 + Bx_1 + D = 0 \tag{4.13}$$

$$\Rightarrow x_{1,1} = \frac{-B + \sqrt{B^2 - 4AD}}{2A} \tag{4.14}$$

$$\Rightarrow x_{1,2} = \frac{-B - \sqrt{B^2 - 4AD}}{2A} \tag{4.15}$$

$$a = \frac{(x_{1,1} - x_{1,2})}{2\cos(\beta)} = \frac{\sqrt{B^2 - 4AD}}{2A\cos(\beta)}, \tag{4.16}$$

where a is the value of the semi-major-axis and β is the angle between the plane and the x-axis, so $\beta = \arcsin(n_1)$. The minor-axis is then the distance between the biggest and smallest value of x_2 which still solves the intersection equation. So, equation 4.12 needs then to be solved for x_2, differentiated and solved in order to get the maximum:

$$x_2 = \sqrt{\frac{Ax_1^2 + Bx_1 + D}{-C}} \tag{4.17}$$

$$\frac{dx_2}{dx_1} = \frac{1}{2} \cdot \frac{1}{\sqrt{\frac{Ax_1^2+Bx_1+D}{-C}}} \cdot \frac{2Ax_1 + B}{-C} \stackrel{!}{=} 0 \tag{4.18}$$

$$\Rightarrow 2Ax_0 + B = 0 \tag{4.19}$$

$$\Rightarrow x_0 = \frac{-B}{2A} \tag{4.20}$$

Inserting x_0 in equation 4.18 yields the value of the semi-minor-axis b:

$$b = x_2(x_0) = \sqrt{\frac{-\frac{B}{2} - \frac{B^2}{2A} + D}{-C}} \tag{4.21}$$

The x-value of the center of the ellipse is x_0, the y-value is 0 due to symmetry reasons. Since it is easier to handle an ellipse in two dimensions instead of an ellipse within a inclined plane in three dimensions it is useful to rotate the system in a way that the plane is parallel to the x-y-plane. The only parameter which changes because of this operation is then x_0: $x_0 \rightarrow x_{0,rot} = x_0/\cos(\beta)$.

4.4 Reconstruction of lepton track lengths

Within the following section the steps which are executed for the track length reconstruction of one event are described.
The track length reconstruction basically executes three different steps. First an event selection is used to determine whether the event is suited for a track length reconstruction. The event selection uses two cuts in order to separate events. On the one hand a closer look at the position of the reconstructed vertex is taken. In order to pass the cut, the reconstructed vertex either must be within the instrumented volume, but with a maximal x-value of 36 m or the

reconstructed vertex shifted for 20 m in neutrino beam direction must be within the detector. These conditions seem reasonable, since an event whose vertex is way outside of the instrumented volume does not leave any usable data inside the detector. If the vertex is too close to the right edge of the detector it is very likely that most secondary particles are outside the detector very soon after the interaction, which makes this track length reconstruction impossible.
On the other hand the direction of the reconstructed track is considered. If the angular difference between reconstructed track and neutrino beam direction is greater than 60° the event does not pass the event selection. One reason for this cut is that for leptons with a very shallow angle to the detector planes the reconstruction described in section 4.3 does not work anymore, since the conic section is no longer an ellipse, but a parabola or a hyperbola. The other reason is that events with a big angular difference between neutrino and lepton track have a high B_y, which means that a lot of the available energy is used for the hadronic shower and only a little for the lepton. Therefore the lepton is not able to cause a lot of light, which makes it improbable that the track length reconstruction would yield useful results. An event needs to pass both, the vertex cut and the track cut in order to be selected for the track length reconstruction.
After the event selection a simple hit selection is applied in order to filter hits which can not be connected to the neutrino interaction or which are caused by multiple scattered light. For the hit selection two time residuals are calculated:

$$t_{res}^{vac} = (t_{hit} - t_{reco}) - \left(\frac{d}{c_0}\right) \tag{4.22}$$

$$t_{res}^{water} = (t_{hit} - t_{reco}) - \left(\frac{d}{c_{H_2O}}\right), \tag{4.23}$$

where t_{hit} is the hit time, t_{reco} the reconstructed interaction time, d the distance between PMT position and vertex, c_0 the speed of light in vacuum and c_{H_2O} the speed of light in water. A hit needs to fulfill the condition

$$t_{res}^{vac} > -20\,\text{ns} \tag{4.24}$$

$$\text{and} \quad t_{res}^{water} < 30\,\text{ns} \tag{4.25}$$

to be passed to the track length reconstruction.
Condition 4.24 excludes all hits which can not be causally connected to the interaction since the detection time was earlier than any possible signal could have reached the PMT position. The fact that t_{res}^{vac} can be less than zero is a consequence of the reconstruction errors of interaction vertex and time.
Condition 4.25 excludes all indirect hits, meaning all hits which are caused by scattered photons. As mentioned above scattered light loses a lot of information about the emitting particle since its direction has changed.
After the event and hit selection the actual track length reconstruction starts working. The first step it to determine all detector planes, for which a Cerenkov ring reconstruction is relevant, so all planes which have a bigger x-value than the reconstructed vertex. Theoretically all possible detector planes could be used in order to reconstruct Cerenkov rings, but because of the detector layout

the most useful planes are parallel to the y-z-plane. Thus all planes have a normal vector of $\vec{n} = (1, 0, 0)$ and a start point of $A = (z, 0, 0)$, while z goes from $-48\,\mathrm{m}$ to $+48\,\mathrm{m}$ in steps of $6\,\mathrm{m}$. The reason for the exclusion of all planes left of the vertex is that most secondary particles move approximately in the same direction as the initial particle, due to conservation of momentum, so along the neutrino beam direction.
After the detector planes have been chosen for one plane after another the same steps are applied. First, all hits within a specific plane are determined, and then passed to the Cerenkov ring reconstruction along with the plane parameters, and the reconstructed track and vertex for the event. Before the possible Cerenkov rings within the plane are calculated some geometrical operations are executed in order to use the advantages mentioned in section 4.3 due to symmetry reasons. Therefore hits and vertex are shifted such that the vertex lies within the point of origin. Then the detector plane and all hits are rotated so that the reconstructed track is identical to the z-axis. The next step is then the rotation of hits and plane in order to make it parallel to the y-axis, so that $\vec{n}_{det} \rightarrow \vec{n}_{det,rot} = (n_1, 0, n_3)$. Finally the hits are rotated around the y-axis by angle equal to the inclination of detector plane and x-axis. The last step is necessary to get the new hit position in a two dimensional system, which makes it easier to determine the hits which lie on a Cerenkov ring.
The so processed parameters are then used to calculate Cerenkov rings for various values of the parameter d, which is the distance on the lepton track between emitting point of Cerenkov photons and detector plane (see fig.4.8). So, for each value of d from $0\,\mathrm{m}$ to $80\,\mathrm{m}$ in steps of $0.25\,\mathrm{m}$ a Cerenkov ring is calculated and for each ring the hits are counted, which are crossed by it. To find these hits, the two dimensional space is quantized in squares with an edge length of $0.5\,\mathrm{m}$. If the Cerenkov ring crosses the same pixel a hit lies in, the hit is counted. So, for each distance d a number of hits, which would fit a possible Cerenkov ring and the hit time of each hit is stored. With the value of d and the position of the reconstructed vertex the minimal track length L can be calculated. The Cerenkov ring reconstruction therefore returns an array of hypothetical minimal track lengths L and the amount of hits which would fit such hypotheses for each plane.
In figure 4.10 the results from the track length reconstruction for a electron neutrino premium event is illustrated. The figure contains three different histograms. The top left plot is a normal histogram for the time residuals t_{res}^{water} of the hits, with a bin width of $1\,\mathrm{ns}$ and unlike normal histograms the number of entries for each bin is on the x-axis and the residual bins are on the y-axis. A similar histogram is the on the bottom right position, but for minimal track lengths. The bin width is $1\,\mathrm{m}$, so each count resembles a hit, which matches the respective minimal track length. The two dimensional histogram on the top right is a combination of the two other histograms, where the color code resembles the amount of hits for each bin, the x-axis the minimal track length and the y-axis the time residual. Figure 4.11 shows the results for a muon neutrino premium event track length reconstruction.
If one compares the histograms of the electron and the muon neutrino event some differences can be seen. First, the amount of hits which indicate a track length above $5\,\mathrm{m}$ is higher for the muon event and second the amount of hits with a negative time residual is also higher for the muon event. Hits, which satisfy both criteria, so track length above $5\,\mathrm{m}$ and negative time residual, are also

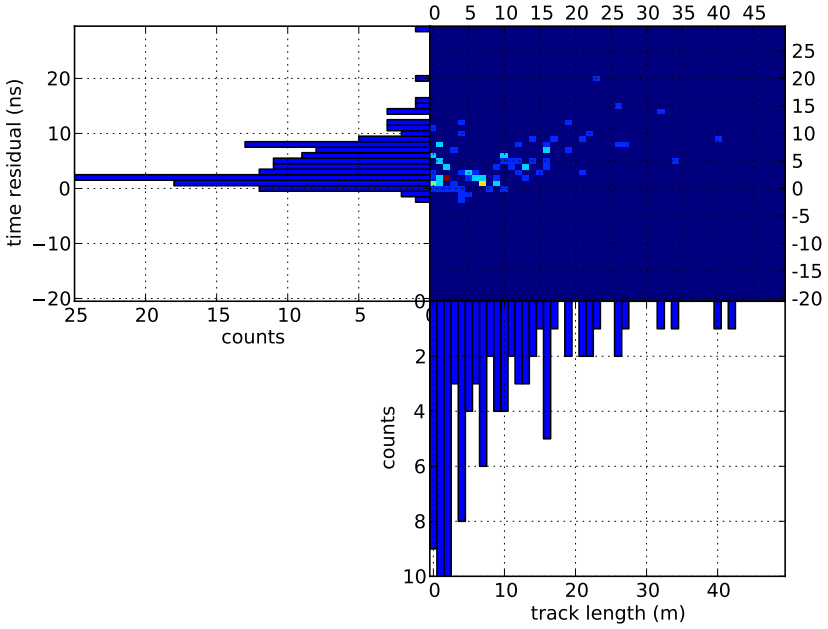

Figure 4.10: Histogram for the results of a track length reconstruction for a ν_e premium event without noise with an neutrino energy of 5 GeV

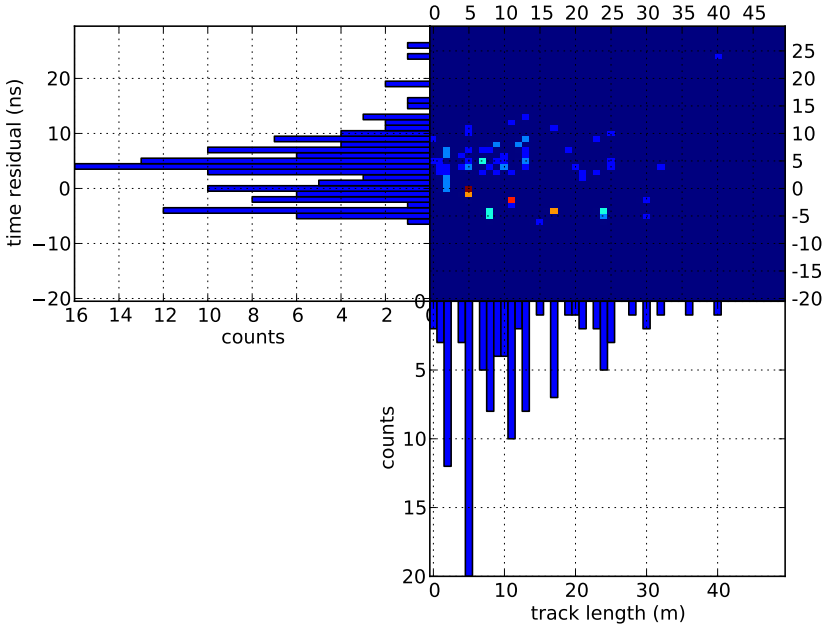

Figure 4.11: Histogram for the results of a track length reconstruction for a ν_μ premium event without noise with a neutrino energy of 5 GeV

more common for the muon neutrino event. The last visible difference would be the distribution of hits for various track lengths. While a clear peak for the electron neutrino event is below a track length of 5 m, distribution for the muon neutrino event seems to be wider and the peak seems to be broader and shifted towards higher distances. These visible differences are used to calculate features for each event which then will be used to make a distinction between muon and electron neutrino events.
It might seem surprising that for the electron neutrino event hits with large track lengths, 20 m and higher are found, but the "large" positive time residuals all these hits have, supports the theory, that these hits are from scattered light and it is coincidental that they are recognized as a hit with the respective track length.

4.5 Algorithm for a distinction using a random decision forest

The next section explains the concept of the classification tool, namely a random decision forest, and what features were used in order to separate between ν_e and ν_μ events.

4.5.1 Random decision forest

One of the simplest classifiers is a single decision tree, like illustrated in figure 4.12.

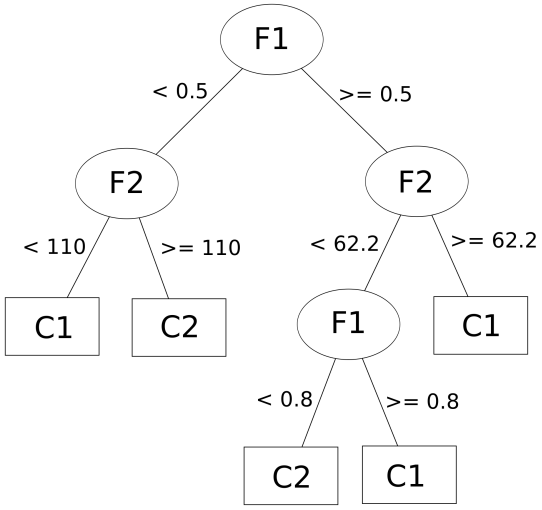

Figure 4.12: Illustration of a decision tree ([16])

The classification of a data set with such a decision tree is very basic. The first step is to define features, $F1, F2, \ldots$ and classes $C1, C2, \ldots$. Now, the features for the data, which shall be classified, have to be calculated. The next step is then to train the classifier, meaning to set the decision rules for each

node (illustrated as ellipses). In figure 4.12 the first node takes feature $F1$ into account. If $F1 < 0.5$ then the classifier follows the left branch, if $F1 \geq 0.5$ the right branch is followed. The next node considers feature $F2$ and so on. The classification ends when a so called leave is reached (represented as a rectangle at the very end of each branch). Each leaf stands for a previously defined class $C1, C2, \ldots$. If such a leave is reached, the data set is then classified to be part of the respective class.
The training of a classifier is done by means of a program. In most cases a so called training data set is defined in order to train the classifier. For this training set, the features have been calculated and the true classes are known. Then an optimization algorithm sets the decision rules, so that the classification rate for the training set is as high as possible.
A further development of a single decision tree is a random decision forest (RDF), which is a classifier composed of a lot of decision trees (that's why it's called a forest). Each decision tree within a RDF only uses a random subsample of the available features. When an event is classified, each decision tree performs a classification using only its subsample of features. The class, which most of the decision trees ended up in, is then the classification results of the RDF.
The biggest advantage of a RDF is its ability to generalize the information from the training data set. The problem with single decision trees is that they tend towards one class, even if the classification rate for the training sets is 100% [19]. Since a RDF is composed of many decision trees the risk of a preference for one specific class is reduced.
The classification tools used for this thesis are written by Stefan Geißelsöder and have been used within the ANTARES project for some years. The program called "train" trains a RDF with a given set of training data and stores the trained RDF. To use this RDF for classification the program "use" is executed on a set of data. The second tool not only classifies a data set, but also yield a classification rate, which is used in order to evaluate the classification process.

4.5.2 Features for the classifier

The key to a classification rate as high as possible are the features used for the classification since they contain the extracted information from the data. The features used for the distinction of ν_e and ν_μ events mostly come from the track length reconstruction algorithm described in section 4.4. Since the track length reconstruction calculates hypothetical minimal track lengths and the amount of hits, which would support respective lengths, the calculated features are derived from these numbers. In table 4.2 all features derived from results from the track length reconstruction are listed. The first feature in this list is the "number of track length hits" which is the sum of hits corresponding to a track length above $-5\,\mathrm{m}$. The consideration of taking hits, which correspond to a negative track length, into account might seem strange, but the fact, that the reconstructed vertex tends to be shifted forward, so within neutrino beam direction, justifies this step. So basically the features are the amount of hits, which support a certain track length, e.g. from -5 to $5\,\mathrm{m}$, from 5 to $10\,\mathrm{m}$ and so on up to above $20\,\mathrm{m}$. For each of these possible track length intervals four features are calculated, the absolute number of hits, the relative number of hits, which is the absolute number divided by the total number of track length hits and for each interval the amount of hits with a negative time residual, absolute and relative,

number of track length hits
absolute number of hits below 5 m
relative number of hits below 5 m
absolute number of hits below 5 m with negative time residual
relative number of hits below 5 m with negative time residual
absolute number of hits above 5 m and below 10 m
relative number of hits above 5 m and below 10 m
absolute number of hits above 5 m and below 10 m with negative time residual
relative number of hits above 5 m and below 10 m with negative time residual
absolute number of hits above 10 m and below 15 m
relative number of hits above 10 m and below 15 m
absolute number of hits above 10 m and below 15 m with negative time residual
relative number of hits above 10 m and below 15 m with negative time residual
absolute number of hits above 15 m and below 20 m
relative number of hits above 15 m and below 20 m
absolute number of hits above 15 m and below 20 m with negative time residual
relative number of hits above 15 m and below 20 m with negative time residual
absolute number of hits above 20 m
relative number of hits above 20 m
absolute number of hits above 20 m with negative time residual
relative number of hits above 20 m with negative time residual

Table 4.2: list of features from the track length reconstruction

are calculated as well.
The time residual which is mentioned here is t_{res}^{water} from formula 4.23. Using the amount of hits with a negative time residual as a feature is promising, since only Cerenkov photons are able to cause such hits, assuming a perfect vertex and time reconstruction result. This is due to the fact, that the emitting particles propagate faster than photons through water. Thus a photon which is emitted by the lepton is able to cause a hit sooner then a photon, which is emitted at the interaction vertex and detected at the same PMT.
Apart from the features listed in table 4.2 four additional features are used. The additional features are listed in table 4.3. The number of shower hits refers to the amount of hits with t_{res}^{water} greater than $-20\,\text{ns}$ but less then 30 ns. So all hits, which satisfy this criterion, might be caused by a electromagnetic or hadronic shower at the vertex. The lower and upper limit take the uncertainties of vertex and time reconstruction into account. The number of hit OMs, refers to all optical modules which detected a hit for an event. Each OM is counted only once, no matter how many PMTs detected hits. The number of selected hits refers to the amount of hits which pass the hit selection described in section 4.4. Both features (number of hit OMs and number of selected hits) should provide a rough energy approximation. This seems necessary since the energy range for beam neutrinos reaches from 2 GeV to 10 GeV and the signature of a neutrino event is strongly connected to the initial neutrino energy.
The last additional feature is the angular difference between the reconstructed track direction and the neutrino beam direction. This features is meant to be a rough estimation of the value of B_y, so the ratio of energy used for the hadronic

number of shower hits
number of hit OMs
number of selected hits
angular difference of reconstructed track and beam direction

Table 4.3: list of additional features used for the ν_e,ν_μ- distinction

shower. For higher values of B_y less energy is available for the lepton, thus the possible track length is reduced and less Cerenkov photons can be emitted, which has a direct effect on the significance of the features from the track length reconstruction.
For each event which passes the event selection these features are calculated and passed to a RDF in order to decide whether it is a ν_e or a ν_μ event.

Chapter 5

Results

The main part of the following chapter is the efficiency analysis of the classifier, which was used for the distinction of ν_e and ν_μ events. In order to enable a more detailed understanding of the presented classification rates, particularly concerning the statistical reliability, the efficiency of the used event selection is discussed, which yields the amount of events for the processed event samples and energy ranges. Furthermore, a closer look is taken on the errors of the vertex, track and time reconstruction, since the developed track length algorithm makes use of these values. The following chapter presents and describes all obtained results. A detailed discussion and interpretation of these results can be found in chapter 6. The terms premium and normal events refer to the in section 4.2 defined event samples.

5.1 Event selection efficiency

The event selection is used in order to determine whether an event is suited for the track length reconstruction or not (see section 4.4). In table 5.1 the amount of events for each sample and energy range is listed. Additionally the efficiency for each event sample averaged over all energy bins is listed within the last column (abbreviation eff.).
For premium events the efficiency is about 90 %, nearly independent of noise and almost equal for ν_e and ν_μ events.
The selection efficiency for normal events drops to about 20 %, but seems to be very stable against noise effects and also nearly independent from the neutrino flavour.
In figure 5.1 the selection efficiency is plotted for each energy range and event sample. Two effects can be seen in the graph, first that the selection efficiency increases with the neutrino energy for both flavors and all event samples. The second effect is that the difference between events with noise and without noise is more distinct for premium events with low neutrino energy. For two energy ranges the selection efficiency for muon neutrino premium events is higher for events with noise, than without. This is the case for a neutrino energy of 7 GeV and much less clearly for 10 GeV. This is assumed to be caused by statistical effects and not due to physical or numerical reasons.

mean energy [GeV]	2	3	4	5	6	7	8	9	10	eff.
ν_e PEnN	861	967	1014	922	1081	1016	1015	1117	1137	0.89
ν_μ PEnN	852	939	954	1020	1038	990	1019	1085	958	0.88
ν_e PEwN	750	895	973	901	1059	996	997	1108	1109	0.87
ν_μ PEwN	778	897	913	990	1015	991	1007	1077	950	0.88
ν_e NEnN	1194	1323	1455	1408	1470	1531	1492	1509	1507	0.20
ν_μ NEnN	1192	1409	1444	1454	1526	1611	1637	1594	1574	0.21
ν_e NEwN	972	1128	1326	1307	1382	1404	1409	1443	1449	0.20
ν_μ NEwN	959	1175	1302	1328	1402	1447	1523	1508	1476	0.20

Table 5.1: Number of events for each energy range and event sample type after the event selection. PE stands for premium event, NE for normal events, nN for no noise and wN for with noise. The last column contains the efficiency for the whole sample.

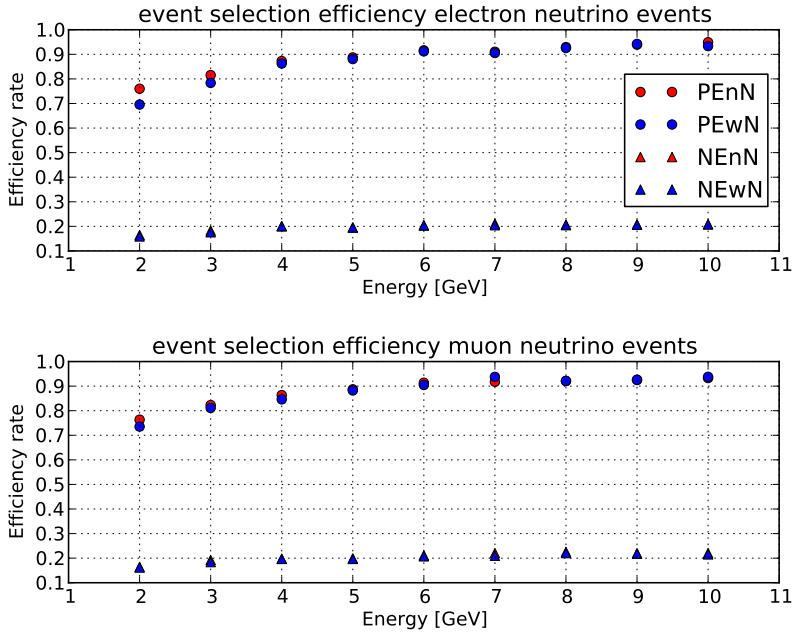

Figure 5.1: Graph of the event selection efficiency. Circles represent premium events, triangles normal events, red stands for events without noise and blue for events with noise. The top graph is for electron neutrino events and the bottom graph for muon neutrino events.

The effective volume for ν_μ and ν_e normal events with noise is plotted in figure 5.2. The dashed red line marks the instrumented volume of the cuboid layout and the green and blue solid lines are fits for the respective events. As functions for the fit $f(x) = (1 - e^{-ax}) \cdot b \cdot V_{gen}$ was used, where a and b are the fitting parameters and V_{gen} is the possible volume for vertices for normal events ($V_{gen} \approx 8.2\,\mathrm{Mm}^3$). The best fit results yield $a_{\nu_e} = 0.708$, $b_{\nu_e} = 0.207$, $a_{\nu_\mu} = 0.660$ and $b_{\nu_\mu} = 0.214$, so both fits converge approximately towards the instrumented volume ($V_{inst} = 1.7\,\mathrm{Mm}^3 = 0.21 \cdot V_{gen}$). The error bars for the effective volume represent the statistical error assuming a binomial distribution of the number of selected events for each energy bin. Since the event selection depends not on one but several variables (like position of vertex, B_y, etc.), which are also randomly distributed, the accurate statistical error is probably larger.

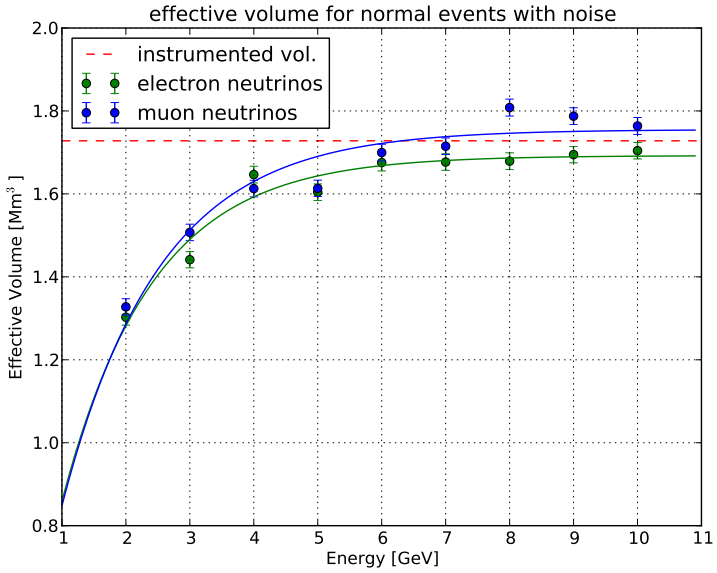

Figure 5.2: Effective volume for normal events with noise with fit.

The distribution of the angular difference between neutrino beam direction and lepton is plotted in figure 5.3 for ν_μ and ν_e CC events after the event selection. The dot marks the median, upper and lower error bar stand for 85 % and 15 % quantile. A clearly visible energy dependency towards smaller differences with higher neutrino energies is visible for both event types. For energies below 7 GeV ν_e events tend towards a larger kinematic angles than ν_μ events, though the effect is not very distinct.

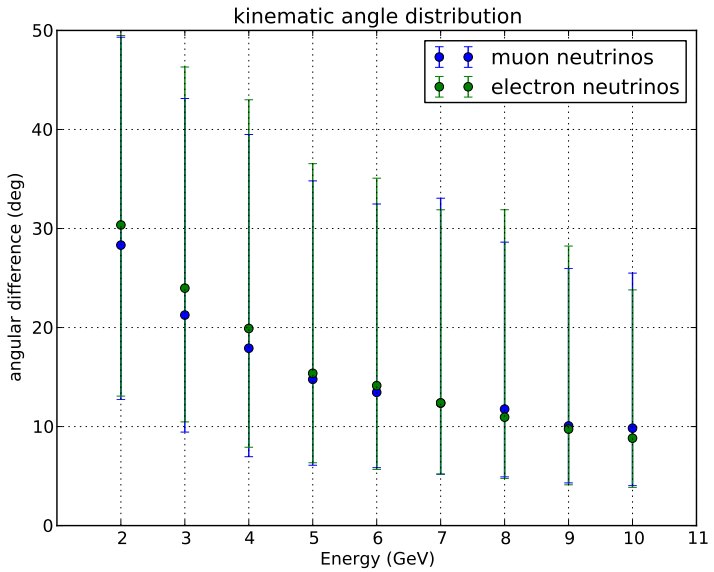

Figure 5.3: Distribution of the angular difference between lepton direction and neutrino beam direction for ν_μ CC and ν_e CC events after the event selection.

5.2 Analysis of vertex, track and time reconstruction

Two reconstruction algorithms were used in order to get reconstructed values for vertex, track and time. The program used for the vertex reconstruction is called "DusjOrcaVertexTresFit", which is the adaption of the "DusjVertexTresFit" algorithm from Florian Folger for the ORCA project. The adaption was carried out by Jannik Hofestädt ([23]). This reconstruction tool returns not only a reconstructed vertex, but also a reconstructed interaction time. The track reconstruction was performed with the "filteringFit" algorithm ([24]).
Since reconstructed values for lepton direction, interaction vertex and time were used for the track length reconstruction it makes sense to investigate the quality of the reconstructed values. This was done for each data sample, for all events before and after the event selection. Since the classification was carried out only for events which passed the event selection the error analysis for the reconstruction algorithms for events before the event selection is moved to the appendix of this thesis (see appendix A).

5.2.1 Analysis of reconstructed interaction vertices

From figure 5.4 to figure 5.11 the vertex errors for each data sample, with and without noise for selected ν_e and ν_μ events are shown. The red dots represent the median, the upper and lower error bar mark the 85 % quantile and the 15 % quantile. The error value is the distance in meter between reconstructed vertex and the true vertex of the interaction.
In figure 5.4 the vertex errors for selected ν_e events without noise and in figure 5.5 with noise are shown. The distance between reconstructed vertex and true vertex increases with the initial neutrino energy. The effect of noise for the vertex reconstruction for this event sample is quite small, but significantly increasing the error. Median, 85 % and 15 % quantile are shifted towards higher errors when the sample contains noise. The conspicuous high median for a neutrino energy of 4 GeV in figure 5.5 is probably due to a statistical fluctuation.
Figures 5.6 and 5.7 show the vertex reconstruction errors for selected ν_μ premium events, respectively with and without noise. It can easily be seen that the vertex errors are higher for ν_μ events compared to ν_e events. While the difference between 85 % quantile and 15 % quantile for selected ν_e premium events does not exceed 1.4 m, the same difference is as large as 9 to 10 m for selected ν_μ premium events. The energy dependence of the vertex error for median and 15 % quantile is still present for ν_μ events and is approximately within the same order of magnitude as for ν_e events. The 85 % quantile, however, increases much steeper for ν_μ events with increasing energy. One interesting phenomenon is that the 85 % quantile is lower for selected ν_μ premium events with noise than for the same events without noise. Median and 15 % quantile position do not seem to be affected much by noise.
Errors for the reconstructed vertex for selected normal ν_e events are plotted in figure 5.8 with noise and in figure 5.9 without noise. Compared to premium events only small differences are visible. An energy dependency between vertex error and neutrino energy is still present. The biggest difference between

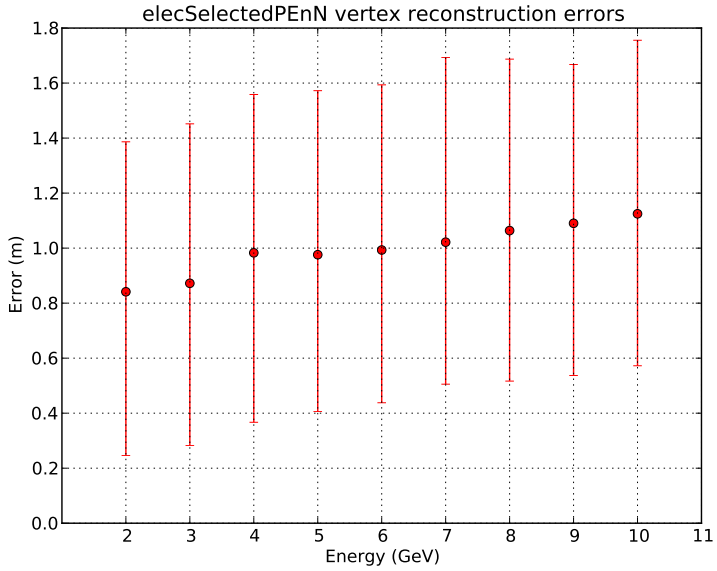

Figure 5.4: Errors of the reconstructed vertex for selected ν_e premium events without noise. The red dot is the median, the top error bar marks the 85 % quantile and the bottom error bar marks the 15 % quantile.

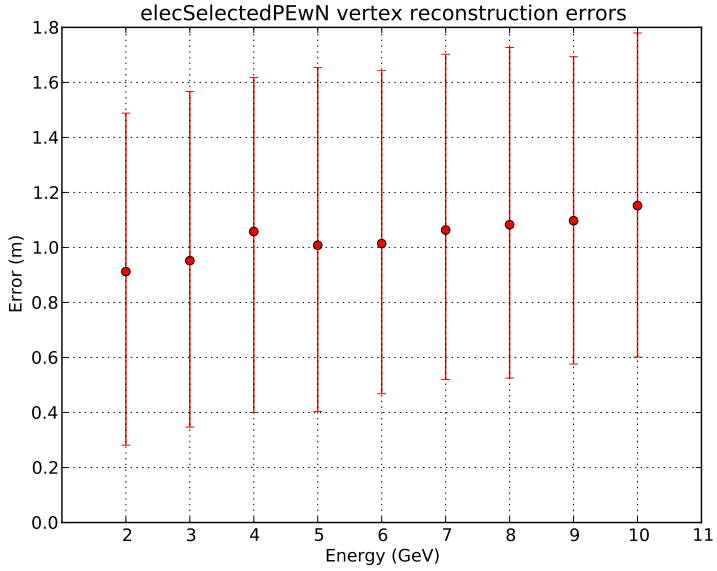

Figure 5.5: Errors of the reconstructed vertex for selected ν_e premium events with noise. The red dot is the median, the top error bar marks the 85 % quantile and the bottom error bar marks the 15 % quantile.

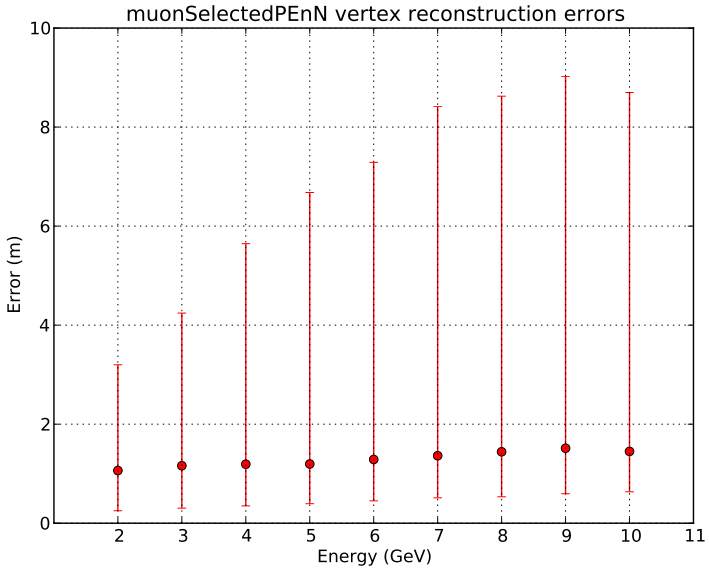

Figure 5.6: Errors of the reconstructed vertex for selected ν_μ premium events without noise. The red dot is the median, the top error bar marks the 85 % quantile and the bottom error bar marks the 15 % quantile.

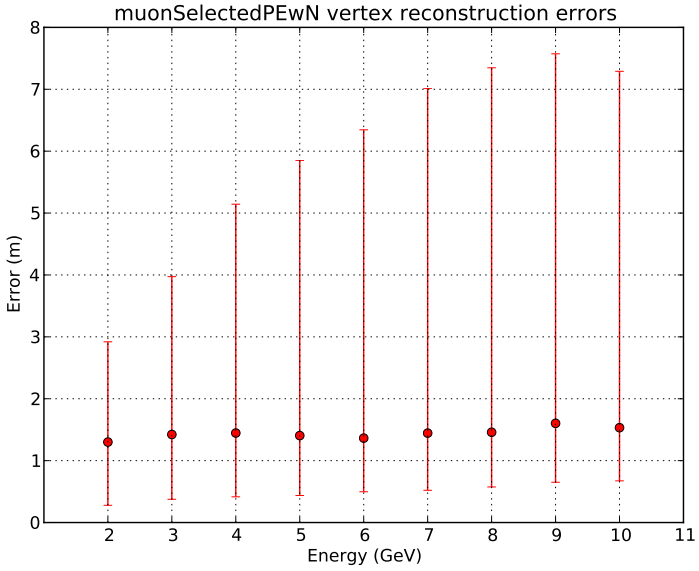

Figure 5.7: Errors of the reconstructed vertex for selected ν_μ premium events with noise. The red dot is the median, the top error bar marks the 85 % quantile and the bottom error bar marks the 15 % quantile.

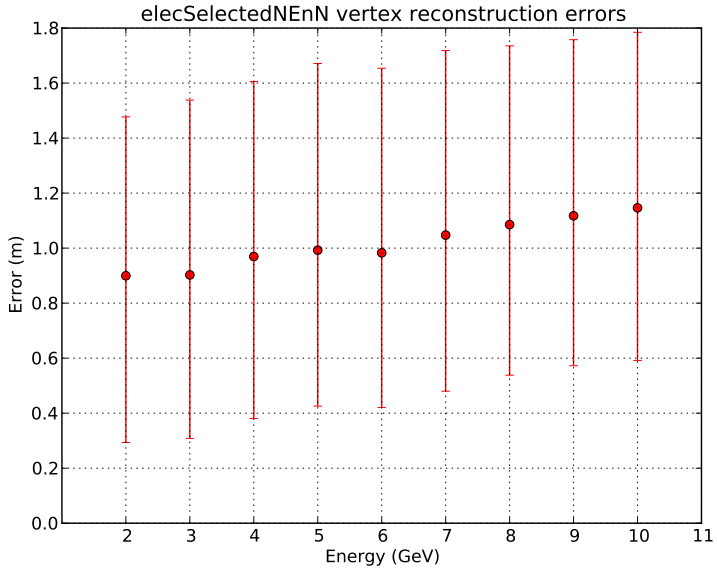

Figure 5.8: Errors of the reconstructed vertex for selected ν_e normal events without noise. The red dot is the median, the top error bar marks the 85 % quantile and the bottom error bar marks the 15 % quantile.

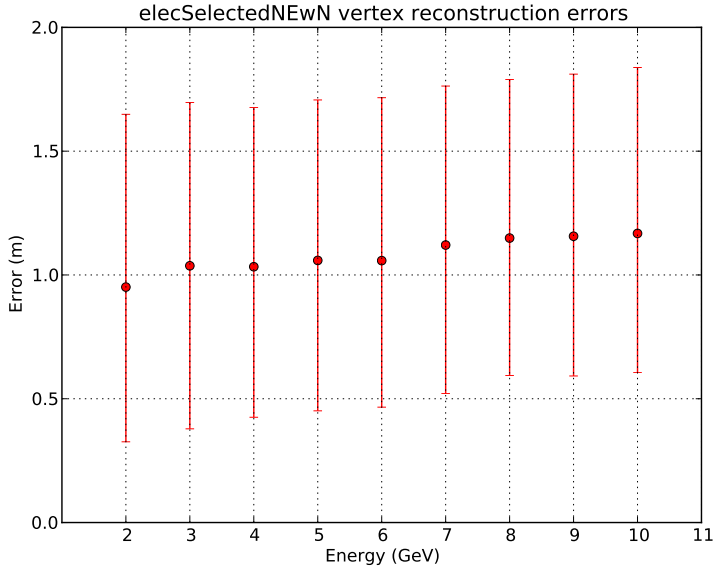

Figure 5.9: Errors of the reconstructed vertex for selected ν_e normal events with noise. The red dot is the median, the top error bar marks the 85 % quantile and the bottom error bar marks the 15 % quantile.

premium and normal events is seen for energy ranges 2 and 3 GeV. For both energy ranges median, 15 % and 85 % quantile are shifted towards higher errors, although the effect is very small. The difference between premium and normal events for this event sample is less than 0.1 m for all probed energy ranges. If noise is added to the events the vertex errors increase slightly. The effect of noise becomes less distinct for higher neutrino energies, similar to premium events, and is less than 0.2 m for all energy ranges.

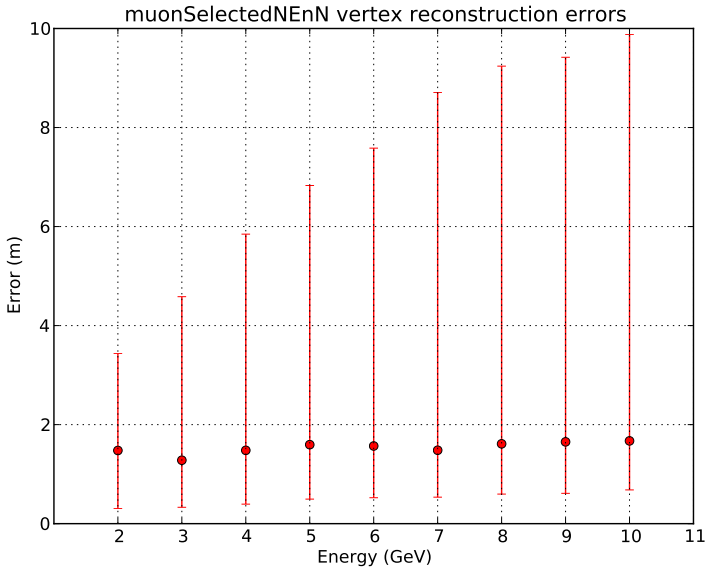

Figure 5.10: Errors of the reconstructed vertex for selected ν_μ normal events without noise. The red dot is the median, the top error bar marks the 85 % quantile and the bottom error bar marks the 15 % quantile.

Similar to ν_e events, the vertex reconstruction becomes a little bit worse for normal events compared to premium events for ν_μ. In figure 5.10 selected ν_μ normal events without noise and in figure 5.11 with noise are shown. The difference between premium and normal events is less than 0.5 m for all energies and becomes less distinct for higher neutrino energies. An energy dependency of the 85 % quantile is still clearly visible, for the 15 % quantile this effect is also still present, although not as steep. The median seems to underlie some fluctuations, the energy dependency, however, is still present. This fluctuation is much more distinct for events with noise. The energy dependency for the median seems to have vanished, but is still visible for the 15 % and the 85 % quantile. The effect, that the 85 % quantile is lower for events with noise than for events without noise is also present for selected ν_μ normal events.

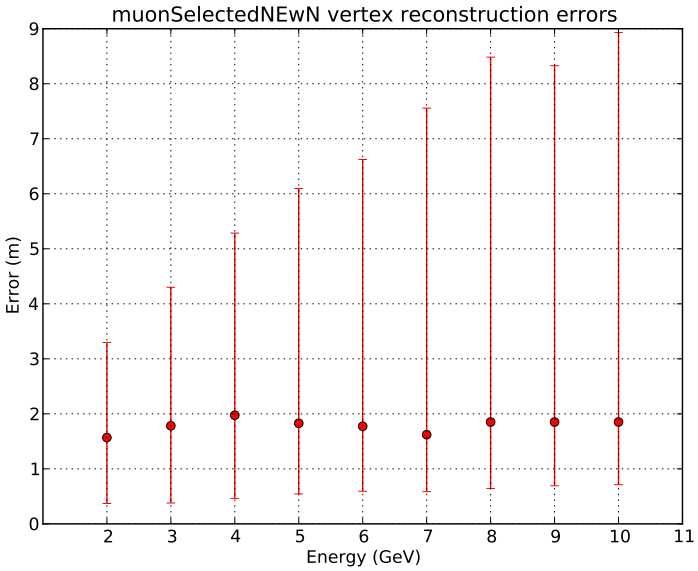

Figure 5.11: Errors of the reconstructed vertex for selected ν_μ normal events with noise. The red dot is the median, the top error bar marks the 85 % quantile and the bottom error bar marks the 15 % quantile.

5.2.2 Analysis of the reconstructed lepton directions

Figure 5.12 shows the angular difference between reconstructed track and true lepton direction for selected ν_e premium events without noise. The angular error for the same sample with noise is shown in figure 5.13. In both figures an energy dependency can be seen. For higher neutrino energies the median decreases down to approximately 5°. A significant difference can be seen for the 85 % quantile, which is clearly higher for events which noise, but drops to about 20° with increasing energy. For ν_e premium events the 85 % quantile also drops with increasing energy, but not as steep as for the same sample with noise and with a more distinct fluctuation. The 15 % quantile is almost identical for events with noise and without noise.

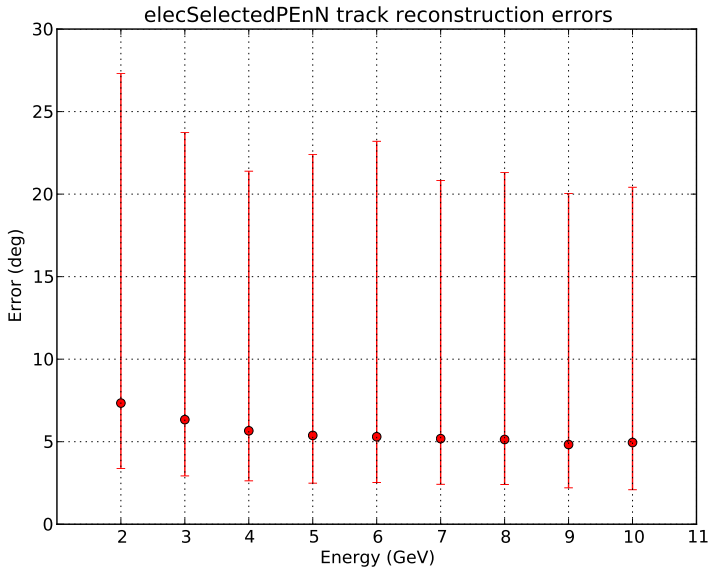

Figure 5.12: Errors of the reconstructed lepton direction for selected ν_e premium events without noise. The red dot is the median, the top error bar marks the 85 % quantile and the bottom error bar marks the 15 % quantile.

In figure 5.14 the track reconstruction errors for selected ν_μ premium events without noise and in figure 5.15 the same events with noise are illustrated. Compared to ν_e premium events the track reconstruction errors are much smaller for the sample with noise and without noise. The 85 % quantile for events without noise shows a energy dependency as well and drops to clearly below 10° although large statistical fluctuations seem to be present. The biggest difference between events with and without noise is visible for a neutrino energy of 2 GeV. The median is almost twice as high when noise is present. The 85 % quantile reaches almost 60° but drops with increasing energy also to below 10°. For both samples, selected ν_μ premium events with and without noise, the median seems to converge to a value below 2°.
The track reconstruction errors for selected ν_e normal events without noise are

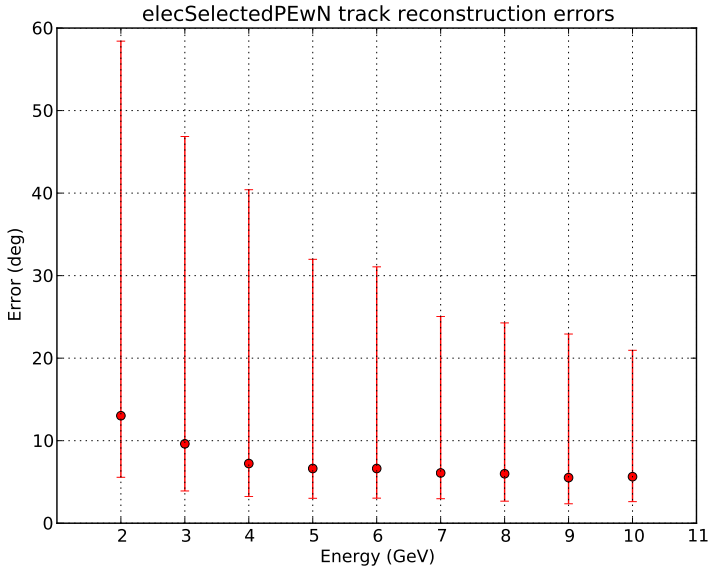

Figure 5.13: Errors of the reconstructed lepton direction for selected ν_e premium events with noise. The red dot is the median, the top error bar marks the 85 % quantile and the bottom error bar marks the 15 % quantile.

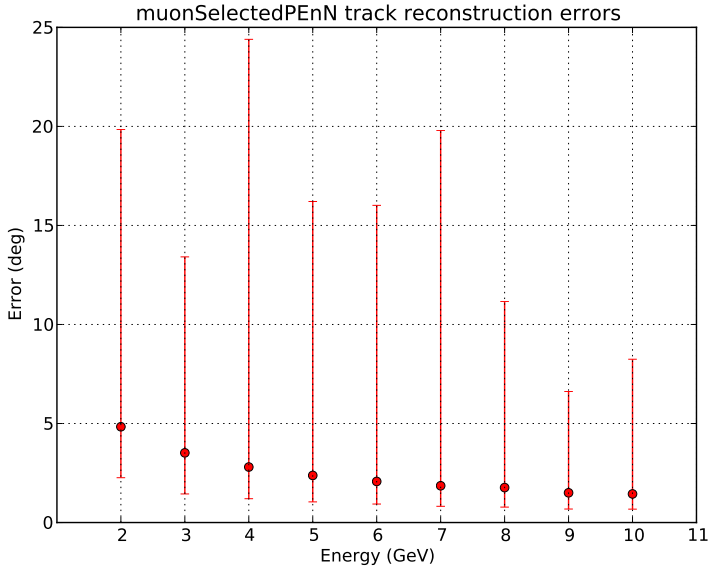

Figure 5.14: Errors of the reconstructed lepton direction for selected ν_μ premium events without noise. The red dot is the median, the top error bar marks the 85 % quantile and the bottom error bar marks the 15 % quantile.

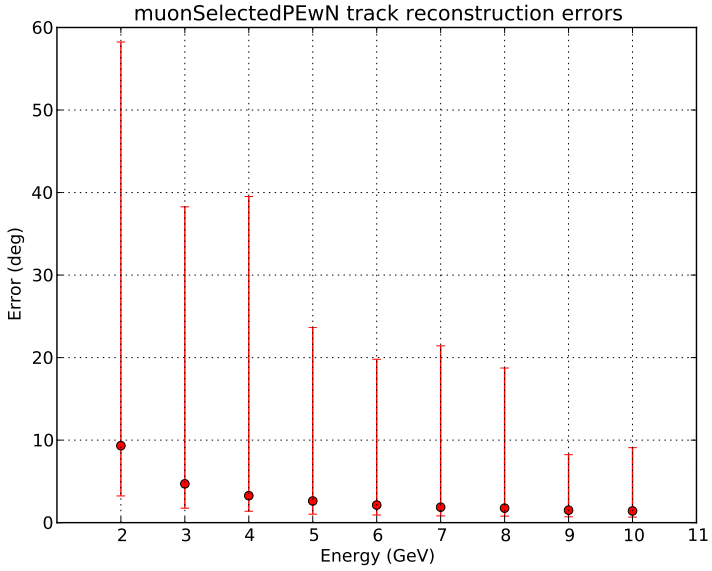

Figure 5.15: Errors of the reconstructed lepton direction for selected ν_μ premium events with noise. The red dot is the median, the top error bar marks the 85 % quantile and the bottom error bar marks the 15 % quantile.

plotted in figure 5.16 and with noise in figure 5.17. The energy dependency is still clearly visible for median and both quantiles. With increasing energy the track reconstruction error decreases and the median seems to converge to a value of approximately 6°. The remarkable low value for an energy of 2 GeV in figure 5.16 is assumed to be a statistical effect. Track errors increase when noise is present within the events, but the low energy range is much more affected then high energies. The median still converges to about 7°, but the 85 % quantile is much higher for events with noise. For selected ν_e normal events the track error for 2 GeV with noise suites the rest of the values much more, which also leads to the assumption that the 2 GeV track error for selected ν_e normal events without noise is a statistical effect.
Figures 5.18 and 5.19 show the reconstructed track errors for selected normal ν_μ events with and without noise. Similar to ν_μ premium events an energy dependency towards smaller errors with increasing neutrino energy is present. The medians for both samples still converge to errors as low as 2°, but the medians for events with noise in the low energy range are much higher. The 85 % quantiles for events with and without noise also show a clear energy dependency. While for events without noise it drops to below 10° it remains above 15° for events with noise.

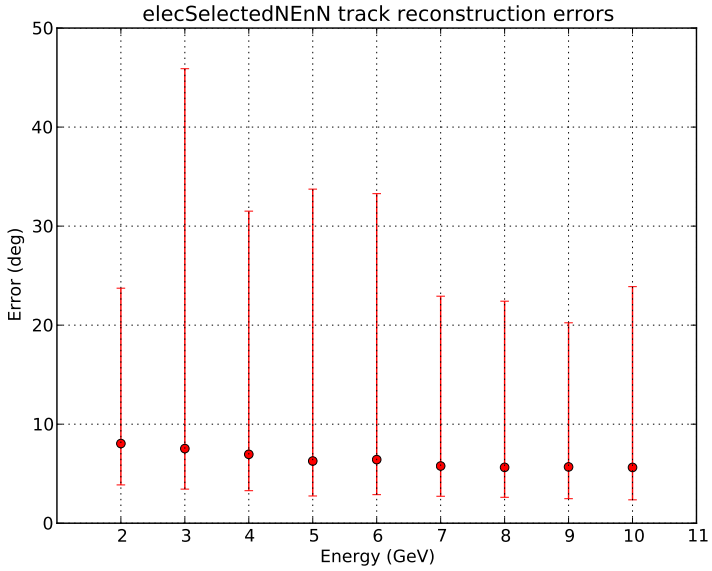

Figure 5.16: Errors of the reconstructed lepton direction for selected ν_e normal events without noise. The red dot is the median, the top error bar marks the 85 % quantile and the bottom error bar marks the 15 % quantile.

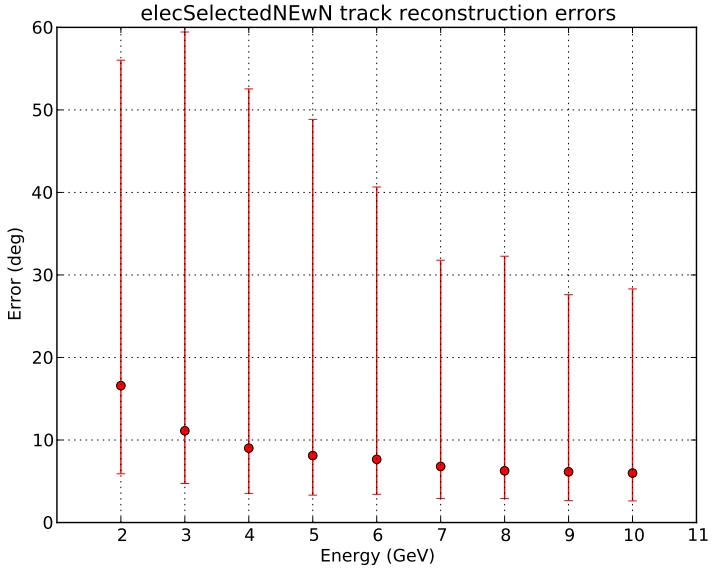

Figure 5.17: Errors of the reconstructed lepton direction for selected ν_e normal events with noise. The red dot is the median, the top error bar marks the 85 % quantile and the bottom error bar marks the 15 % quantile.

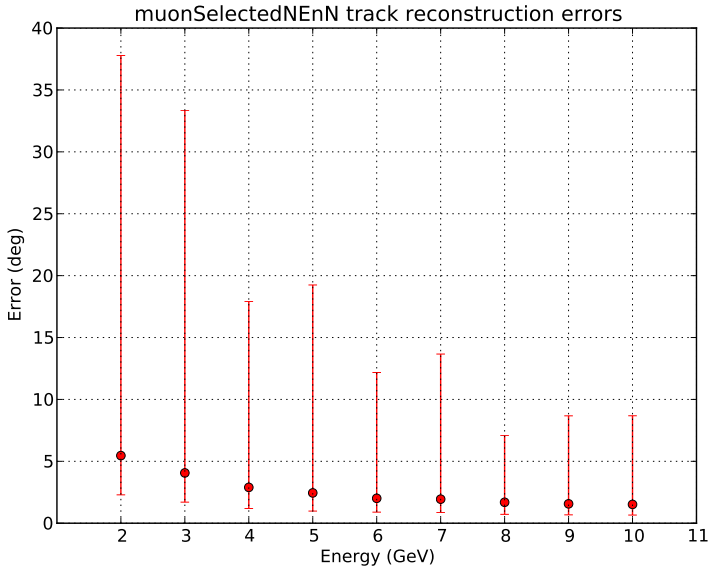

Figure 5.18: Errors of the reconstructed lepton direction for selected ν_μ normal events without noise. The red dot is the median, the top error bar marks the 85 % quantile and the bottom error bar marks the 15 % quantile.

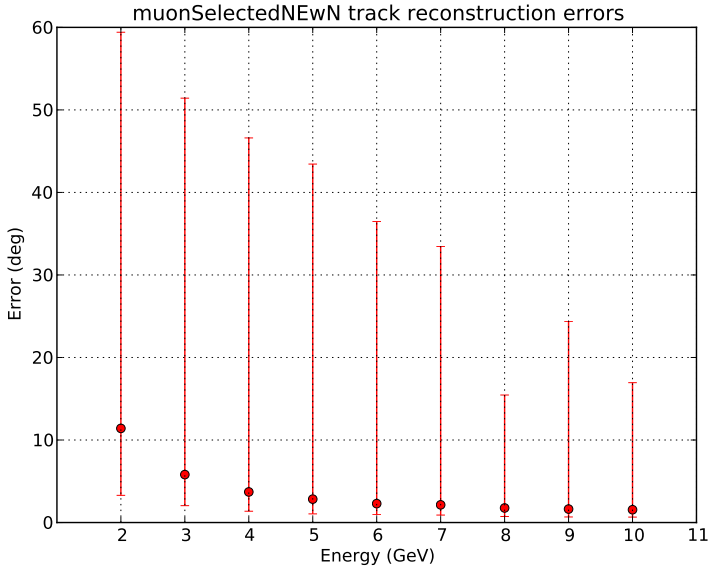

Figure 5.19: Errors of the reconstructed lepton direction for selected ν_μ normal events with noise. The red dot is the median, the top error bar marks the 85 % quantile and the bottom error bar marks the 15 % quantile.

5.2.3 Analysis of the reconstructed interaction time

The errors of the reconstructed interaction time, discussed in this section, is the only error for which the sign is important. The reconstructed interaction time might be too late (positive error) or too early (negative error).
In figure 5.20 the errors of the reconstructed interaction time for selected ν_e premium events without noise and in figure 5.21 with noise are shown. Similar to the error of the reconstructed vertex a dependency between neutrino energy and time difference can be seen for both samples, so with noise and without noise. Higher neutrino energies cause larger positive errors for the reconstructed interaction time. There is almost no visible difference between ν_e premium events with and without noise, but the time errors seem to tend towards larger positive errors for events with noise, although the difference is less than 0.5 ns for each probed energy range. The interaction time error looks very similar to the vertex error (shown in figures 5.4 and 5.5). This also applies for the noticeable high error for a neutrino energy of 4 GeV.

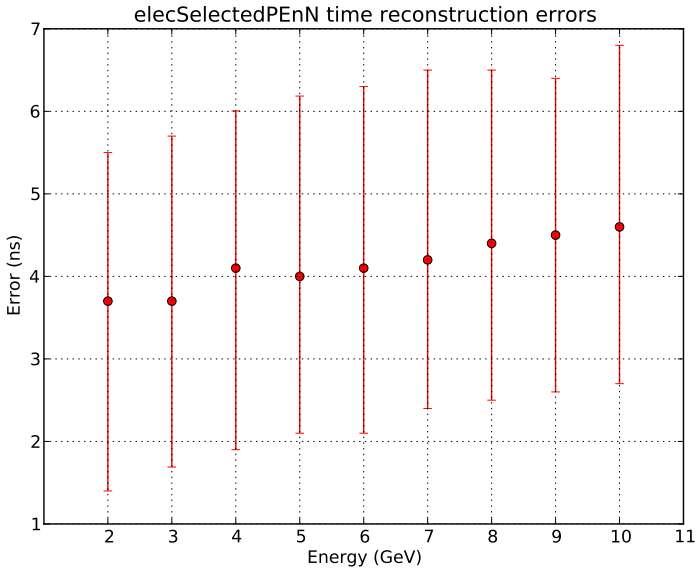

Figure 5.20: Errors of the reconstructed interaction time for selected ν_e premium events without noise. The red dot is the median, the top error bar marks the 85 % quantile and the bottom error bar marks the 15 % quantile.

The errors of the reconstructed interaction time for selected ν_μ premium events without noise are plotted in figure 5.22 and with noise in figure 5.23. An energy dependency for the median and the 15 % quantile is still present, although not as distinct as for ν_e events. A clearly visible energy dependency for the 85 % quantile is present. For both event samples, so with and without noise, a higher neutrino energy leads to larger positive interaction time errors. Similar to ν_e premium events a high resemblance between vertex errors and interaction time errors is present for ν_μ premium events. This is also true for the phenomenon

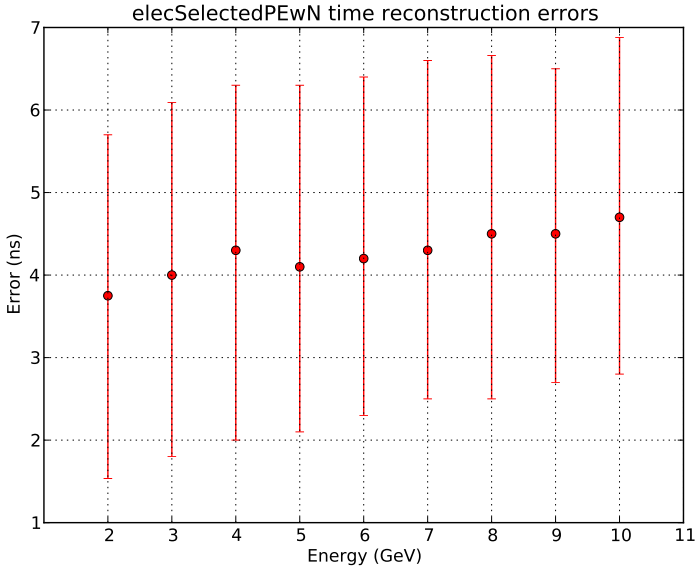

Figure 5.21: Errors of the reconstructed interaction time for selected ν_e premium events with noise. The red dot is the median, the top error bar marks the 85 % quantile and the bottom error bar marks the 15 % quantile.

that the 85 % quantile is lower for events with noise than for events without noise. The effect of noise, however, on median and 15 % quantile is less than 2 ns.
Figures 5.24 and 5.25 display the reconstructed interaction time error for selected ν_e normal events, respectively with and without noise. Nearly no visible difference between ν_e premium and normal events is visible. The energy dependence is still present for median and both quantiles. The runaway at 4 GeV has vanished for normal events, but the median at 3 GeV in for normal events with noise seems to fluctuate a little.
Errors for reconstructed selected ν_μ normal events with and without noise are plotted in figures 5.26 and 5.27. The difference between premium events and normal events is still very small, but more distinct than for ν_e events. Median and 85 % quantile is shifted towards larger positive errors, medians less than 2 ns and 85 % quantiles less than 5 ns. Noise increases the medians further, although for not more than 3 ns. The effect that 85 % quantiles have lower values for normal events with noise than for normal events without noise is present for this sample as well.

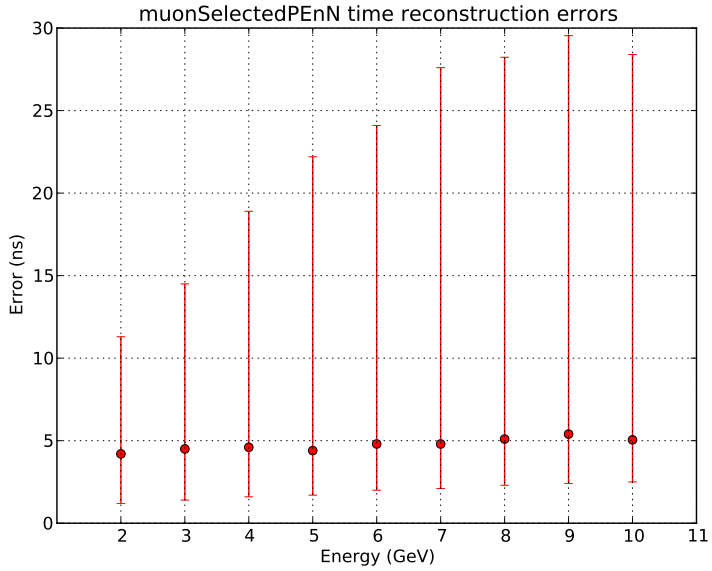

Figure 5.22: Errors of the reconstructed interaction time for selected ν_μ premium events without noise. The red dot is the median, the top error bar marks the 85 % quantile and the bottom error bar marks the 15 % quantile.

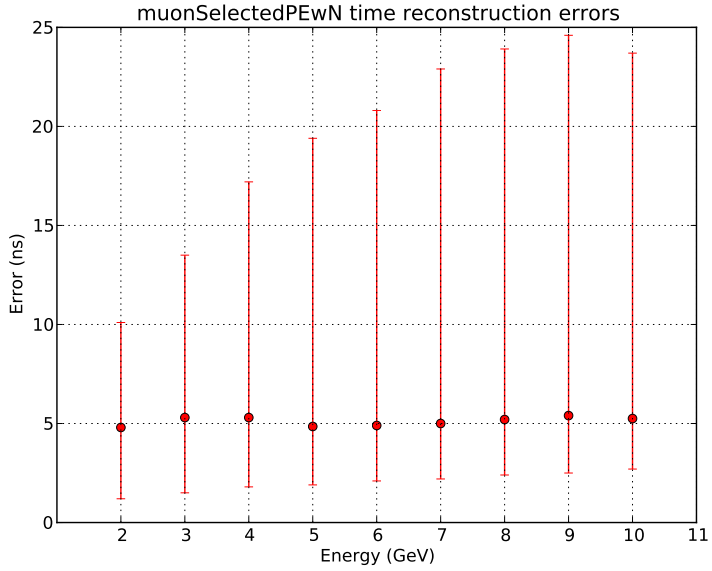

Figure 5.23: Errors of the reconstructed interaction time for selected ν_μ premium events with noise. The red dot is the median, the top error bar marks the 85 % quantile and the bottom error bar marks the 15 % quantile.

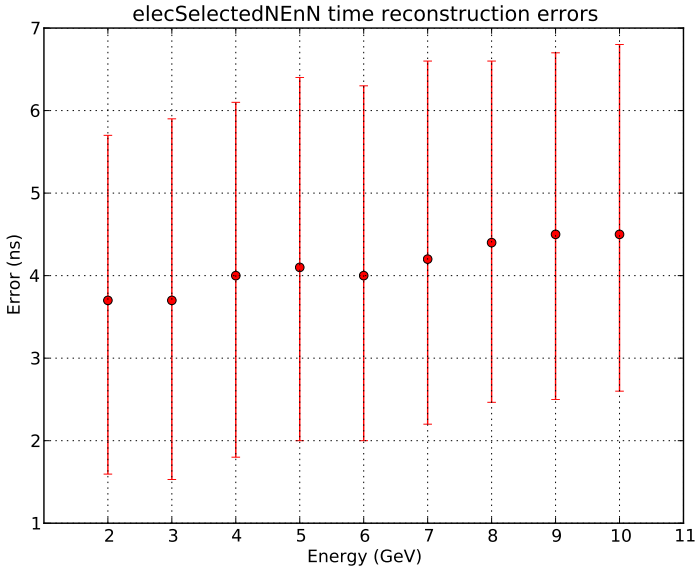

Figure 5.24: Errors of the reconstructed interaction time for selected ν_e normal events without noise. The red dot is the median, the top error bar marks the 85 % quantile and the bottom error bar marks the 15 % quantile.

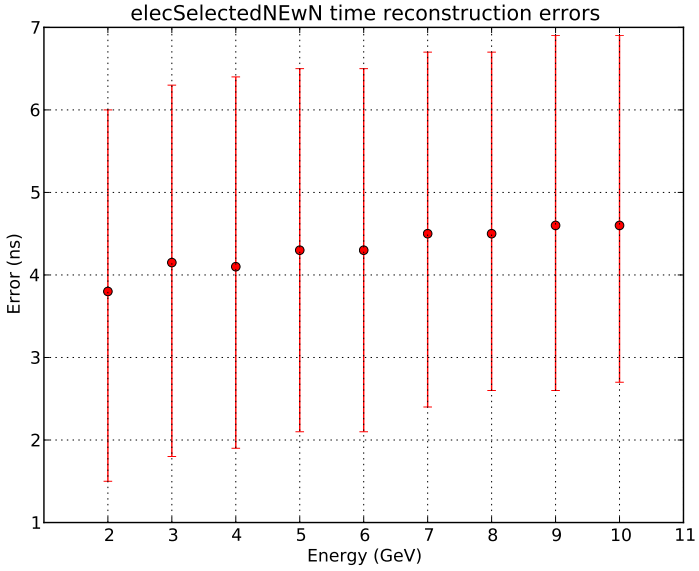

Figure 5.25: Errors of the reconstructed interaction time for selected ν_e normal events with noise. The red dot is the median, the top error bar marks the 85 % quantile and the bottom error bar marks the 15 % quantile.

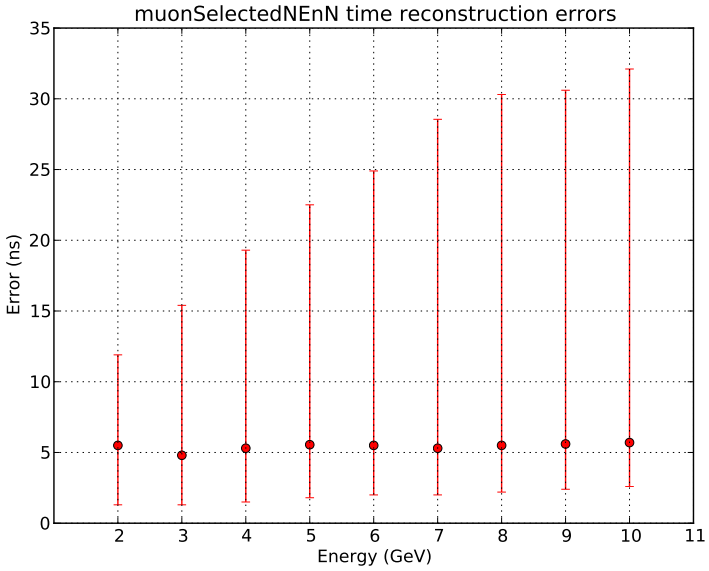

Figure 5.26: Errors of the reconstructed interaction time for selected ν_μ normal events without noise. The red dot is the median, the top error bar marks the 85 % quantile and the bottom error bar marks the 15 % quantile.

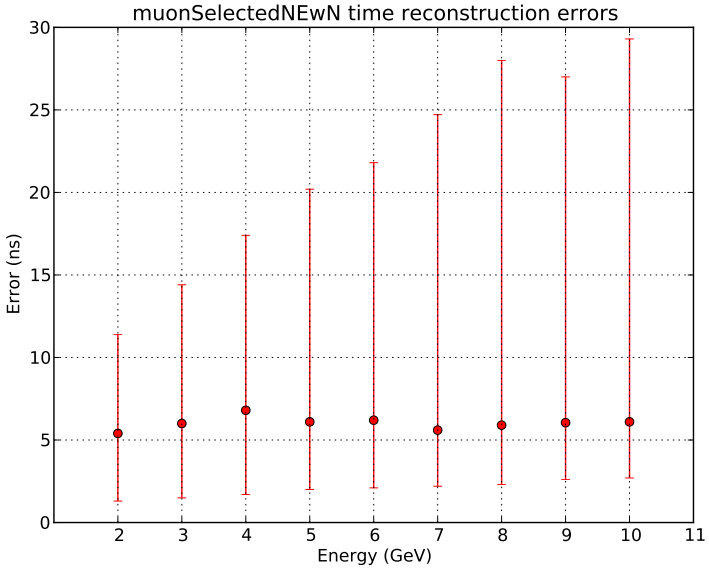

Figure 5.27: Errors of the reconstructed interaction time for selected ν_μ normal events with noise. The red dot is the median, the top error bar marks the 85 % quantile and the bottom error bar marks the 15 % quantile.

5.3 Classification efficiency

In the following section the classification results are presented. In order to get results as significant as possible a cross validation was used to calculate the classification results for each energy range and data sample. The way this process was performed shall be briefly explained before the actual results are shown.
The cross validation is a common procedure for the efficiency analysis of a classifier. The first step is to divide the data sample into a number of equally large subsamples. If, for example, the initial data sample contains 500 events and one would use ten subsamples, each subsample would contain 50 events. The overlap between the subsamples is zero. Then the data from all but one subsample, which is also called the training set, is used to train the classifier, and the data form the remaining subsamples, called the test set, is used to test the classifier. This leads to the classification rate for the first subsample. Then the next subsample is excluded, the rest used to train the classifier again and then the excluded sample is used to test the newly trained classifier, which leads to the classification rate for the second subsample. This procedure is then repeated until each subsample has been used as test set once. In order to continue the example from above, ten classification rates, one for each subsample, would have been obtained at this point. With the so obtained classification rates a mean classification rate, standard deviation etc. can be calculated. The reason for applying the cross validation to analyze the performance of a classifier is to the get more significant results. Since the number of events which are available to test a classifier is limited, the cross validation reduces the effect of statistical fluctuations, because not only one rate is calculated to characterize the performance, but more values for the classification rate are available. Another advantage of the cross validation is the fact that every subsample is used as test sample once, meaning that every event of the available data was classified once, leading to more statistical reliability and a more efficient usage of the available number of events.
In order to get an energy dependent classification rate this method had to be adjusted a little. The events available for each energy range were divided into the same number of equally large subsamples. Then from each class one subsample was excluded as test sample and the all other subsamples (from all energy ranges) were used as training samples. The trained classifier was then tested with the remaining subsample from each energy range. This leads to a classification result for each energy range. This procedure was then repeated, until each subsample has been used as test sample once. The classification rates for each class were then used to calculate the median and the 85 % and the 15 % quantile for each energy range. For this thesis the events from each energy range were divided in 10 subsamples. Since the characteristics of a classifier are not only its (overall) classification rate, two additional values are calculated in the same manner for normal events with noise, namely the correctness and the purity. The characteristics of a classifier are defined as:

$$\text{overall classification rate}(E) = \frac{\text{number of correct classified events}(E)}{\text{total number of events}(E)} \tag{5.1}$$

$$\text{purity of class A}(E) = \frac{\text{number of correct classified events from class A}(E)}{\text{total number of events classified as class A}(E)} \tag{5.2}$$

$$\text{correctness of class A}(E) = \frac{\text{number of correct classified events from class A}(E)}{\text{total number of events with true class A}(E)} \tag{5.3}$$

In order to reduce the risk of a tendency towards a certain class within an energy range the amount of events for each flavour and energy range has been equalized before the classifier was tested.

5.3.1 Flavour Classification

The following section contains the results of the classification between ν_μ events and ν_e events. For both flavors CC and NC interactions were present within the event samples (the ratio of CC and NC events for normal events with noise after the event selection is shown in figure B.1). The first classification results presented are results form the classification into ν_μ and ν_e event. For each event sample the overall classification rate is plotted within the following figures, where the red dot is the median, upper and lower error bar mark 85 % and 15 % quantile.
In figure 5.28 the results for the cross validation of premium events without noise are presented. A clearly visible energy dependency is present. The classification rate increases with higher neutrino energies and seems to converge to a value in the range of 0.85. It is also noticeable, that the difference between 85 % quantile and 15 % quantile is quiet large, almost 9 % at a neutrino energy of 9 GeV.
The classification rates for premium events with noise are plotted in figure 5.29. The rates for energies below 6 GeV clearly decrease when noise is present, while the rates for higher energies are not as much affected.
Figure 5.30 shows the classification rates for normal events without noise. Compared to premium events without noise the rates for energies below 6 GeV decrease significantly. The classification rates for higher energies seem to remain almost at the same position. Also noticeable is the smaller distance between 85 % and 15 % quantile, which might be due to the larger amount of normal events compared to premium events.

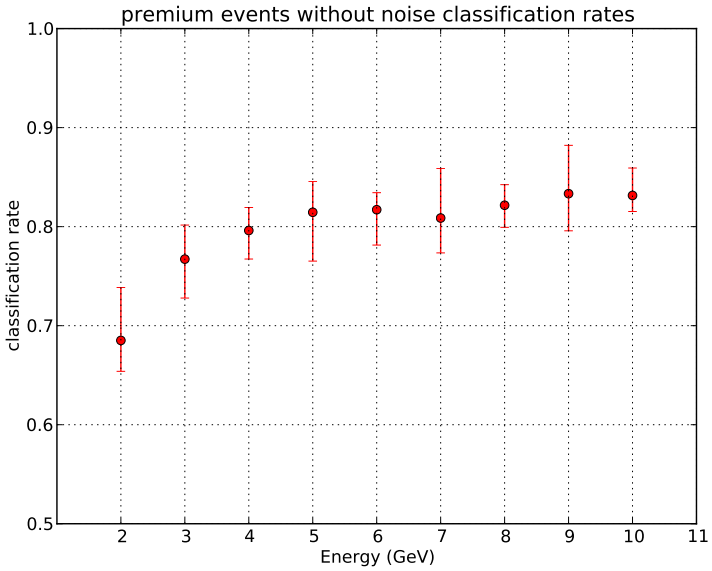

Figure 5.28: Overall classification rate for ν_e ν_μ distinction for premium events without noise

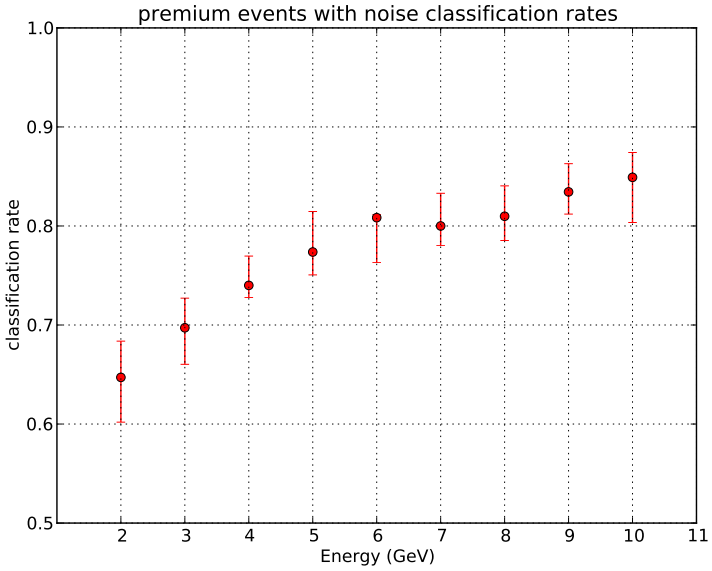

Figure 5.29: Overall classification rate for ν_e ν_μ distinction for premium events without noise

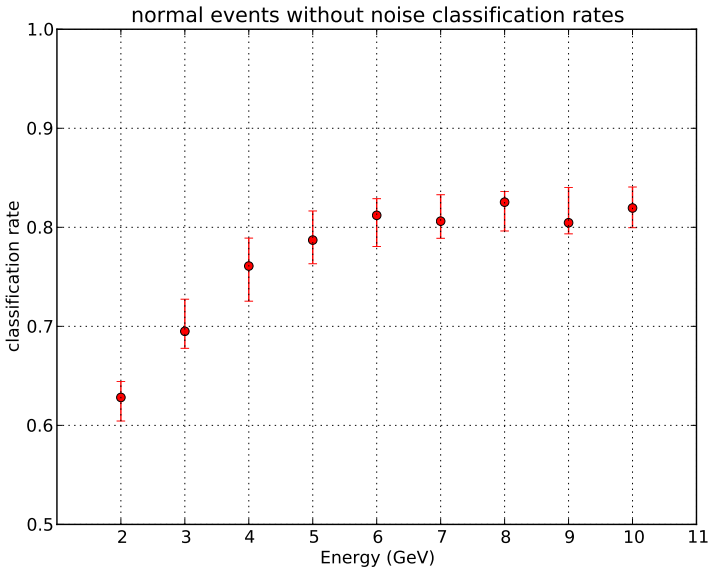

Figure 5.30: Overall classification rate for ν_e ν_μ distinction for normal events without noise

Since normal events with noise are the most realistic events probed in this thesis more properties of the classification for these events shall be presented. Figure 5.31 contains the overall classification rates for normal events with noise. For each energy range the classification rate decreases, but the effect is more distinct for low energies compared to the classification rates for normal events without noise. With increasing energy the classification rate seems to converge towards a value in the range of 0.8.

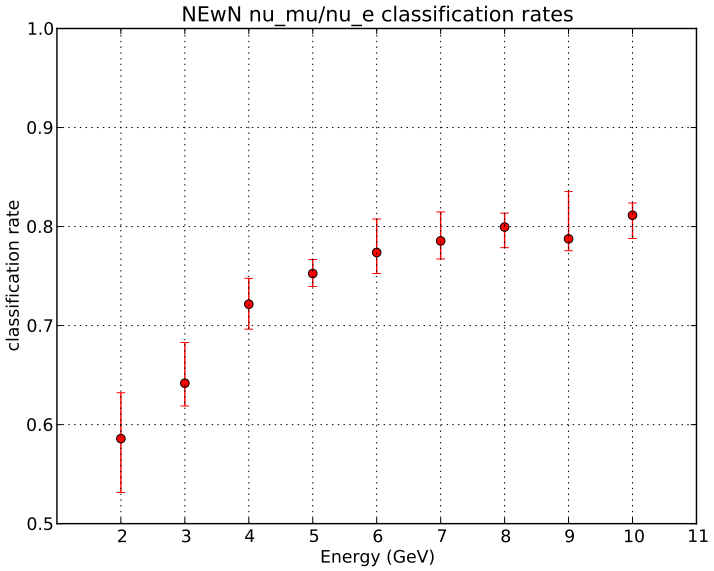

Figure 5.31: Overall classification rate for ν_e ν_μ distinction for normal events with noise

The correctness for ν_μ and ν_e normal events with noise is plotted in figure 5.32. It is clearly visible, that the probability for a correct classification of ν_e events is much higher than for ν_μ events for all energies above 2 GeV. While the energy dependency for ν_e is very distinct for the hole energy range, the correctness for ν_μ events seems not to increase further for energies above 5 GeV.
Figure 5.33 shows the purity of the flavour classification for ν_μ and ν_e normal events with noise. Still the energy dependency is present in both graphics. The purity of ν_e events is clearly lower compared to ν_μ events, which is correlated to the low correctness values for ν_μ events (since only two classes are defined within this classification).

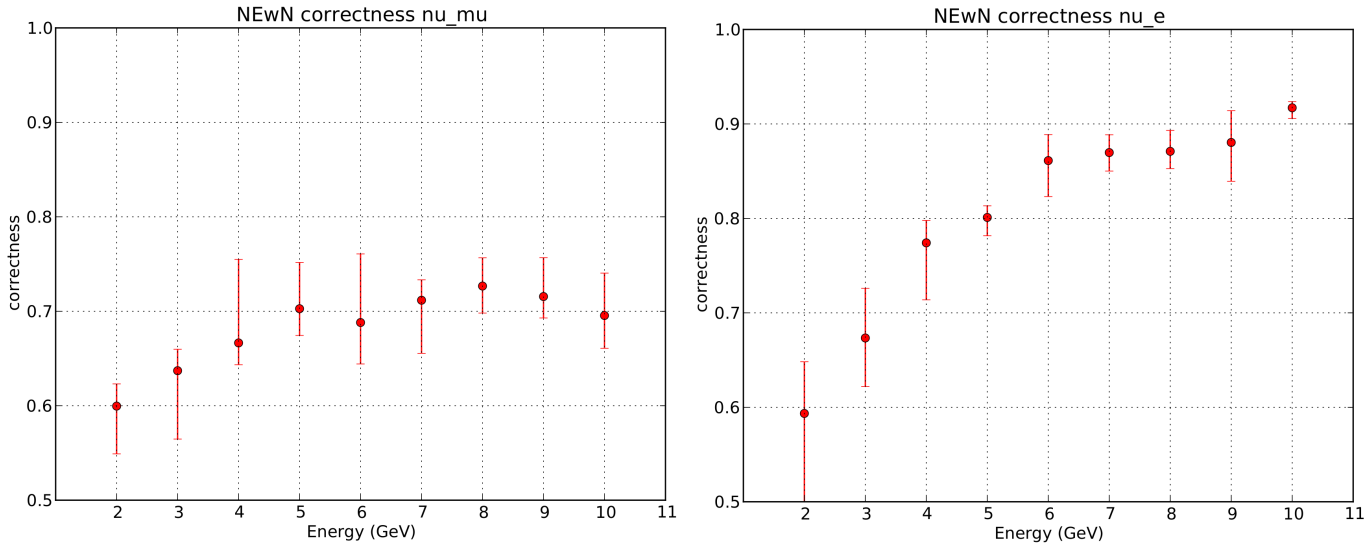

Figure 5.32: **left:** Correctness of ν_μ events of the flavour classification with normal events with noise. **right:** Correctness of ν_e events of the flavour classification with normal events with noise.

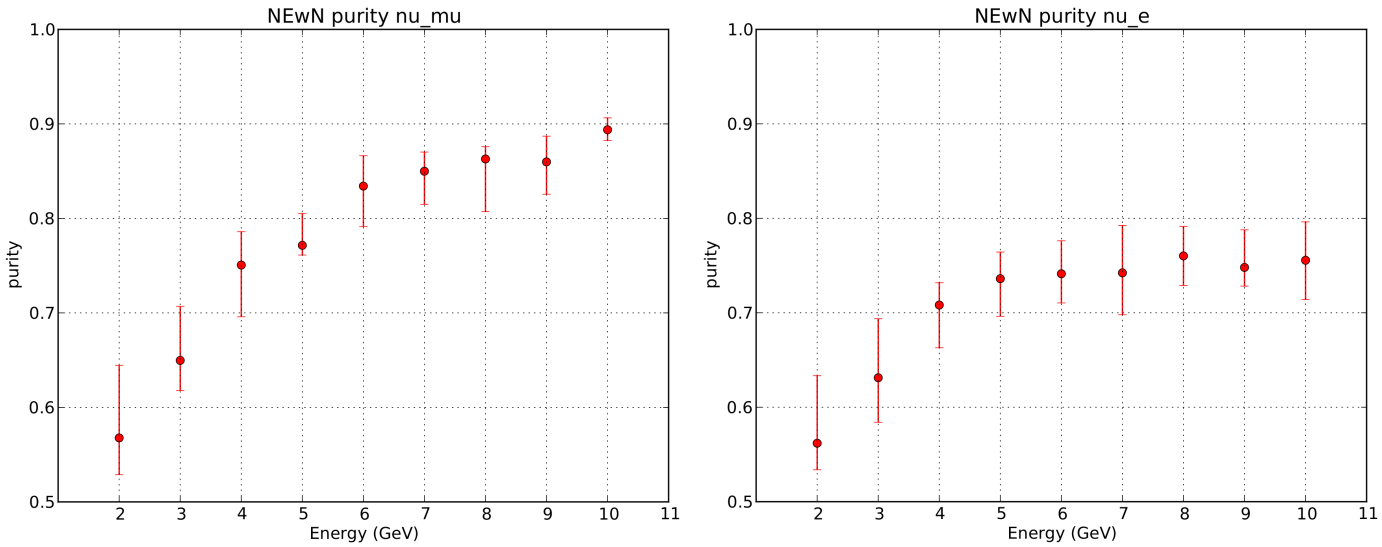

Figure 5.33: **left:** Purity of ν_μ events of the flavour classification with normal events with noise. **right:** Purity of ν_e events of the flavour classification with normal events with noise.

5.3.2 Track and shower classification

In the following section the classification results for a distinction between track like and shower like events are presented (as proposed in [22]). A track like event is defined as a ν_μ CC interaction and a shower like event is defined as ν_e CC, ν_e NC and ν_μ NC, since a NC reaction only causes a hadronic shower and no lepton. Only selected normal events with noise are used for the following results. Apart from the different defined classes the same classification and analysis methods as before are used.
In figure 5.34 the overall classification rate for the track shower classification are plotted. A increasing classification rate for higher neutrino energies is clearly visible. The median reaches values above 0.85 for neutrino energies over 7 GeV, which is a significantly higher value than for the flavour classification with the same event sample.

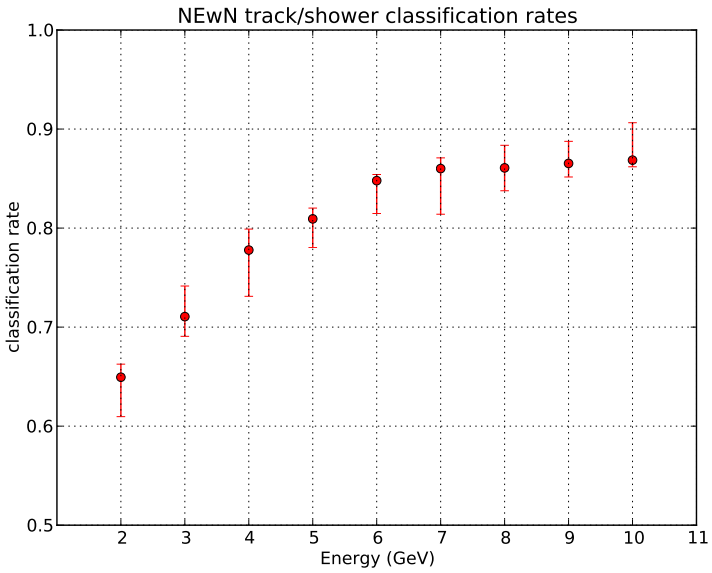

Figure 5.34: Overall classification rates for the track shower classification for normal events with noise

The correctness for track like and shower like events is illustrated in figure 5.35. A distinct energy dependency can only be seen for the correctness of track like events. Shower like events show also an energy dependency, but much less significant. It is also remarkable that the correctness of track like events for 2 GeV drops to below 0.4, while the correctness of ν_μ events for the same event reaches a value of approximately 0.6 (for the ν_μ ν_e classification).
In figure 5.36 the purity for track and shower like events is plotted. An energy dependency is present in both graphs, though the purity for shower like events increases to a value of almost 0.9, while the purity for track like events remains below 0.85 for increasing neutrino energy.

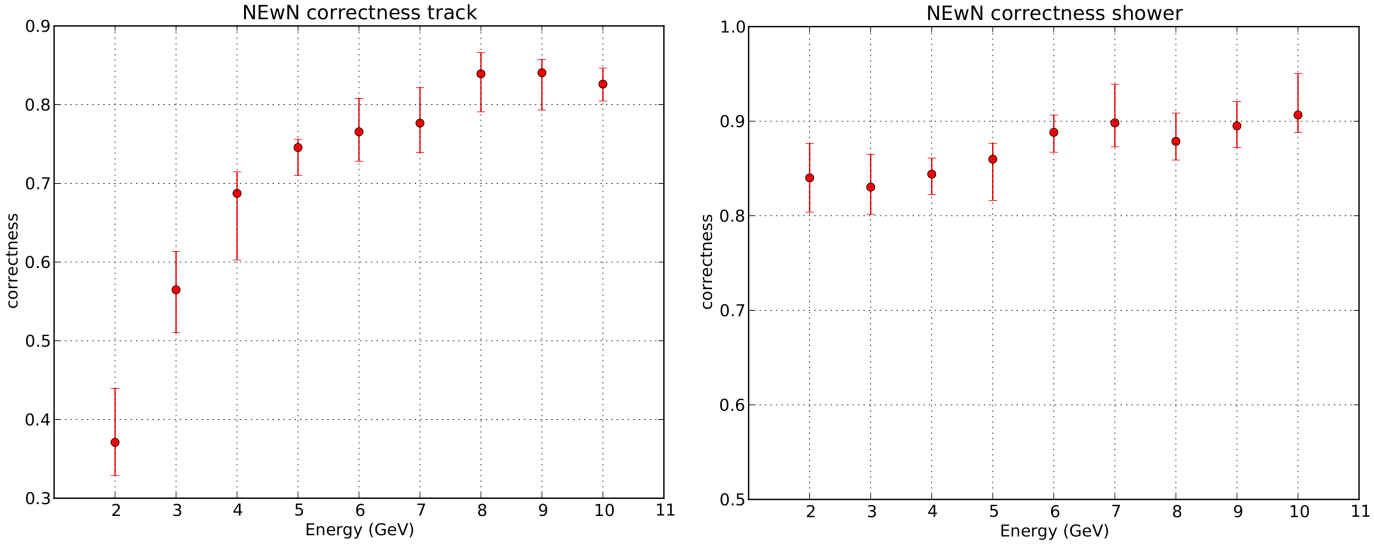

Figure 5.35: **left:** Correctness of track like events of the track shower classification with normal events with noise. **right:** Correctness of shower like events of the track shower classification.

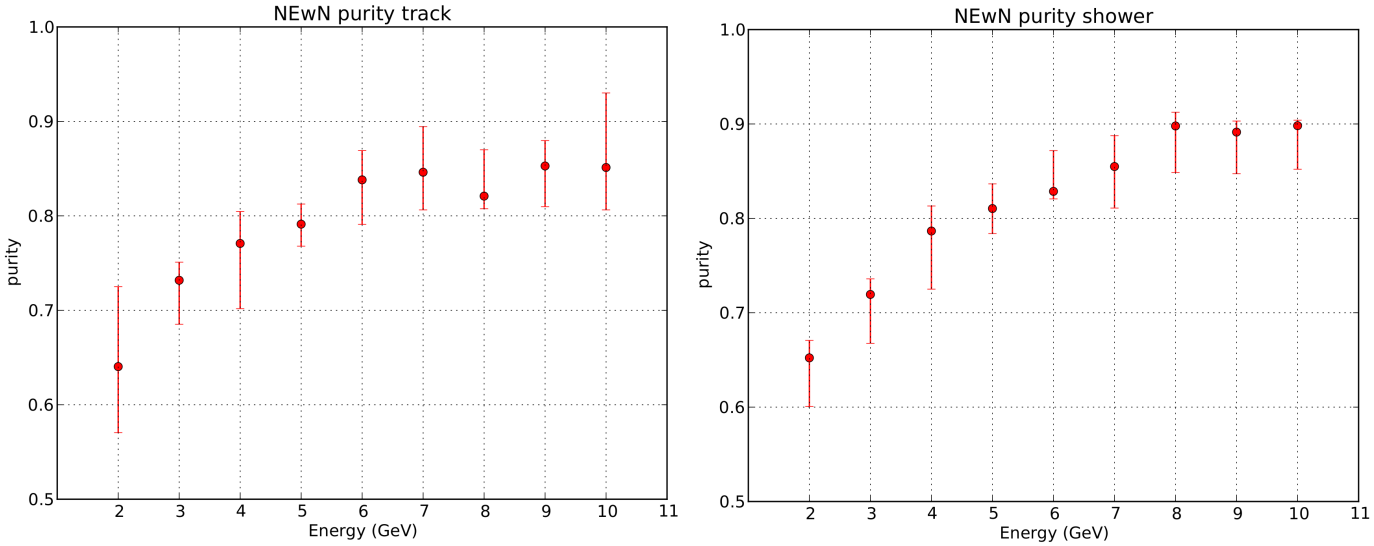

Figure 5.36: **left:** Purity of track like events of the track shower classification with normal events with noise. **right:** Purity of shower like events of the track shower classification.

Chapter 6

Conclusion

Within the following chapter the main results, which have been presented in chapter 5, are discussed and interpreted.

The first results which shall be discussed are the efficiency values for the applied event selection. The selection efficiency for all premium event samples is only about 90 %. Since the vertex for premium events is always inside the detector and the distance between reconstructed vertex and true vertex is not too big (largest 85 % quantile is below 9 m, see figure 5.7) in almost every case the track cut causes events to be sorted out. If a premium event is sorted out, then either the angular error of the reconstructed track is high, or the value of B_y of the respective event is large. In both cases the event would not be suited for the track length reconstruction developed in this thesis, because either the conic sections are not elliptical any more due to the shallow angle between detector plane and lepton or the error on the reconstructed tracks are so big, that the calculated ellipses would not match the true form of the Cerenkov rings any more.
For normal events the efficiency drops to 20 %. For these events the vertex cut becomes important, since only about 20 % of the possible volume for the vertex is inside the detector. An interaction vertex at the right end of the detector, so a large positive x-value (see footprint in figure 4.6) would also be sorted out, since not enough detector planes would be able to detect Cerenkov rings. Furthermore, semi contained event, so events with a vertex left of the detector, or very close to the edge (except for the right edge), might also be sorted out, since only a fraction of the Cerenkov light would propagate into the detector, which increases the probability of large track reconstruction errors.
The next effect is that the selection efficiency is higher for larger neutrino energies independent of event sample neutrino flavour. This effect can be explained due to the track cut within the event selection process. If the neutrino energy is low, the available lepton energy is reduced as well, thus the amount of hits, caused by the lepton, is low as well. Less hits means less information and therefore a higher error rate for the reconstruction algorithms and therefore a higher probability for large angles between reconstructed track and beam direction, which causes the event selection to sort out respective events.
The second effect is the larger difference between events with noise and without noise for low energetic premium events. This is also a consequence of the lower

amount of hits produced by low energy neutrino events. Since the noise rate is equal for each event the fraction of event hits drops significantly with the initial neutrino energy, which then causes a higher probability for reconstruction errors. For normal events this effect is also present although not as distinct as for premium events. Since the efficiency is much lower for normal events the difference between events with and without noise is almost not visible in the figure 5.1.
Furthermore the effective volume for ν_μ and ν_e normal events with noise has been presented. With increasing energies the effective volume for both flavors converges towards the actual instrumented volume, which also is present within the fitted functions. The effective volume for ν_μ events even excels the instrumented volume, which is due to the fact, that semi contained events can still cause enough hits within the detector to be recognizes as event. Though this is true for ν_e events as well, muons can propagate further through water than electrons, therefore the vertex can have a greater distance to the detector and the event would still cause enough hits to pass the event selection.

The next results which will be discussed are the presented errors of the used reconstruction algorithms for interaction vertex, lepton direction and interaction time for selected events. The vertex reconstruction yields significantly better results for ν_e events throughout all energy ranges and event samples. Even for normal events with noise the 85 % quantile stays below an error of 2 m. This is most likely due to the fact that the vertex is reconstructed by reconstructing the position of the brightest point. Since ν_e events cause a electromagnetic shower, more photons are produced near the interaction vertex. The clearly visible energy dependency is most likely caused by the same effect. If more energy is available the electromagnetic shower gets bigger, causing Cerenkov light emitted further away from the vertex, which then leads to a larger distance between reconstructed and true vertex. The vertex reconstruction error for ν_μ events is much larger. While median and 15 % quantile are clearly below $2\,m$ the 85 % quantile goes almost to values of 10 m. The energy dependence for the 85 % quantile can also be explained by the amount of light which is not produced near the true interaction vertex. A muon with more energy is capable of propagating further through water, thus emitting more light, which then causes the vertex reconstruction algorithm to yield a vertex shifted towards the lepton direction. The fact that the 85 % quantile reaches higher values for ν_μ events with noise than without noise is quiet surprising, but since this is present for premium and normal events and all energy ranges a statistical effect seems unlikely.
Since reconstructed vertex and interaction time are calculated by the same algorithm it makes sense to discuss the time reconstruction before the track errors. The analysis of the reconstructed interaction time errors almost exactly resembles the reconstructed vertex errors, since both values are reconstructed by the reconstruction of a particle shower. For ν_e events the 85 % quantile stays below 7 ns for all event samples and noise only has a small effect towards larger positive time errors. An energy dependency is still clearly visible, which also leads to larger positive errors for higher neutrino energies. The median for ν_μ events remains around 5 ns but a small increase with higher neutrino energies is present. When noise is present, the errors are shifted slightly towards larger positive values, except for the 85 % quantile, which decreases, similar to the

error of the reconstructed vertex.
The reconstruction of the lepton track was performed by another algorithm. All event samples show a clear energy dependency. The angular error decreases with increasing neutrino energy, which is not surprising, since more neutrino energy leads to a higher lepton energy and therefore to either a longer lepton track or a larger particle shower, which is boosted in lepton direction. In both cases more hits which can be connected to the lepton direction can be detected, thus enabling a better track reconstruction.
The energy dependency of the track reconstruction can also be correlated to the distribution of the kinematic angle, so the difference between the initial neutrino direction and the lepton direction (see figure 5.3). A clear energy dependency can be seen, such that with increasing energy, the kinematic angle tends to decrease, for muon and electron neutrinos. With decreasing kinematic angle the probability for a low B_y increases, which means more energy for the lepton, thus a better track reconstruction. Since a neutrino beam is used, the neutrino direction is known (angular spread is negligible, see section 4.2). Therefore the difference between reconstructed track and initial neutrino direction can be correlated on the one hand to the initial neutrino energy, and on the other hand to the value of B_y. Therefore the angular difference between beam direction and reconstructed track is one of the additional features passed to the classifier.
The effect of noise is clearly visible within the results of the track reconstruction for both flavors and all event samples, but more distinct for low energies than for high energies, which is due to the fact that high energetic particles produce more light, thus are more outstanding against background noise, which makes a reconstruction better. For two event samples, namely selected ν_μ premium events without noise (figure 5.14) and selected ν_e normal events without noise (figure 5.16) large fluctuations for the 85 % are visible. It is assumed that this is a statistical effect.

The main topic of this thesis was to develop an algorithm for the distinction of ν_e and ν_μ events. Within the following paragraph the classification rates of this method are discussed. The first results, and maybe the most important, is that a distinction between ν_e and ν_μ events with the calculated features works for all energy ranges and all probed event samples.
A clear energy dependence is also visible in all graphs. Higher neutrino energies increase the classification rate, which seems to converge toward a rate of approximately 0.83 for premium events without noise, and 0.80 for normal events with noise. The energy dependency can be explained by various reasons.
The most important parameter for a successful classification is probably the quality of the reconstructed lepton direction. This can be seen by comparison of the figures of the angular error and the classification rates. While the medians for the angular error seem to obey an exponential law with negative exponent, the classification rate might fit $R(E) = (1 - e^{-aE}) \cdot b$, with the parameters a and b. A correlation between track direction error and classification rate is not surprising, if the method for the track length reconstruction is considered. A wrong track direction leads to a wrong calculation for the possible Cerenkov ring, thus the probability for detecting Cerenkov light from the lepton decreases.
The second reason for the energy dependency is the available energy for the lepton. If the neutrino energy is high, the energy for the produced lepton is higher as well. The more energy a muon has, the longer it can propagate through

water, thus increasing the differences between ν_e and ν_μ events. Another reason for the energy dependency is the amount of hits, and therefore the amount of information, which is available. More information in general means a better understanding of what happened within the detector.
Keeping in mind, that both, vertex and interaction time reconstruction, tend towards larger errors with increasing energy, and that both values are used in order to calculate the event features, it seems that the classification method is not too much affected by reconstruction errors of these values. For none of the classified event samples a broadening of the distance between 15 % and 85 % quantile or decrease for the median with increasing neutrino energy is clearly visible.
Never the less, the distance between the two quantiles is not negligible. The reason for this behavior might be due to statistical fluctuations, and the classification rate might become more stable if more events would be available, but this is only an assumption, which can not be verified at this point.
Apart from the distinction between neutrino flavour the developed classifier was used to classify track like and shower like events. For all energy ranges this yields a better overall classification rate then a flavour classification with the same event sample. The classification rate for a track shower distinction converges for increasing energy to a value above 0.85. The reason for this is most likely the separation between ν_μ CC and ν_μ NC events. In a ν_μ NC reaction no muon is produced, therefore no track can be reconstructed, which is the main information source for the classifier. This probably causes a high probability for a misclassification for ν_μ NC events with a flavour classifier. Since a NC reaction still causes a hadronic shower, a classification between track and shower like events does not have this problem.

The last part of this chapter is now to connect the classification results to the in [22] presented estimations concerning the distinction between the two neutrino mass hierarchies.
In figure 6.1 the correctness rates for track like and shower like events from the track shower classification are illustrated and fits have been added. The function $\text{correctness}(E) = (1 - e^{a(E-c)}) \cdot b$ has been used for the fit. The parameters for the plotted functions are: $(a, b, c)_{track} = (0.528, 0.838, 0.881)$ and $(a, b, c)_{shower} = (0.0848, 0.984, -19.8)$. Additionally the assumed correctness for the distinction of ν_μ CC and ν_e CC events from [22] is plotted, which was assumed to be equal for both interaction types. The absolute value of the relative difference between obtained correctness fits and assumed correctness are shown as well (black line for track like events and cyan line for shower like events). It can be seen, that the difference for track like events reaches a value of 30 % at 2 GeV but drops to below 10 % at 4 GeV. Thus, the assumed correctness for track events has been overestimated compared to the here obtained results of approximately 10 %. Before the correctness of shower like events is compared to the estimated rate, it has to be emphasized that the shower like events in [22] are defined as ν_e CC events only, while in this thesis shower like events are defined as ν_e CC, ν_e NC and ν_μ NC (the ratio for CC and NC events within the used event sample is plotted in figure B.1). The correctness of shower events, however, has been underestimated, especially in the energy range below 4 GeV. For higher energies the difference seems to converge almost to zero. The mean difference to the estimated correctness is also less than 10 % for shower like

events.
Summing up, the obtained classification results do look promising concerning the proposed experimental setup for the measurement of the neutrino mass hierarchy. The mean differences between the correctness rates are less than 10 % of the estimated values but have different sings. Since the counting of shower like events is proposed in order to distinct between the two mass hierarchies, the high correctness values for shower like events increases the probability for a successful exclusion of one hierarchy even more.

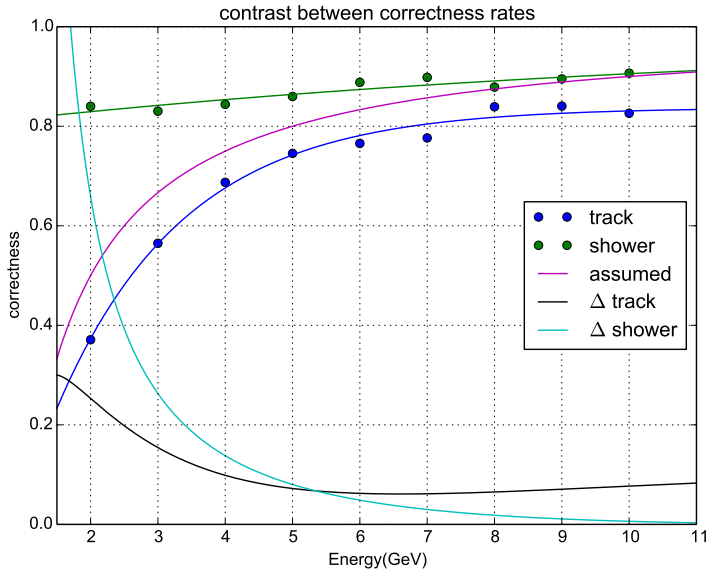

Figure 6.1: Illustration of the correctness values for track like events (blue), shower like events (green), the assumed correctness from [22] (mangan), the relative difference between track like correctness fit and assumed curve (black) and the relative difference between shower like correctness fit and assumed curve (cyan).

Chapter 7

Summary and outlook

Within this thesis the individual steps, from first idea to efficiency analysis, of a working algorithm for the distinction of ν_e and ν_μ beam events with a megaton Cerenkov detector have been described. The distinction algorithm calculates for each event features with a track length reconstruction. With the so calculated features and four additional features a random decision forest is used in order to classify simulated beam neutrino events in two classes, ν_e and ν_μ events.
Furthermore the production chain of four different neutrino beam event samples, namely premium events, which are events with a vertex within a small volume inside the detector, and normal events, which have a vertex within or outside the detector, each sample with and without noise, has been explained in detail. To achieve results as detailed as possible, nine different energy ranges, 2, 3, 4, 5, 6, 7, 8, 9 and 10 GeV, which represent the energy range for the proposed beam, with a band width of $\pm 2.5\,\%$ were simulated for each event sample. Since the developed track length reconstruction makes use of a reconstructed vertex, lepton direction and interaction time, a detailed analysis of these reconstruction algorithm was performed in order to get a detailed understanding of the distinction results.
Furthermore the efficiency of a simple event selection, which was used to find out whether an event is suited for the track length reconstruction or not, was analyzed.
Finally, the developed classifier was used for the distinction of track like events, so ν_μ CC, and shower like events, so ν_e CC, ν_e NC and ν_μ NC. The so obtained results of the classifier were then compared to the estimated classification rates for the proposed experimental set up in [22].

In order to continue the P2O plausibility study several aspects need to be investigated. One of them is to investigate the influence of ν_τ events. It would be very interesting to know how the classifier would treat such events, and if it would be possible even to recognize them. Although no ν_τ are present when the neutrino beam is produced, due to neutrino oscillation this flavour is present within the neutrino beam at the detector site (see figure 3.1, high oscillation probability for $\nu_\mu \rightarrow \nu_\tau$ for a distance of 2600 km). The separation of NC events from shower like events and the classification in three classes, so ν_μ CC, ν_e CC and NC events, with the developed classifier would also be interesting to investigate. Another necessary step would be to change the detector layout to

a realizable layout, so a realistic amount of PMTs and a realistic distance between the strings and to test the reconstruction algorithms and the classification method with this new layout.
Some improvements for the track length reconstruction algorithm might improve the classification rate further. One of these possible improvements concerns the method which determines, whether a hit lies on a Cerenkov ring or not. At the moment this is done by checking whether they share the same pixel. Since the position of a PMT is approximated as the position of the center of the optical module some hits might not be recognized as Cerenkov hits. A more stable method might be to calculate whether the Cerenkov ring, an ellipse, and the optical module, a circle within a detector plane, have intersection points, which is analytical possible (real roots of a fourth degree polynomial). Furthermore the mean angular error of the track reconstruction might be included in a way that not only one Cerenkov ring is calculated, but more Cerenkov rings, corresponding to various track direction within the mean track error. Another improvement which might be useful concerns the time and distance binning of the track length reconstruction. Since the reconstructed interaction time tends to be too late (positive errors), it seems useful not only to make a difference between negative and positive time residual, but to implement more time bins, so even when the reconstructed interaction time is too late, Cerenkov hits within a certain time bin can be recognized.
The criteria used for hit and event selection are not due to any analysis or the results of an optimization process, but out of common sense. It would be surprising, if the used cuts can not be improved and other useful criteria could be added, which might not only improve the selection efficiency, but also the classification results.

List of Figures

List of Tables

Appendix A

Analysis of the reconstruction errors before the event selection

Within the following figures the analysis of the reconstruction errors for vertex, lepton direction and interaction time are presented for premium and normal ν_e and ν_μ events, each with and without noise. In each figure the red dot marks the median, the top error bar stands for the 85 % quantile and the bottom error bar marks the 15 % quantile.

A.1 Analysis of reconstructed interaction vertices

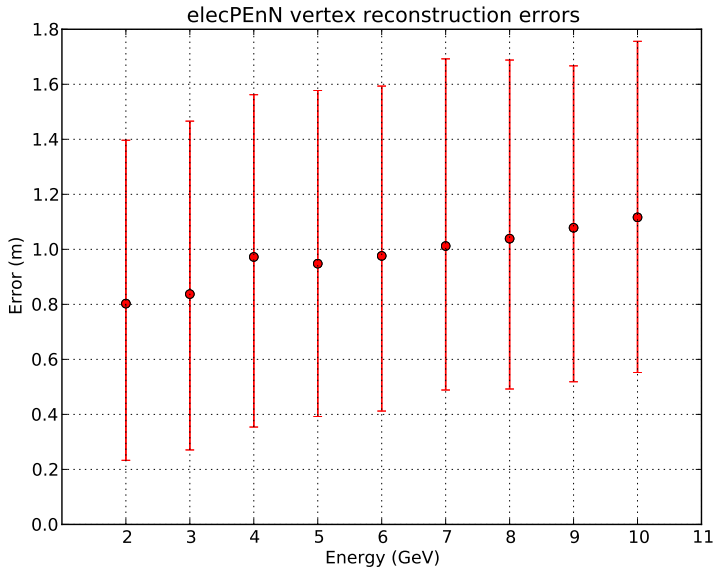

Figure A.1: Errors of the reconstructed vertex for ν_e premium events without noise.

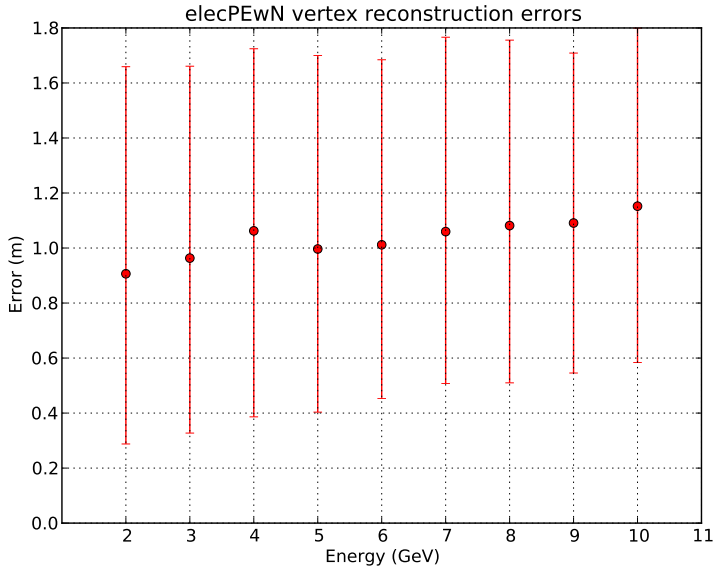

Figure A.2: Errors of the reconstructed vertex for ν_e premium events with noise.

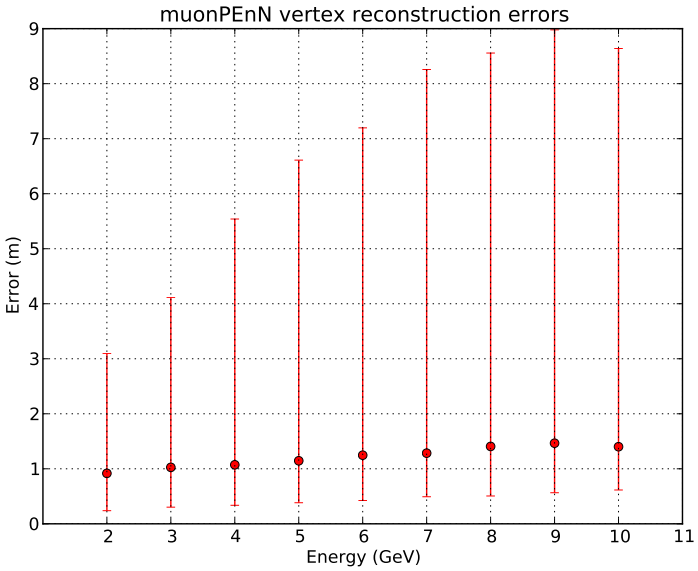

Figure A.3: Errors of the reconstructed vertex for ν_μ premium events without noise.

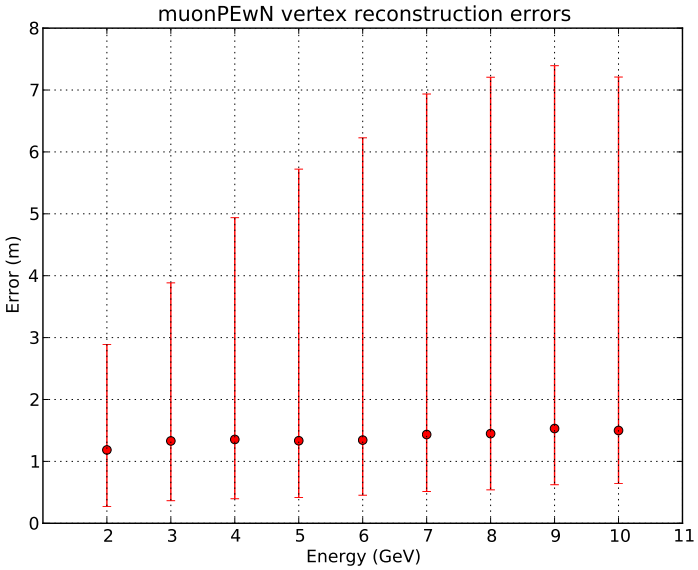

Figure A.4: Errors of the reconstructed vertex for ν_μ premium events with noise.

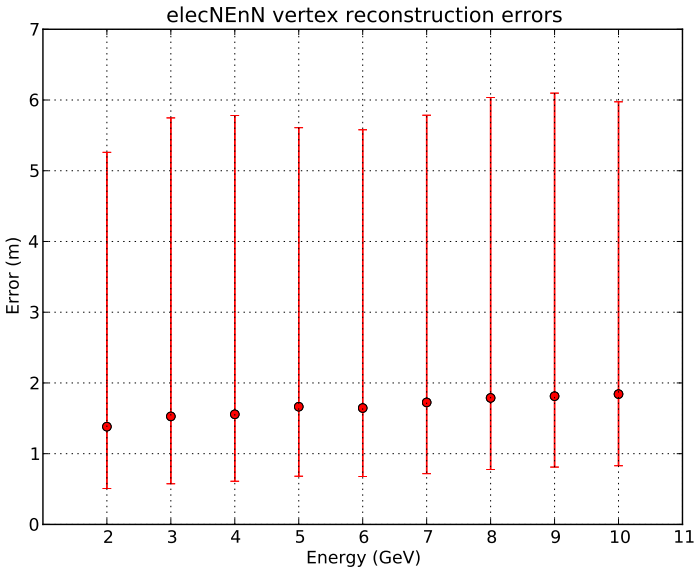

Figure A.5: Errors of the reconstructed vertex for ν_e normal events without noise.

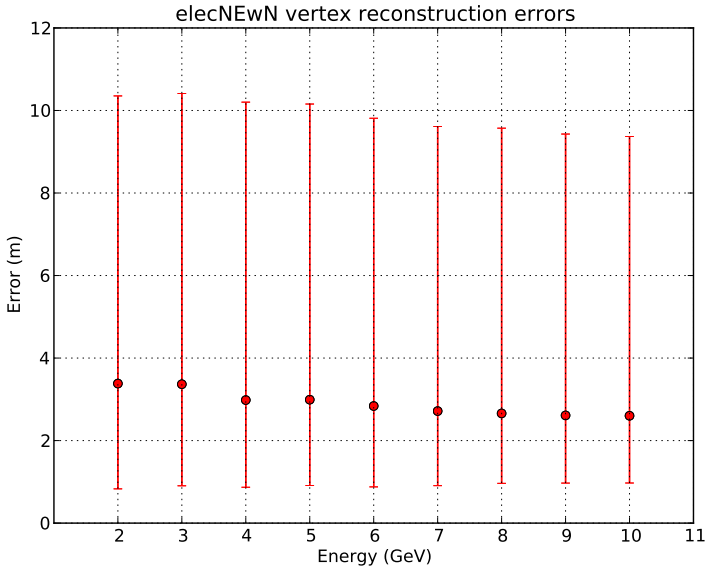

Figure A.6: Errors of the reconstructed vertex for ν_e normal events with noise.

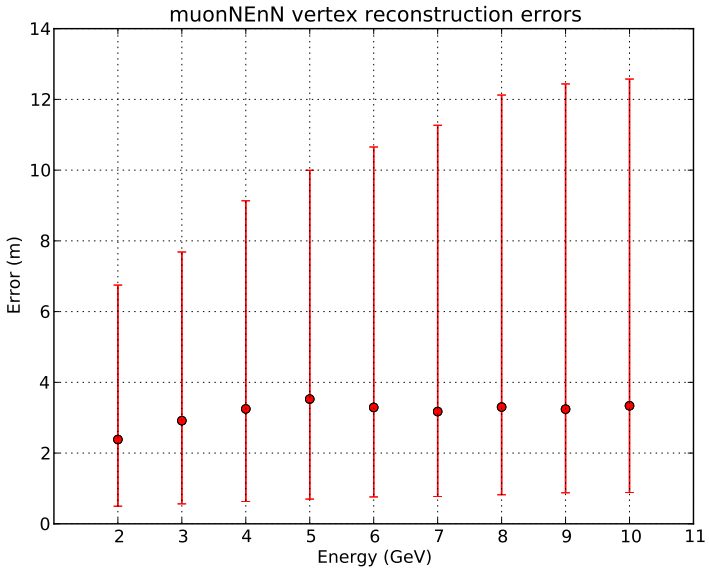

Figure A.7: Errors of the reconstructed vertex for ν_μ normal events without noise.

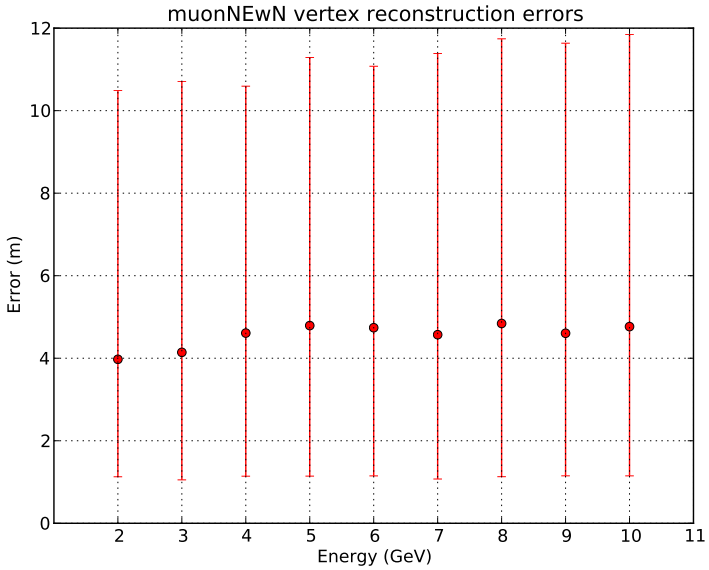

Figure A.8: Errors of the reconstructed vertex for ν_μ normal events with noise.

A.2 Analysis of the reconstructed lepton directions

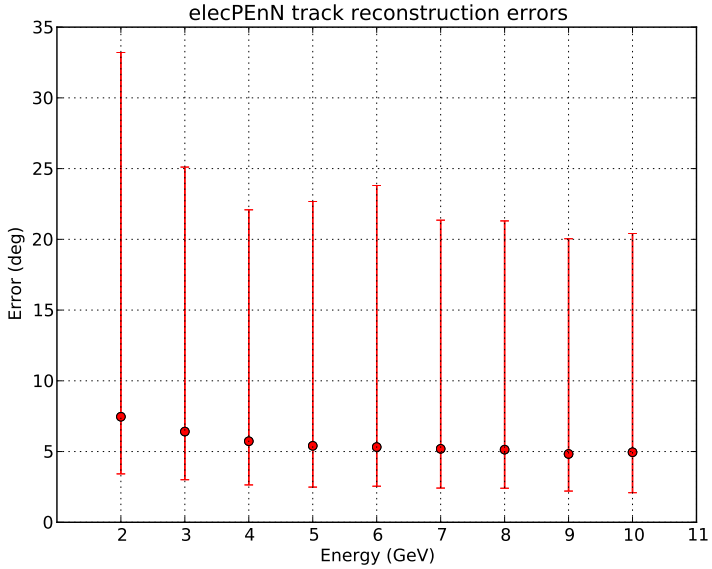

Figure A.9: Errors of the reconstructed lepton direction for ν_e premium events without noise.

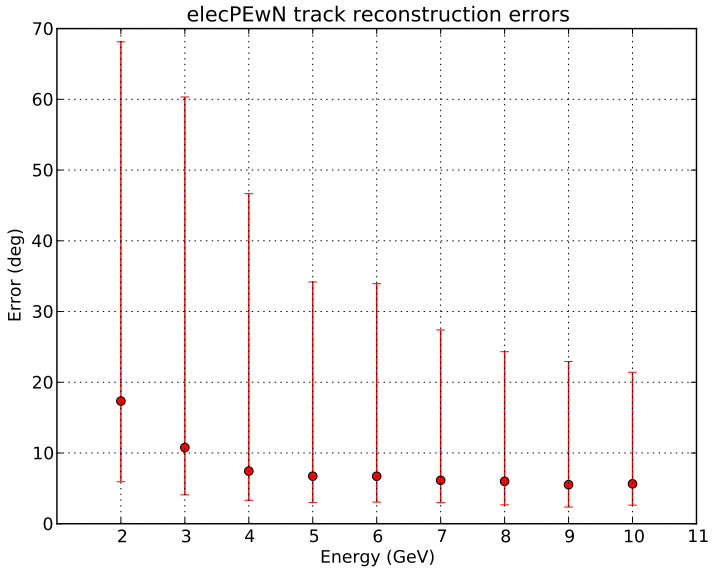

Figure A.10: Errors of the reconstructed lepton direction for ν_e premium events with noise.

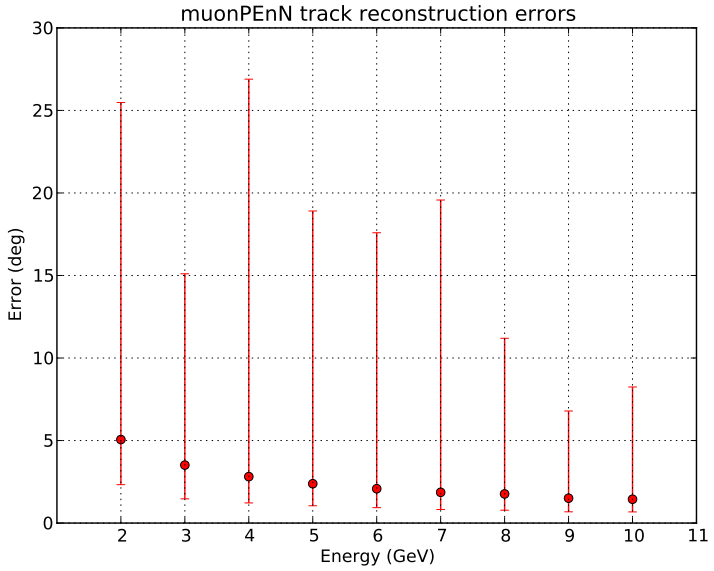

Figure A.11: Errors of the reconstructed lepton direction for ν_μ premium events without noise.

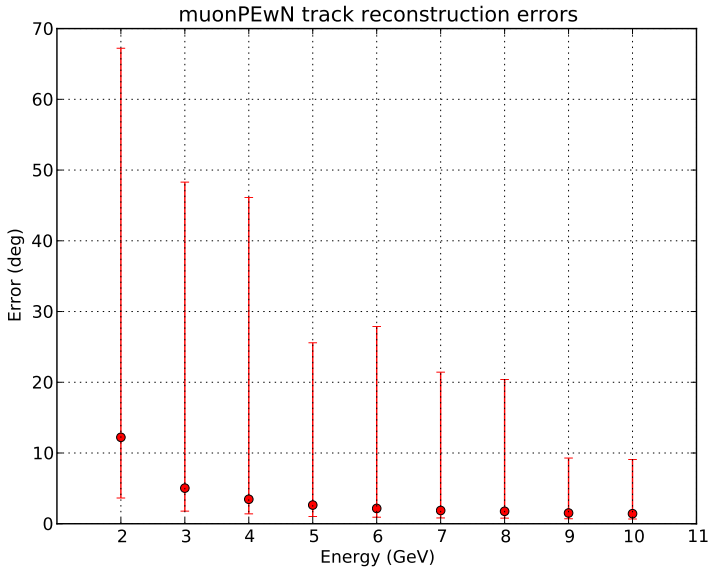

Figure A.12: Errors of the reconstructed lepton direction for ν_μ premium events with noise.

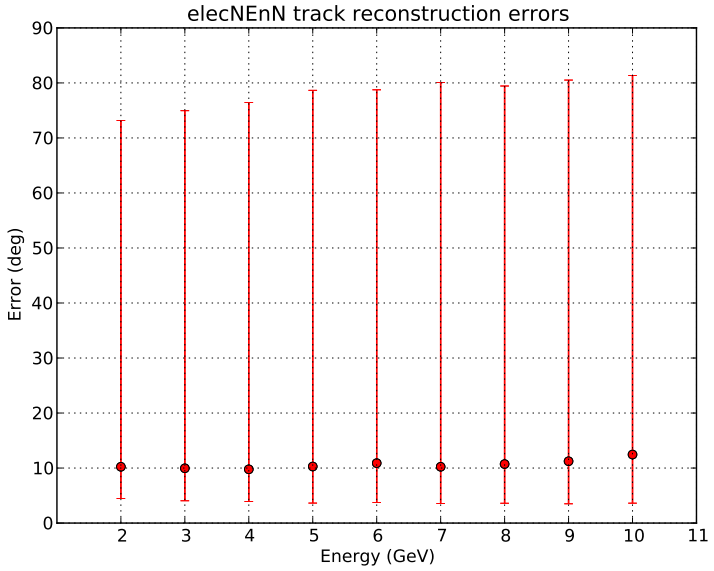

Figure A.13: Errors of the reconstructed lepton direction for ν_e normal events without noise.

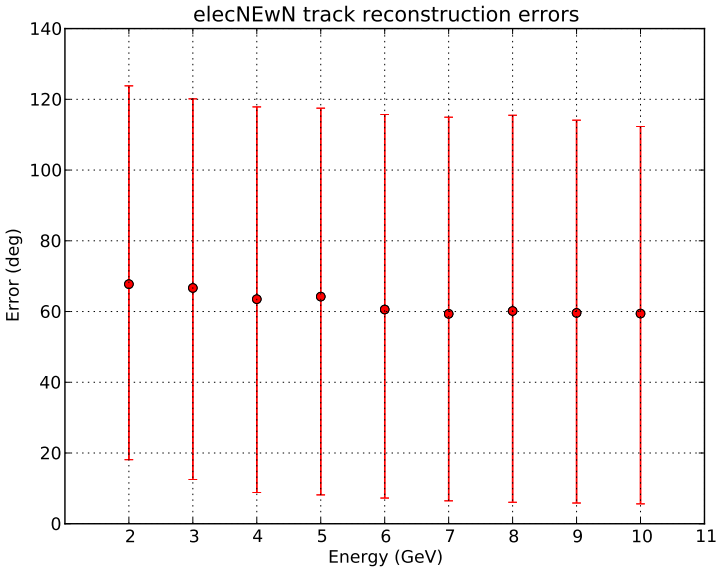

Figure A.14: Errors of the reconstructed lepton direction for ν_e normal events with noise.

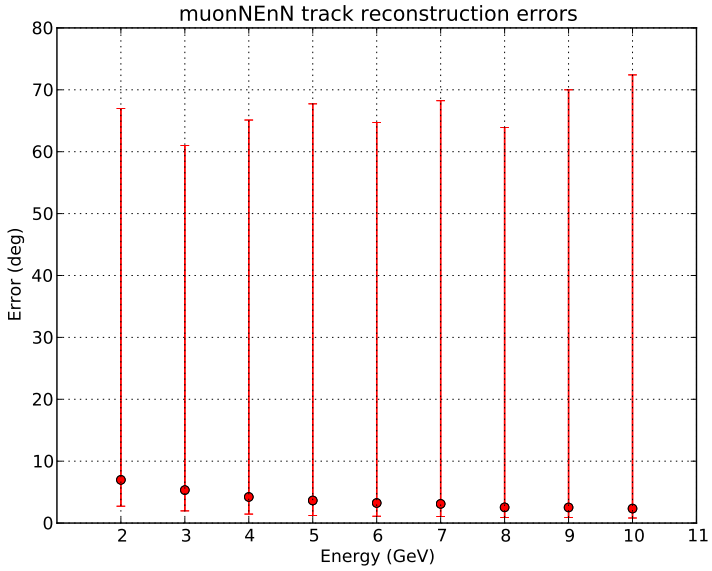

Figure A.15: Errors of the reconstructed lepton direction for ν_μ normal events without noise.

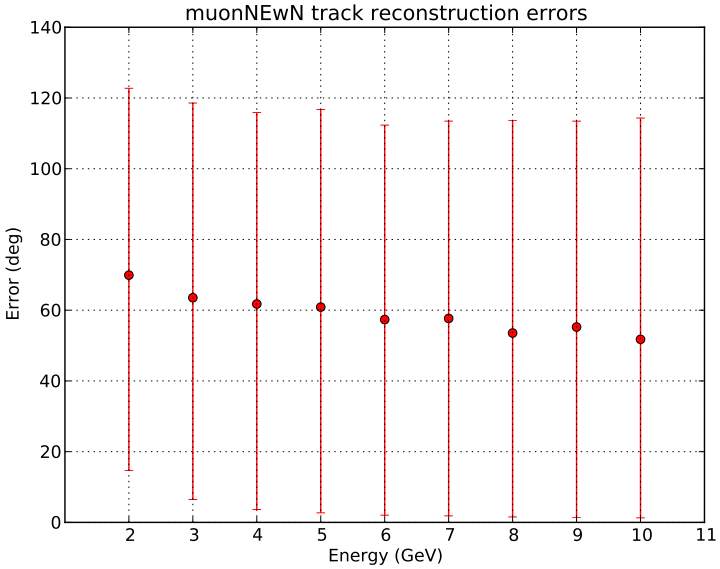

Figure A.16: Errors of the reconstructed lepton direction for ν_μ normal events with noise.

A.3 Analysis of the reconstructed interaction time

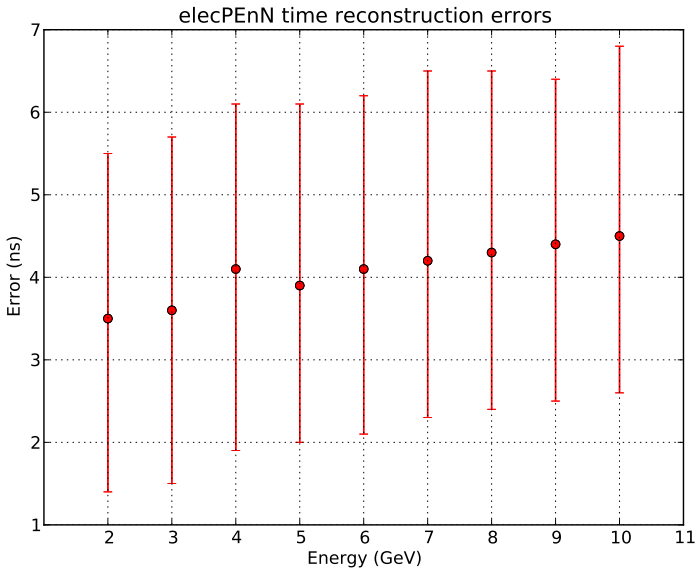

Figure A.17: Errors of the reconstructed interaction time for ν_e premium events without noise.

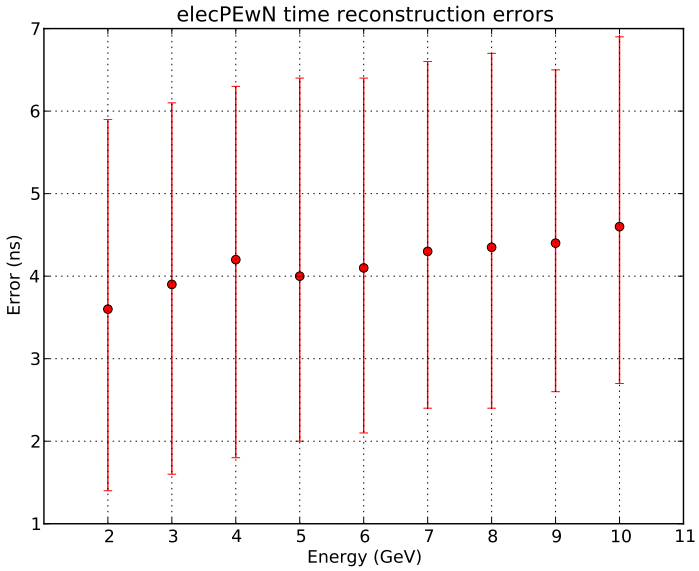

Figure A.18: Errors of the reconstructed interaction time for ν_e premium events with noise.

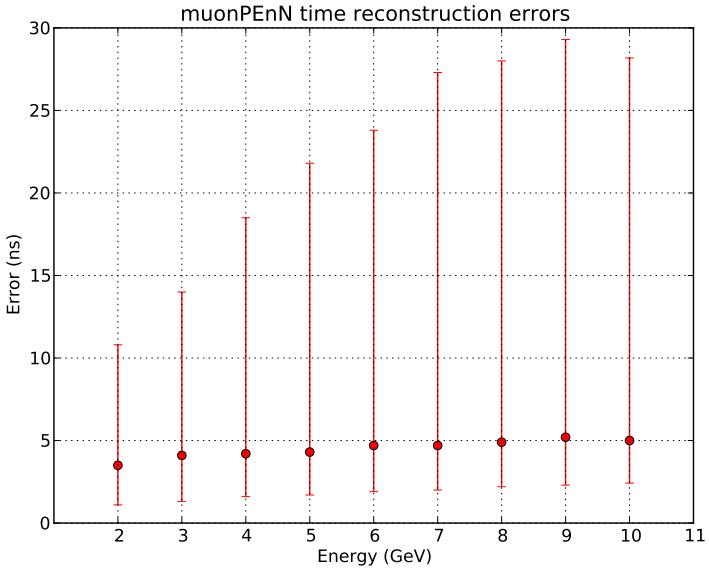

Figure A.19: Errors of the reconstructed interaction time for ν_μ premium events without noise.

Figure A.20: Errors of the reconstructed interaction time for ν_μ premium events with noise.

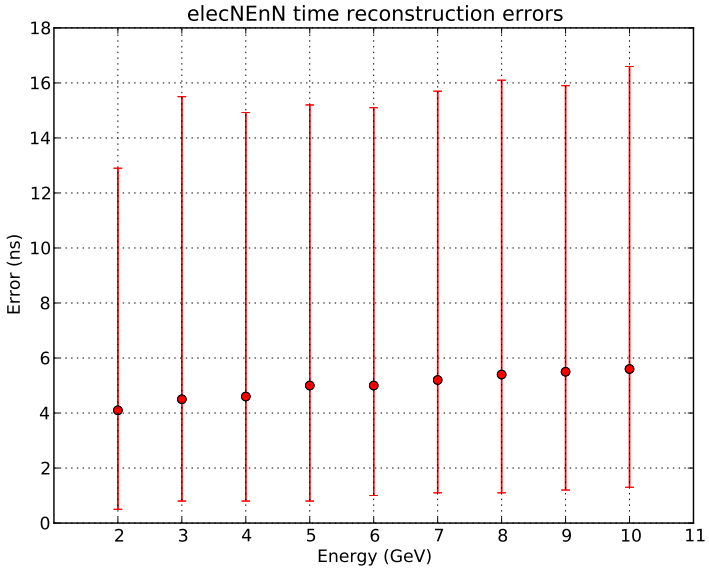

Figure A.21: Errors of the reconstructed interaction time for ν_e normal events without noise.

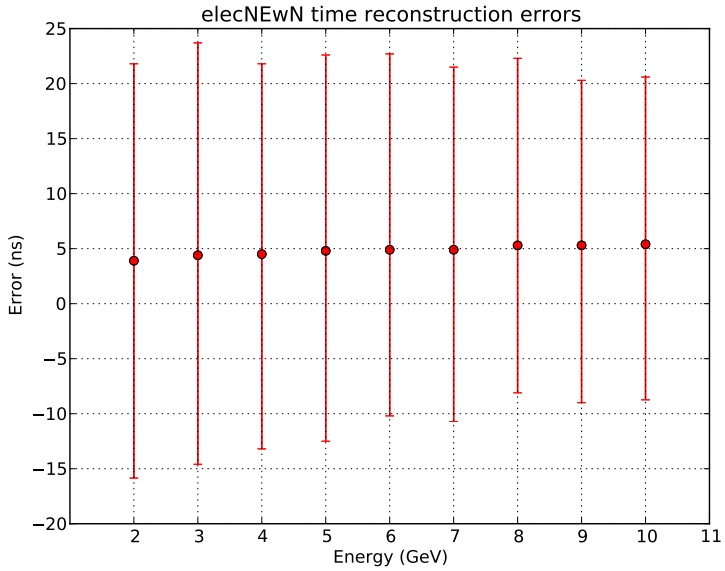

Figure A.22: Errors of the reconstructed interaction time for ν_e normal events with noise.

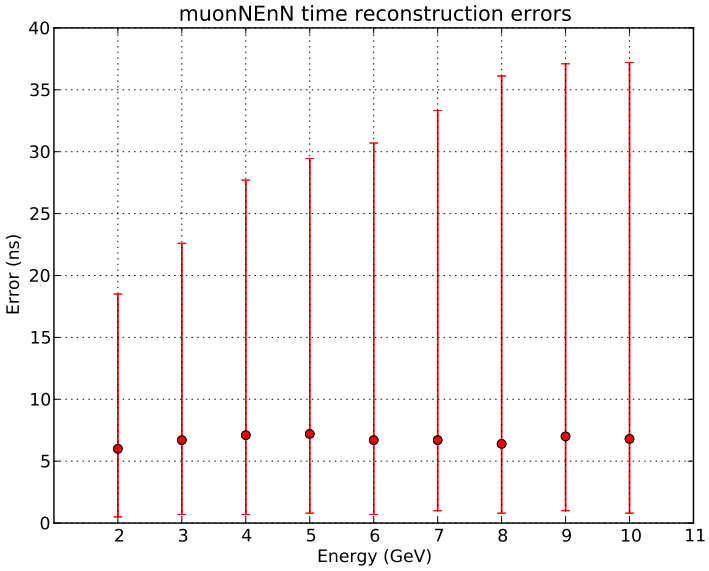

Figure A.23: Errors of the reconstructed interaction time for ν_μ normal events without noise.

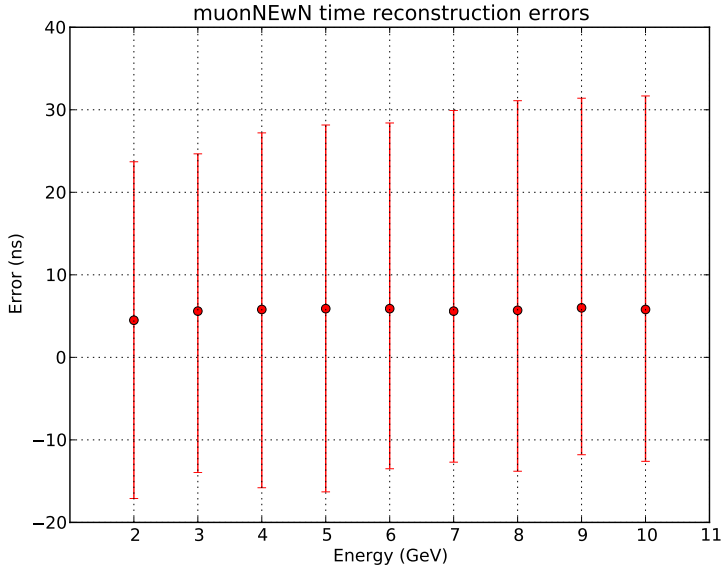

Figure A.24: Errors of the reconstructed interaction time for ν_μ normal events with noise.

Appendix B

Ratio of CC and NC interactions after the event selection

In figure B.1 the ratio for CC interactions and NC interactions within the normal events with noise event sample after the event selection is illustrated.

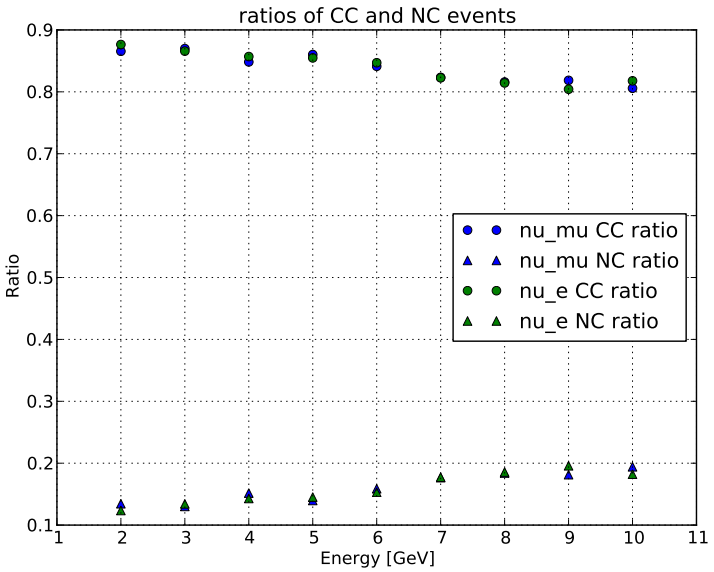

Figure B.1: Ratios for CC and NC interactions within the normal events with noise event sample after the event selection

Danksagung

Abschließend möchte ich mich bei allen Bedanken, die beim Entstehen dieser Arbeit geholfen haben.
Ein großes Dankeschön geht an Prof. Ulrich Katz, welcher immer ein offenes Ohr für Fragen aller Art hat und keine Mühen scheut Hilfe zu leisten.
Dann geht ein riesiges Dankeschön an meine Betreuer Dr. Thomas Eberl, Dr. Jürgen Brunner und Jannik Hofestädt, welche zu jeglicher Tag- und Nachtzeit bereit waren alle möglichen Fragen zu beantworten.
Abschließend geht ein Dankeschön an alle Mitarbeiter des Erlangen Centre for Astroparticle Physics, da sich immer eine hilfsbereite Kollegin, oder ein hilfsbereiter Kollege finden lässt.

Bibliography

[1] Wikipedia, standard model, November 2014. `http://en.wikipedia.org/wiki/Standard_Model`.

[2] Wikipedia, January 2015. http://commons.wikimedia.org/wiki/File:Cherenkov.svg.

[3] C. Andreopoulos et al. The GENIE Neutrino Monte Carlo Generator. *Nucl. Instrum. Meth.*, A614:87–104, 2010.

[4] Marco Drewes. The Phenomenology of Right Handed Neutrinos. arXiv:1303.6912v3, September 2013.

[5] Ariel Goobar et al. The neutrino mass bound from WMAP-3, the baryon acoustic peak, the SNLS supernovae and the Lyman-Alpha forest. arXiv:0602155v2, May 2006.

[6] G.L. Fogli et al. Global analysis of neutrino masses, mixings and phases: entering the era of leptonic CP violation searches. arXiv:1205.5254v3, June 2012.

[7] J. Beringer et al. *Particle Physics Booklet*. APS physics, 2012.

[8] K. Abe et al. Indication of Electron Neutrino Appearance from an Accelerator-produced Off-axis Muon Neutrino Beam. arXiv:1106.2822v2, July 2011.

[9] M. Ageron et al. ANTARES: the first undersea neutrino telescope. arXiv:1104.1607v2, June 2011.

[10] M. Auger et al. Search for Neutrinoless Double-Beta Decay in 136Xe with EXO-200. arXiv:1205.5608v2, July 2012.

[11] N. Agafonova et al. Observation of tau neutrino appearance in the CNGS beam with the OPERA experiment. arXiv:1407.3513v2, August 2014.

[12] P. Huber et al. Simulation of long-baseline neutrino oscillation experiments with GLoBES (General Long Baseline Experiment Simulator). arXiv:hep-ph/0407333, June 2004.

[13] S. Klimushin et al. Precise parametrizations of muon energy losses in water. arXiv:0106010v1, June 2001.

[14] Stephen F. King et al. Neutrino Mass and Mixing with Discrete Symmetry. arXiv:1301.1340v2, May 2013.

[15] Martin Freund. Analytic Approximations for Three Neutrino Oscillation Parameters and Probabilities in Matter. arXiv:0103300v1, March 2001.

[16] Stefan Geißelsöder. Classification of events for the ANTARES neutrino detector. Master's thesis, Friedrich-Alexander-Universität Erlangen-Nürnberg, July 2011.

[17] W. Heitler. *The quantum theory of radiation*. Oxford University Press, 1954.

[18] Juan José Hernández-Rey. Recent results of the ANTARES Neutrino Telescope. arXiv:1410.7720v2, October 2014.

[19] Tin Kam Ho. Random Decision Forests. IEEE Transactions on Pattern Analysis and Machine Intelligence, 20:832-844, 1998.

[20] Anthony J.G. Hey Ian J.R. Aitchison. *Gauge Theories in Paricle Physics*, volume 1. CRC Press, 2013.

[21] Jürgen Brunner. Counting Electrons to Measure the Neutrino Mass Hierarchy, April 2013. presentation at the APC.

[22] Jürgen Brunner. Counting Electrons to Probe the Neutrino Mass Hierarchy. arXiv:1304.6230v1, April 2013.

[23] KM3NeT/ORCA Collaboration. Status report on the feasibility of measuring the neutrino mass hierarchy with an underwater Cherenkov detector: ORCA, 2014.

[24] KM3NeT/ORCA Collaboration. Status Report on the feasibility of measuring the neutrino mass hierarchy with an underwater Cherenkov detector: ORCA (Oscillation Research with Cosmics in the Abyss), 2015.

[25] Y. Kudenko. Protvino Neutrino Beam. http://laguna.ethz.ch/indico/conferenceDisplay.py?confId=8, February 2013. Presentation at Laguna-LBNO General Meeting, Hamburg.

[26] R.P. Lichtfield. (Direct) Measurement of Theta13. arXiv:1209.3884v2, September 2012.

[27] Veronika Ludwig. Elektronneutrino-Untergrund bei der Bestimmung der Neutrinomassenhierarchie mit ORCA. B.Sc. Thesis, Erlangen Centre for Astroparticle Physics, 2013.

[28] Annarita Margiotta. The KM3Net deep-sea neutrino telescope. arXiv:1408.1392v1, August 2014.

[29] R. G. Hamish Robertson. KATRIN: an experiment to determine the neutrino mass from the beta decay of tritium. arXiv:1307.5486v1, July 2013.

[30] N. Schmitz. *Neutrinophysik*. B.G. Teubner, 1997.

[31] Ulrich F. Katz. The ORCA Option for KM3Net. arXiv:1402.1022v1, February 2014.